Properties and applications of structured optical fiber tapers

Ding, Wei

Award date:
2006

Awarding institution:
University of Bath

PROPERTIES AND APPLICATIONS OF STRUCTURED OPTICAL FIBER TAPERS

Wei Ding

A thesis submitted for the degree of Doctor of Philosophy

University of Bath

Department of Physics

December 2006

COPYRIGHT

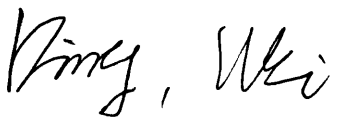

ProQuest LLC
789 East Eisenhower Parkway
P.O. Box 1346
Ann Arbor, MI 48106-1346

Abstract

This thesis focuses on the exploration of device concepts based on tapered optical fibers. The work is divided into two parts. The first part includes studies of devices made by the application of planar processing techniques to the curved surface of micron-scale fiber tapers. The second part theoretically investigates the internal excitation and superfocusing of surface plasmon polaritons (SPPs) on a silver-coated fiber tip.

In the first part, we describe the fabrication and characterisations of Au Bragg gratings, reactive-ion-etched groove gratings, HF-etched long period gratings, and focused-ion-beam milled micro-cavity structures on micron-scale fiber tapers. These devices have applications in, for example, refractometric sensing, optical filtering, wideband filters, and band-pass filters. Our work paves the way to expand the functionality of optical fiber tapers.

In the second part, we describe theoretical investigations of surface plasmon polariton (SPP) internal excitation and superfocusing on an apertureless silver-coated fiber tip. This process is relevant to the development of improved scanning near-field optical microscopes. Based on an analytical model and numerical simulations, the mode conversion and the energy transfer from fiber waveguide modes to the SPP at the silver apex are studied. Mode projection, mode coupling, metal dissipation, and radiation coupling in this process are qualitatively investigated. Our study provides a comprehensive understanding of SPP excitation and indicates how an efficient power transfer to a region far below the diffraction limit can be achieved.

Acknowledgements

There are a lot of people I should thank for their help and support during my PhD term. First of all, I would like to thank my parents for their continuous encouragements and confidences. With their loves, I am really lucky!

I specially would like to thank my supervisors Stefan Maier and Steven Andrews for their patience and insistence during the arduous research works. Stefan Maier is an active supervisor and has stimulated many important projects of my doctoral research. Steven Andrews is a truly wonderful man and has given me a lot of crucial and important suggestions. His unique view to physics and gentle temperament really benefit me. I think, even many years later, I will still cherish these three years when I work under their supervision. Thank you very much Stefan and Steven!

I must also thank Philip Russell for giving me the opportunity to work in such a great research group and opening my project.

I would sincerely thank Jonathan Knight and Tim Birks for their encouragements and helps. Although I am not their student, their kindly concernments to my work always move me. Thank you very much!

Thanks must go to the guys working in Nanofabrication Cleanroom: Spartaco Landi, Antonio Moreno-Losana, Andriy Moskalenko, Atif Aziz, Tom Kehoe, Philip Shields, Somyod Denchitcharoen, Jean-Marc Rollin ... The time spent with them is full of fun.

Many thanks to all members of Centre for Photonics and Photonic Materials. Aimin Wang, Feng Luan, Sergio Leon-Saval, Alan George, Ke Lai, Chunle Xiong, Agata Witkowska, Fetah Benabid, William Wadsworth, Kevin Cook, Alexey Yulin... Each name will bring me a good memory. Thank you all!

Thanks also need to give Dr. Roger Peters for proofreading this thesis. And to Yanwu Guo, Bo Jin, and Shanshan Zeng.

Contents

Chapter 1

Introduction

In the visible and near infrared, far from electronic resonances in the ultraviolet (< 0.5 μm) and vibrational resonances in the mid-infrared (> 2 μm), fused silica exhibits excellent optical transparency. The lowest transmission loss occurs in the regions close to 1.31 and 1.55 μm, the windows used for telecommunications. An optical fiber, the backbone of the information highway, is made from fused silica and conventionally consists of a pure silica cladding and a small core, whose refractive index is slightly increased by germanium doping.

After germanium doping, silica displays another important characteristic: photosensitivity [Hill 78]. UV light irradiation (200-260 nm) causes a permanent change of the refractive index in the near infrared. Exploiting this characteristic, the optical properties of a Ge-core fiber can be manipulated by producing a refractive index modulation along the fiber [Meltz 89], and this refractive index modulation occurs in the Ge-core, where most of the field of the guided mode is distributed.

However, this UV irradiation technique has limitation of a relatively small index contrast. Even with the assistance of the techniques such as hydrogen loading [Lemaire 93], flame brushing [Bilodeau 93], and high-energy laser damage [Archambault 93], the index contrast is less than 0.01. The Ge-doped core is buried inside the pure silica cladding, hence many other micro-fabrication methods, which might result in enhanced functionality, are prohibited.

Although a technology based on fiber side polishing has been used to produce gratings directly in the core region [Russell 85], such devices require careful polarization and mode managements. In the work of this thesis, we instead adopt a fiber tapering technique to gain access to an open waveguide. This technique can produce a perfect transition from the buried waveguide of an un-tapered fiber to the open waveguide of a taper waist with low excess loss [Love 86] and conservation of

cylindrical symmetry. When the taper diameter is reduced to the micron scale, the field of the guided mode spreads out across the boundary of the taper. Structures formed on taper surfaces or inside have significant overlap with the guided modes. Therefore, if the rich family of planar process techniques can be applied to a micron-scale fiber taper, we will benefit from the versatility and a much higher index contrast. To our knowledges, only a few efforts have been made in this direction. For example, Hodzic et al have demonstrated third-order Bragg gratings (the period is three time of that of usual first-order Bragg grating) on fiber tapers using focused-ion-beam milling and implantation [Hodzic 04].

The chapters 2 and 3 of this thesis respectively present the theoretical and fabrication backgrounds used in our works. Then, we demonstrate our attempts to transfer planar process techniques onto the curved surfaces of micron-scale fiber tapers and to identify possible device applications. In chapter 4, two kinds of surface Bragg grating fiber tapers are described. The first one consists of deposited periodic gold strips. A large index contrast is created, and strong mode coupling is observed. The second one contains periodic shallowly etched grooves and only shows grating features in the reflection spectra. Applications of these two devices to refractometric sensing and optical fiber filtering, respectively, are discussed. In chapter 5, another two longitudinally structured fiber tapers are presented. One is made using contact optical lithography and HF etching, and the other by focused-ion-beam milling. Their respective applications as a long period grating, which is a wideband filter, and a micro-cavity waveguide, which is a band-pass filter, are given out.

In chapter 6, our investigations of tapered optical fibers are extended from index-guiding structures to metal/dielectric surface-guiding structures. These surface-guiding modes are known as surface plasmon polaritons (SPPs), and our studies are related to the relatively new field of plasmonics.

At the beginning of this century, three factors triggered a growth of the field of plasmonics [Barnes 03]: the development of nanofabrication techniques, the appearance of near field optical characterisation techniques, and the rapid advance in electromagnetic modelling. Localized surface plasmons [Wokaun 82, Jackson 99, Lamprecht 00, Krenn 00, Maier 02, Hirsch 03, Prodan 03] and surface plasmon polaritons [Burnstein 74, Sarid 81, Prade 91, Al-Bader 93] have found many applications in sensing [Kneipp 02, Mock 03, McFarland 03, Raschke 03],

waveguiding [Maier 01, Bozhevolnyi 01, Ditlbacher 02, Maier 05, Yin 05], and optical microscopy [Reddick 89, Zenhausern 94, Ashino 98, Adam 98].

Different with the mode propagation constant in an index-guiding structure, which has an upper limit determined by the guiding dielectric medium, the propagation constant of a SPP can be greatly enhanced. This enhancement is known as SPP superfocusing [Stockman 04] and has a very important consequence that the mode field can be highly concentrated in space, so that the SPP can access near-field information with high spatial resolution [Bouhelier 03, Stockman 04, Janunts 05].

In chapter 6, theoretical studies of this superfocusing process in a silver-coated fiber tip are carried out with potential applications in scanning near-field optical microscopy. Our analytical model and numerical simulations lead to a comprehensive understanding of how SPP modes can be efficiently excited from fiber waveguide modes and of how this mode conversion is influenced by structure parameters.

In the appendix, one cooperative work completed in my PhD term is presented.

Chapter 2

Background on Electromagnetic Theory

2.1 Introduction

As an electromagnetic wave, light obeys Maxwell's equations, which involve the four macroscopic field variables, **E**, **H**, **D**, and **B**. This chapter briefly reviews the electromagnetic theory of light propagation; analytical and numerical treatment methods are introduced. In the analytical treatments, the weak amplitude assumption is used, so that the electric displacement **D** and the magnetic induction **B** are linear proportional to the applied fields **E** and **H**, and the electromagnetic problem is linear.

The first two sections review light propagation in uniform and non-uniform cylindrical waveguides. The third section describes modal coupling in periodic optical structures. The last two sections briefly introduce two numerical methods of solving Maxwell's equations. All the methods presented in this chapter will be used in later chapters, and this chapter constitutes a theoretical background for the whole thesis.

2.2 Theory of a uniform cylindrical waveguide

Before describing the full mathematical formalism, it is useful to provide an intuitive physical picture for the optical waveguide problem.

2.2.1 Synopsis

The existence of an optical waveguide alters the properties of the electromagnetic fields in neighbourhood. In a homogeneous medium, eigen-modes are plane waves in direction of full solid angle; whereas in a space including an optical waveguide, the eigen-mode can be a guided wave.

The analogy between Maxwell's equations and Schrödinger equation implies that dielectric media can be regarded as optical "potential wells" where photons tend to be localised [Russell 95].

$$[-\frac{\hbar^2}{2m_0}\nabla_t^{\,2} + U_0'(\mathbf{r})]\mathbf{E} - \frac{\hbar^2}{2m_0}\nabla[\{\nabla \ln \varepsilon(\mathbf{r})\}\cdot\mathbf{E}] = -\frac{\hbar^2\beta^2}{2m_0}\mathbf{E} \qquad (2.1)$$

Here, given a fixed angular frequency ω, a uniform waveguide with arbitrary cross section (Fig. 2.1) is considered; the waveguide axis is set to be z direction; β is the propagation constant along the axis; ∇_t denotes the transverse spatial differential operator; $\varepsilon(\mathbf{r})$ is the spatial distribution function of permittivity. Analogy to the terms in Schrödinger equation, $-\hbar^2\beta^2/2m_0$ is the "energy" of the eigen mode; the "optical mass", m_0, and the "potential energy", U_0', are defined as follows:

$$m_0 = \hbar\omega/2c^2 \qquad (2.2a)$$

$$U_0'(\mathbf{r}) = -\hbar\omega\varepsilon(\mathbf{r}) \qquad (2.2b)$$

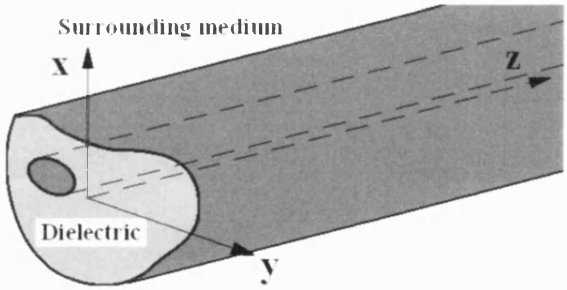

Fig. 2.1. Schematic of a uniform optical waveguide with an arbitrary cross section.

Based on Eqns. (2.1) and (2.2), the language used in quantum mechanics is then be lent to describe the optical waveguide problem. By introducing a waveguide, i.e. an optical "potential well", the continuous "energy band" of the eigen modes in a homogeneous medium, which corresponds to the continuous radiation angle of the plane wave, splits out several discrete "energy levels", which correspond to the guided modes. Fig. 2.2 schematically shows this picture.

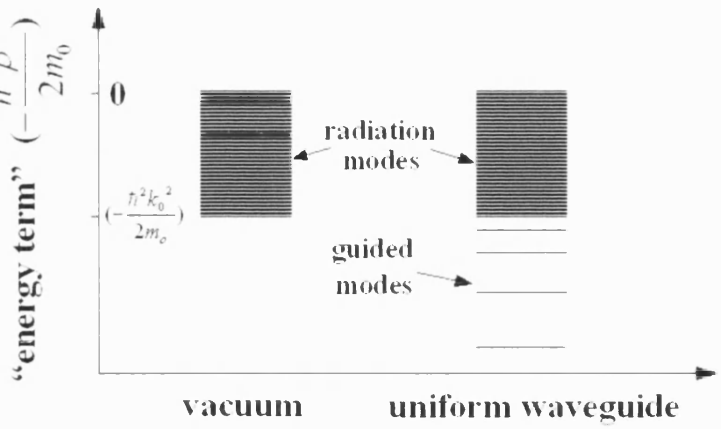

Fig. 2.2. Schematic of the "energy levels".

Mathematically, the optical waveguide problem can also be regarded as a resonant eigen-function problem [Snyder 83]. All the eigen-modes obtained in the waveguide structure are divided into guided modes and radiation modes depending on their transverse field confinement characteristics.

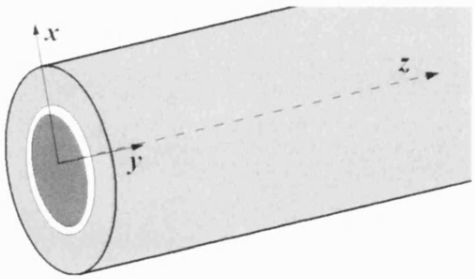

Fig. 2.3. Schematic of a uniform cylindrical waveguide.

Amongst all the uniform waveguides, the cylindrical waveguide (Fig. 2.3) is of most importance, since the widely used optical fibers have such geometry. Fortunately, the precise analytical solution to these uniform cylindrical waveguides exists, and this thesis mainly considers such waveguides.

2.2.2 Maxwell's equations

Maxwell's equations (in **SI** units) can be expressed as,

$$\begin{cases} \nabla \times \mathbf{E} = -\partial \mathbf{B}/\partial t & \text{(Faraday's law)} \\ \nabla \times \mathbf{H} = \partial \mathbf{D}/\partial t + \mathbf{J} & \text{(Ampere's law)} \\ \nabla \cdot \mathbf{D} = \rho & \text{(Gauss's law)} \\ \nabla \cdot \mathbf{B} = 0 & \text{(Gauss's law for magnetism)} \end{cases} \tag{2.3}$$

where **E**, **H**, **D**, and **B** are electric and magnetic fields, electric displacement, and magnetic induction respectively. The charge density, ρ, and the current density, **J**, are the sources of the fields. The linear optical response of an isotropic medium can be expressed in terms of the scalar electric permittivity, ε, and magnetic permeability, μ.

$$\begin{cases} \mathbf{D} = \varepsilon \mathbf{E} \\ \mathbf{B} = \mu \mathbf{H} \end{cases} \tag{2.4}$$

Not introducing any new physics, Maxwell's equations can also be expressed in terms of vector and scalar potentials (**A** and ϕ) [Ishimaru 91], whose definitions are as follows:

$$\begin{cases} \mathbf{B} = \nabla \times \mathbf{A} \\ \mathbf{E} = -\partial \mathbf{A}/\partial t - \nabla \phi \end{cases} \tag{2.5}$$

From Eqn. (2.5), Gauss's law and Ampere's law of Maxwell's equations are written as [Ishimaru 91],

$$\begin{cases} -\mu\varepsilon \dfrac{\partial^2 \phi}{\partial t^2} + \nabla^2 \phi = -\dfrac{\rho}{\varepsilon} \\ \nabla^2 \mathbf{A} - \mu\varepsilon \dfrac{\partial^2 \mathbf{A}}{\partial t^2} = -\mu \mathbf{J} \end{cases} \tag{2.6}$$

where the Lorentz gauge is used:

$$\nabla \cdot \mathbf{A} + \mu\varepsilon \cdot \partial \phi / \partial t = 0 \tag{2.7}$$

Using the vector and scalar potentials (**A** and ϕ), Maxwell's equations (2.6) and (2.7) are solved in each homogeneous dielectric region, and then all solutions are related to each other by using Eqn. (2.5) and the boundary continuity conditions:

$$\begin{cases} \mathbf{E}_{1t} = \mathbf{E}_{2t} \\ \mathbf{B}_{1n} = \mathbf{B}_{2n} \end{cases} \quad \begin{cases} \mathbf{D}_{1n} - \mathbf{D}_{2n} = \mathbf{Q} \\ \mathbf{n} \times (\mathbf{H}_{1t} - \mathbf{H}_{2t}) = \mathbf{K} \end{cases} \tag{2.8}$$

Here, the subscripts 1 and 2 denote two adjacent media, and t and n represent transverse and normal directions of the boundary. **Q** and **K** are the surface charge and current densities respectively.

2.2.3 Hertz vector method

To the wave propagation problem in a uniform cylindrical waveguide, the Hertz vector method provides a much simpler solution. Using the Hertz vector method, the above-mentioned vector and scalar potentials (**A** and ϕ) and the Lorentz gauge (Eqn. 2.7) can be combined into one equation.

Firstly, an electric Hertz vector $\boldsymbol{\pi}$ is defined as follows [Ishimaru 91]:

$$\begin{cases} \mathbf{A} = \mu\varepsilon \cdot \partial\boldsymbol{\pi}/\partial t \\ \phi = -\nabla \cdot \boldsymbol{\pi} \end{cases} \tag{2.9}$$

By introducing an "electric polarization vector" **P** defined by $\mathbf{J} = \partial\mathbf{P}/\partial t$ and $\rho = -\nabla \cdot \mathbf{P}$, Maxwell's equations are transformed to,

$$\nabla^2\boldsymbol{\pi} - \mu\varepsilon \cdot \partial^2\boldsymbol{\pi}/\partial t^2 = -\mathbf{P}/\varepsilon \tag{2.10}$$

The electromagnetic fields are related to $\boldsymbol{\pi}$ and **P** by,

$$\begin{cases} \mathbf{E} = -\mu\varepsilon \cdot \partial^2\boldsymbol{\pi}/\partial t^2 + \nabla(\nabla \cdot \boldsymbol{\pi}) = \nabla \times (\nabla \times \boldsymbol{\pi}) - \mathbf{P}/\varepsilon \\ \mathbf{H} = \varepsilon\nabla \times \partial\boldsymbol{\pi}/\partial t \end{cases} \tag{2.11}$$

In Eqn. (2.11), magnetic sources are ignored. Making use of the electric-magnetic Duality Principle and introducing the imaginary magnetic charge density ρ_m and the magnetic current density $\mathbf{J}_m$ into Eqns. (2.3), the magnetic Hertz vector $\boldsymbol{\pi}_m$ can also be defined. The complete expressions for Maxwell's equations and the electromagnetic fields are,

$$\begin{cases} \nabla^2\boldsymbol{\pi} - \mu\varepsilon \cdot \partial^2\boldsymbol{\pi}/\partial t^2 = -\mathbf{P}/\varepsilon \\ \nabla^2\boldsymbol{\pi}_m - \mu\varepsilon \cdot \partial^2\boldsymbol{\pi}_m/\partial t^2 = 0 \end{cases} \tag{2.12}$$

$$\begin{cases} \mathbf{E} = \nabla \times (\nabla \times \boldsymbol{\pi} - \mu\,\partial\boldsymbol{\pi}_m/\partial t) - \mathbf{P}/\varepsilon \\ \mathbf{H} = \nabla \times (\nabla \times \boldsymbol{\pi}_m) + \varepsilon\nabla \times \partial\boldsymbol{\pi}/\partial t \end{cases} \tag{2.13}$$

Similar to the vector and scalar potential method, the Hertz vector method also needs to define different $\boldsymbol{\pi}$ and $\boldsymbol{\pi}_m$ in different homogeneous dielectric region and then relates them using the boundary continuity conditions of Eqn. (2.8).

2.2.4 HE/EH hybrid modes

In a source-free uniform cylindrical waveguide, the different characteristics of the TM, TE and HE/EH hybrid modes can be easily categorized by the following conditions:

$$\begin{cases} \boldsymbol{\pi} = \pi_z(\mathbf{r})\mathbf{a}_z \\ \boldsymbol{\pi} = 0 \\ \boldsymbol{\pi} = \pi_z(\mathbf{r})\mathbf{a}_z \end{cases}, \begin{cases} \boldsymbol{\pi}_m = 0 & \text{(for TM modes)} \\ \boldsymbol{\pi}_m = \pi_{mz}(\mathbf{r})\mathbf{a}_z & \text{(for TE modes)} \\ \boldsymbol{\pi}_m = \pi_{mz}(\mathbf{r})\mathbf{a}_z & \text{(for HE/EH modes)} \end{cases} \tag{2.14}$$

where $\mathbf{a}_z$ is the unit vector along the axis. The TM and TE modes have only azimuthal magnetic and electric fields respectively, while the HE/EH hybrid modes have both.

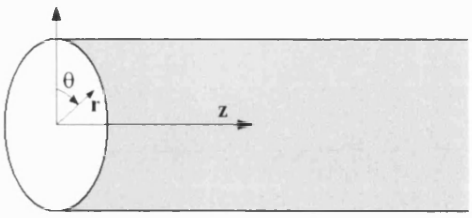

Fig. 2.4. A cylindrical coordinate with the notation of (r, θ, z).

In the cylindrical coordinate system shown in Fig. 2.4, substituting Eqn. (2.14) into Eqns. (2.12) and (2.13) gives the Hertz vector equations of HE/EH hybrid modes as follows:

$$\begin{cases} [\dfrac{\partial^2}{\partial r^2}+\dfrac{\partial}{r\partial r}+\dfrac{\partial^2}{r^2\partial\theta^2}]\pi_z - k_C{}^2\pi_z = 0 \\ [\dfrac{\partial^2}{\partial r^2}+\dfrac{\partial}{r\partial r}+\dfrac{\partial^2}{r^2\partial\theta^2}]\pi_{zm} - k_C{}^2\pi_{zm} = 0 \end{cases} \qquad (2.15)$$
$$k_C = \sqrt{\beta^2 - n^2(r)k_0{}^2}$$

The corresponding fields are

$$\begin{cases} E_z = -k_C{}^2\pi_z \\ E_r = i\beta\partial\pi_z/\partial r - \nu\omega\mu\,\pi_{zm}/r \\ E_\theta = -\nu\beta\,\pi_z/r - i\omega\mu\,\partial\pi_{zm}/\partial r \end{cases}, \begin{cases} H_z = -k_C{}^2\pi_{zm} \\ H_r = \nu\omega\varepsilon\,\pi_z/r + i\beta\partial\pi_{zm}/\partial r \\ H_\theta = i\omega\varepsilon\,\partial\pi_z/\partial r - \nu\beta\,\pi_{zm}/r \end{cases} \qquad (2.16)$$

where ω is the angular frequency, k_0 is the vacuum wavevector, β is the propagation constant along the axis z, $n(r)$ and $\varepsilon(r)$ are the spatial functions of refractive index and permittivity respectively, μ is the vacuum magnetic permeability, and ν = 1,2,3... represents the azimuthal order of the modes.

In each dielectric region, the solutions of (2.15) are,

$$\begin{cases} \pi_z = [A_1 I_\nu(k_C r) + A_2 K_\nu(k_C r)]\exp[i(\nu\theta + \beta z - \omega t)] \\ \pi_{zm} = [B_1 I_\nu(k_C r) + B_2 K_\nu(k_C r)]\exp[i(\nu\theta + \beta z - \omega t)] \end{cases} \qquad (2.17)$$

where I_ν and K_ν are respectively the modified Bessel functions of the 1st and 2nd kinds, $A_{1,2}$ and $B_{1,2}$ are undetermined coefficients, and k_C is defined in Eqn. (2.15).

Applying the boundary conditions of Eqn. (2.8), equations in matrix form are obtained [Al-Bader 93]:

$$\begin{bmatrix} E_z^{(j)}(r=a_j) \\ E_\theta^{(j)}(r=a_j) \\ H_z^{(j)}(r=a_j) \\ H_\theta^{(j)}(r=a_j) \end{bmatrix} = \mathbf{M}_j^{(+)} \begin{bmatrix} A_1^{(j)} \\ A_2^{(j)} \\ B_1^{(j)} \\ B_2^{(j)} \end{bmatrix} = \mathbf{M}_{j+1}^{(-)} \begin{bmatrix} A_1^{(j+1)} \\ A_2^{(j+1)} \\ B_1^{(j+1)} \\ B_2^{(j+1)} \end{bmatrix} = \begin{bmatrix} E_z^{(j+1)}(r=a_j) \\ E_\theta^{(j+1)}(r=a_j) \\ H_z^{(j+1)}(r=a_j) \\ H_\theta^{(j+1)}(r=a_j) \end{bmatrix} \qquad (2.18)$$

Here, the waveguide is assumed to consist of N layers of cylindrical dielectric. The superscript j denotes the j^{th} layer from the axis, the superscripts (+) and (-) denote the outer and inner boundaries of the layer respectively, $r = a_j$ represents the interface between the j^{th} and $(j+1)^{th}$ layers. The matrix $\mathbf{M}_j$ is derived from (2.16) and the boundary conditions (2.8). Taking into account the asymptotic properties of the field approaching the axis and infinity, two more boundary conditions $A_2^{(1)} = B_2^{(1)} = 0$ and $A_1^{(N)} = B_1^{(N)} = 0$ are obtained.

Repeatedly using Eqn. (2.18) gives a relationship between $(A_1^{(1)}, B_1^{(1)})$ and $(A_2^{(N)}, B_2^{(N)})$,

$$\mathbf{M}\begin{bmatrix} A_1^{(1)} \\ B_1^{(1)} \\ A_2^{(N)} \\ B_2^{(N)} \end{bmatrix} = 0 \tag{2.19}$$

where the matrix $\mathbf{M}$ is a derivative of Eqns. (2.18).

The eigen-values are obtained by the condition,

$$\det(\mathbf{M}) = 0, \tag{2.20}$$

and the eigen-modes are solved by calculating coefficients $(A_{1,2}^{(j)}, B_{1,2}^{(j)})$ in Eqns. (2.18) and (2.19).

The above process steps, from (2.15) to (2.20), are also suitable for TM and TE modes in uniform cylindrical waveguides, where Eqn. (2.14) should be noticed. Fig. 2.5 schematically shows the whole flow chart of this process.

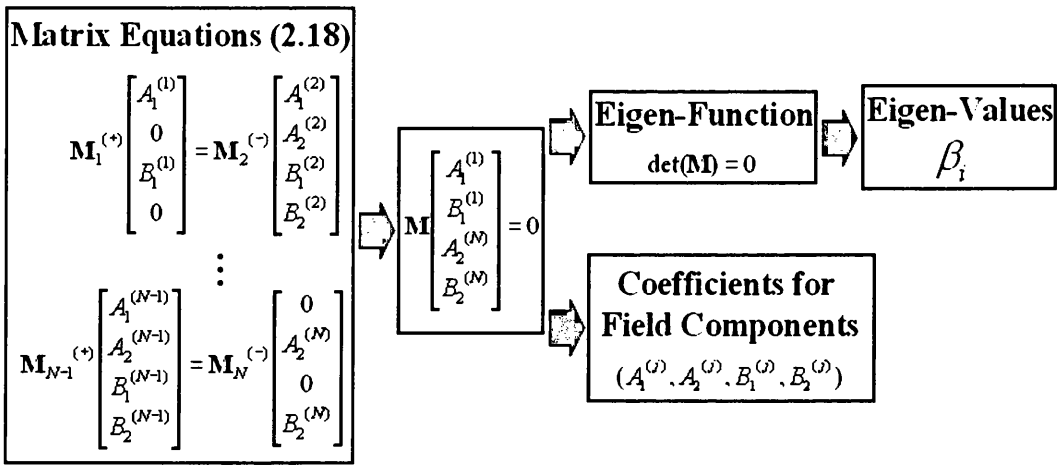

Fig. 2.5. Flow chart of how to solve the eigen-mode problem in a uniform cylindrical waveguide.

The Hertz vector method and the matrix operation process are core analytical tools in this thesis. They will be used in the theoretical parts of chapter 4, 5, and 6.

2.3 Local mode theory of a non-uniform cylindrical waveguide

In a non-uniform cylindrical waveguide, due to lose of translational symmetry, the eigen-modes described in the last section do not exist. Generally speaking, it is difficult to give out exact solutions of Maxwell's equations for such waveguides. Nevertheless, if the non-uniformity is small, the local mode can be expressed as a superposition of the eigen-modes of the assumed uniform waveguide as shown in Fig. 2.6b. The evolution of the local mode along the waveguide can be represented by the evolution of the distribution function in this eigen-mode expansion [Snyder 83]. This section briefly reviews the local mode theory in a cylindrical waveguide with slowly varying cross-section.

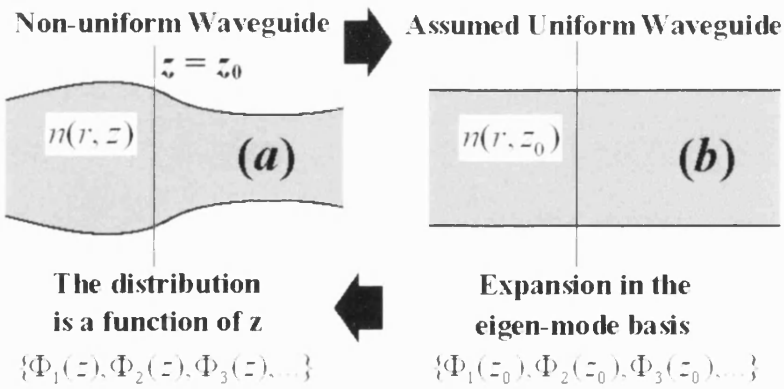

Fig. 2.6. Local modes in a slowly varying waveguide.

Assuming the j^{th} order eigen-mode in the assumed uniform waveguide (Fig. 2.6b) to be

$$\begin{cases} \mathbf{E}_j = \frac{1}{2}[\mathbf{e}_j(x,y)e^{i[\beta_j(z_0)z-\omega t]} + c.c.] \\ \mathbf{H}_j = \frac{1}{2}[\mathbf{h}_j(x,y)e^{i[\beta_j(z_0)z-\omega t]} + c.c.] \end{cases} \tag{2.21}$$

As stated above, the local mode in the non-uniform waveguide (Fig. 2.6a) can be expressed as,

$$\begin{cases} \mathbf{E}_t(x,y,z) = \frac{1}{2}\{\sum_j b_j(z)\hat{\mathbf{e}}_{tj}(x,y,\beta_j(z))e^{-i\omega t} + c.c.\} \\ \mathbf{H}_t(x,y,z) = \frac{1}{2}\{\sum_j b_j(z)\hat{\mathbf{h}}_{tj}(x,y,\beta_j(z))e^{-i\omega t} + c.c.\} \end{cases} \tag{2.22}$$

where the subscript t denotes the transverse component, $\wedge$ denotes the normalization to the mode, $b_j(z)$ and $\beta_j(z)$ are the complex amplitude and the propagation constant of the mode, respectively. The ortho-normalization condition is,

$$\frac{1}{2}\int_{A_\infty}[\hat{\mathbf{e}}_j \times \hat{\mathbf{h}}_l^*]\cdot\mathbf{a}_z dA = \frac{1}{2}\int_{A_\infty}[\hat{\mathbf{e}}_l^* \times \hat{\mathbf{h}}_j]\cdot\mathbf{a}_z dA = \begin{cases} 1 & \text{if } j = l \\ 0 & \text{if } j \neq l \end{cases} \tag{2.23}$$

Substituting Eqn. (2.22) into Maxwell's equations and using Eqn. (2.23), the coupled local mode equations is found to be,

$$db_j(z)/dz = i\beta_j(z)b_j + \sum_l C_{jl}b_l(z) \tag{2.24}$$

The coupling coefficient C_{jl} represents the strength of the coupling from the mode l to the mode j, and can be expressed as,

$$C_{jl} = \frac{1}{4}\int_{A_\infty}\{\hat{\mathbf{h}}_j \times \frac{\partial \mathbf{e}_l}{\partial z} - \hat{\mathbf{e}}_j \times \frac{\partial \hat{\mathbf{h}}_l}{\partial z}\}\cdot\mathbf{a}_z dA, \qquad j \neq l; \qquad C_{jj} = 0 \tag{2.25}$$

For a non-absorbing waveguide, Eqn. (2.25) can be further deduced to, [Snyder 83]

$$C_{jl} = \frac{\omega\varepsilon_0}{4(\beta_j - \beta_l)}\int_{A_\infty}\hat{\mathbf{e}}_j^* \cdot \hat{\mathbf{e}}_l \frac{\partial n^2}{\partial z} dA \tag{2.26}$$

In chapter 6, the above analysis will be used to investigate mode conversion and evolution in a fiber tip.

2.4 Periodic optical structures

Introducing periodicity into optical structures is a conventional method to obtain plentiful optical functionality. Such structures include all kinds of gratings with different period length scales. Generally speaking, it is difficult to provide analytical solutions for various periodic structures. Here, we just discuss several simple but important examples and present the well-known transfer matrix method and perturbation theory.

2.4.1 Transfer matrix method

The simplest example of periodic optical structure consists of alternating layers of two different dielectrics. Based on the Bloch-Floquet theorem, which arises from the periodictranslational symmetry of the structures, precise solutions to the eigen-modes of these periodic stack structures can be obtained. This technique is called transfer matrix method (TMM) [Ishimaru 91].

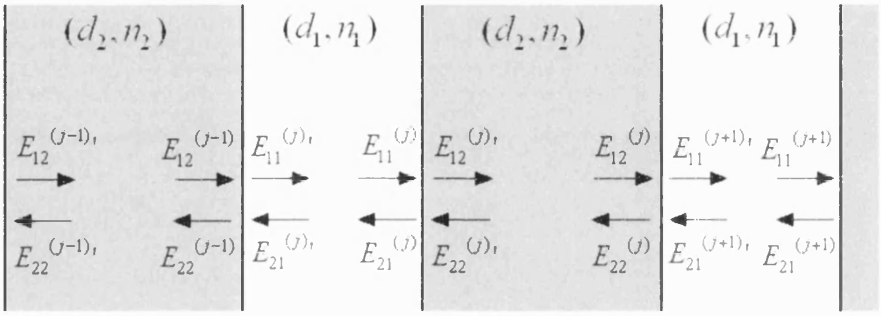

Fig. 2.7. Periodic alternating layers of two different dielectrics.

In the normal incidence case (Fig. 2.7), the field has the form of a transverse electromagnetic (TEM) wave. Applying Fresnel's law, the Bloch wave in this periodic structure can be expressed as,

$$M\begin{bmatrix} E_{11}^{(j)} \\ E_{21}^{(j)} \end{bmatrix} = \begin{bmatrix} E_{11}^{(j+1)} \\ E_{21}^{(j+1)} \end{bmatrix} = e^{ik_B(d_1+d_2)}\begin{bmatrix} E_{11}^{(j)} \\ E_{21}^{(j)} \end{bmatrix} \tag{2.27}$$

$$M = \begin{bmatrix} e^{ik_0 n_1 d_1} & 0 \\ 0 & e^{-ik_0 n_1 d_1} \end{bmatrix} \begin{bmatrix} \frac{n_1+n_2}{2n_1} & \frac{n_1-n_2}{2n_1} \\ \frac{n_1-n_2}{2n_1} & \frac{n_1+n_2}{2n_1} \end{bmatrix} \begin{bmatrix} e^{ik_0 n_2 d_2} & 0 \\ 0 & e^{-ik_0 n_2 d_2} \end{bmatrix} \begin{bmatrix} \frac{n_1+n_2}{2n_2} & \frac{n_2-n_1}{2n_2} \\ \frac{n_2-n_1}{2n_2} & \frac{n_1+n_2}{2n_2} \end{bmatrix} \tag{2.28}$$

Here, k_0 is the vacuum wavevector, k_B is the Bloch wavevector, d and n are the thickness and the refractive index of the dielectric layer. The eigen-function is,

$$e^{ik_B(d_1+d_2)} = [M_{11} + M_{22} \pm \sqrt{(M_{11}+M_{22})^2 - 4}]/2 \tag{2.29}$$

In the oblique incidence case, polarization dependence should be taken into account in Fresnel's law.

Using the transfer matrix method, apart from the eigen-modes, transmittance and reflectivity of multi-layer stacks can also be calculated. In the appendix A2, the transfer matrix method will be used to deal with one-dimensional photonic crystal structures.

2.4.2 Perturbation theory

If periodic structures are incorporated into a uniform waveguide, mode coupling occurs when the resonance condition is satisfied. Such examples include fiber gratings, electro-optic or acousto-optic gratings, and surface corrugation gratings. In order to solve these gratings, perturbation theory, which supposes that the influence of the grating to the waveguide eigen-modes is small, is adopted [Yariv 97].

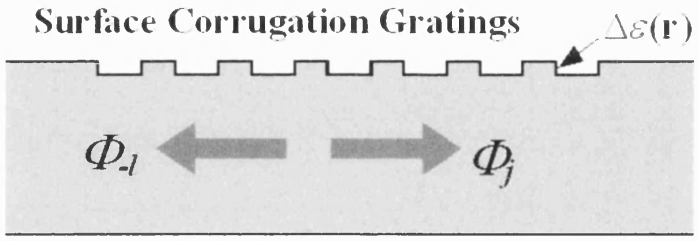

Fig. 2.8. Mode couplings caused by surface corrugation gratings.

As a starting point, we write out the source-free wave equation in the form of the Helmholtz equation [Yariv 97],

$$\nabla^2\mathbf{E}(\mathbf{r},t)-\mu\varepsilon(\mathbf{r})\partial^2\mathbf{E}(\mathbf{r},t)/\partial t^2=\mu\partial^2\mathbf{P}_{pert}(\mathbf{r},t)/\partial t^2 \tag{2.30}$$

where $\mathbf{E}(\mathbf{r},t)$ is the total electric field, and $\varepsilon(\mathbf{r})$ is the permittivity distribution in the unperturbed waveguide. The perturbation polarization $\mathbf{P}_{pert}(\mathbf{r},t)$ arises from the grating induced permittivity modulation $\Delta\varepsilon(\mathbf{r})$ (see Fig. 2.8).

$$\mathbf{P}_{pert}(\mathbf{r},t)=\Delta\varepsilon(\mathbf{r})\mathbf{E}(\mathbf{r},t) \tag{2.31}$$

Expanding $\mathbf{E}(\mathbf{r},t)$ in the basis of the eigen-modes of the unperturbed waveguide,

$$\mathbf{E}(\mathbf{r},t)=\frac{1}{2}\sum_j[A_j(z)\hat{\mathbf{e}}_j e^{i(\beta_j z-\omega t)}+c.c.] \tag{2.32}$$

If we substitute Eqn. (2.32) into Eqn.(2.30) and assume a slow variation of A_j

$$\left|d^2A_j/dz^2\right|<<\beta_j\left|dA_j/dz\right|, \tag{2.33}$$

the Helmholtz equation (2.30) becomes:

$$\sum_j[i\beta_j\frac{dA_j}{dz}\hat{\mathbf{e}}_j e^{i(\beta_j z-\omega t)}+c.c.]=\mu\frac{\partial^2}{\partial t^2}\mathbf{P}_{pert}(\mathbf{r},t) \tag{2.34}$$

Using the mode orthonormalization conditions of Eqn. (2.23), the coupled mode equations are,

$$\frac{dA_j}{dz}e^{i(\beta_j z-\omega t)}-\frac{dA_{-j}}{dz}e^{i(-\beta_j z-\omega t)}-c.c.=\frac{-i\mu}{2\beta_j}\frac{\partial^2}{\partial t^2}\int_{A_\infty}[\mathbf{P}_{pert}(\mathbf{r},t)\times\hat{\mathbf{h}}_j^{\,*}]\cdot\mathbf{a}_z dA \quad (2.35)$$

where the subscript $-j$ denotes a backward propagating mode. In the deduction of Eqn. (2.35), the following relation between two counter-propagating modes in a non-absorbing wave-guide is used [Snyder 83]:

$$\begin{cases}\mathbf{e}_{-j}=\mathbf{e}_{tj}-e_{zj}\mathbf{a}_z\\ \mathbf{h}_{-j}=-\mathbf{h}_{tj}+h_{zj}\mathbf{a}_z\end{cases} \quad (2.36)$$

In chapter 4, this mode coupling equation will be used to deal with Bragg grating fiber tapers.

2.5 Finite difference time domain technique

The techniques described in last three sections can only be used in a very limited range of geometries. In most complicated cases, numerical simulations are necessary. One such technique is the finite difference time domain method (FDTD), whose foundation is based on the discretization of Maxwell's equations on spatial grids and time steps [Yee 66].

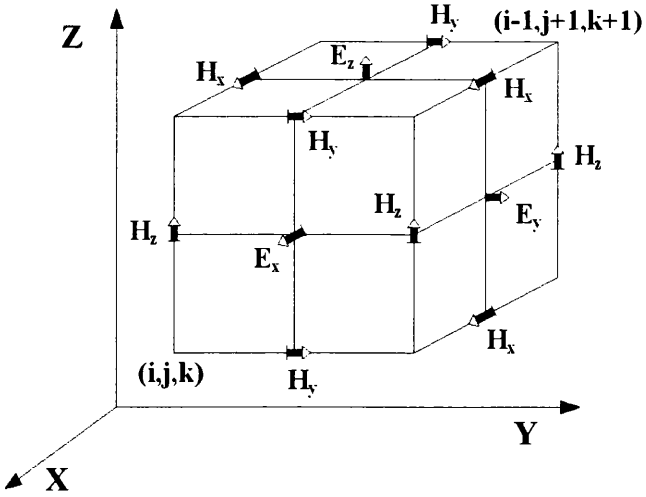

Fig. 2.9. Electric and magnetic field vector components in a cubic Yee lattice.

FDTD, invented by Kane Yee in 1966, is based on solving Maxwell's curl equations and making discrete sampling of the electric and magnetic fields in spatial grids and time steps. Fig. 2.9 shows these grid lattices, and (i,j,k) represent the grid

indices. The Yee discretized expressions for Ampere's law and Faraday's law can then be written as:

$$\frac{E_x\big|_{i,j+1/2,k+1/2}^{n+1/2} - E_x\big|_{i,j+1/2,k+1/2}^{n-1/2}}{\Delta t} = \frac{1}{\varepsilon_{i,j+1/2,k+1/2}} \left(\begin{array}{l} \dfrac{H_z\big|_{i,j+1,k+1/2}^{n} - H_z\big|_{i,j,k+1/2}^{n}}{\Delta y} - \dfrac{H_y\big|_{i,j+1/2,k+1}^{n} - H_y\big|_{i,j+1/2,k}^{n}}{\Delta z} \\ - J_x\big|_{i,j+1/2,k+1/2}^{n} - \sigma_{i,j+1/2,k+1/2} \left(\dfrac{E_x\big|_{i,j+1/2,k+1/2}^{n+1/2} + E_x\big|_{i,j+1/2,k+1/2}^{n-1/2}}{2} \right) \end{array} \right) \tag{2.37}$$

$$\frac{H_x\big|_{i-1/2,j+1,k+1}^{n+1} - H_x\big|_{i-1/2,j+1,k+1}^{n}}{\Delta t} = \frac{1}{\mu_{i-1/2,j+1,k+1}} \left(\begin{array}{l} \dfrac{E_y\big|_{i-1/2,j+1,k+3/2}^{n+1/2} - E_y\big|_{i-1/2,j+1,k+1/2}^{n+1/2}}{\Delta z} - \dfrac{E_z\big|_{i-1/2,j+3/2,k+1}^{n+1/2} - E_z\big|_{i-1/2,j+1/2,k+1}^{n+1/2}}{\Delta y} \\ - M_x\big|_{i-1/2,j+1,k+1}^{n+1/2} - \sigma^*_{i-1/2,j+1,k+1} \left(\dfrac{H_x\big|_{i-1/2,j+1,k+1}^{n+1} + H_x\big|_{i-1/2,j+1,k+1}^{n}}{2} \right) \end{array} \right) \tag{2.38}$$

Here, the sub- and super-scripts refer to the spatial and time positions respectively. Apart from the electric and magnetic fields, E and H, the electric and magnetic current densities, J and M, are also included in equations. σ and σ^* are the electric and magnetic conductivities, respectively. The other four partial differential equations corresponding to the other field components in y and z directions have similar forms.

In Eqns. (2.37) and (2.38), the spatial and time discretizations of the **E** and **H** fields are carried out in two sets of staggered spatial lattices (see Fig. 2.9) and leap-frog time steps. These arrangements ensure that the Yee algorithm is accurate to second-order. Field-material interactions, such as dissipation, gain, dispersion, non-linearity, and non-locality, can be easily incorporated into these equations. In addition, the FDTD method also needs a boundary condition that allows outward-propagating waves to exit the simulation space without causing significant reflection artefacts. The detailed introduction to the FDTD technique can be found in [Taflove 97].

In chapter 5, a commercial FDTD package named as OptiFDTD [OptiFDTD 5.0] is used to simulate micro-cavity structures in fiber tapers. This package is a powerful full 3D simulator, provides absorbing boundaries, and can model materials with anisotropy and dispersion. In simulation, the dispersion of the dielectric permittivity is described as a sum of resonances (Lorentz oscillator).

$$\varepsilon(\omega) = \varepsilon_{\infty} + \sum_{m=1}^{N} \frac{\Omega_m^{\ 2}}{\omega_m^{\ 2} + i\Gamma_m \omega - \omega^2} \tag{2.39}$$

where ε_{∞} is the relative permittivity in the infinity frequency, Ω_m is the plasma frequency, ω_m is the resonant frequency, and Γ_m is the damping factor [OptiFDTD 5.0].

2.6 Finite integration technique

A decade after Yee's time domain approach, another discretization theory based on integral formulation of Maxwell's equations (Maxwell's grid equations, MGE) was proposed by Weiland [Weiland 77]. The corresponding simulation method is known as Finite Integration Technique (FIT). A merit of FIT is the possibility of accurately modelling curved structures, whereas classical FDTD methods are limited to staircase approximations of complex boundaries.

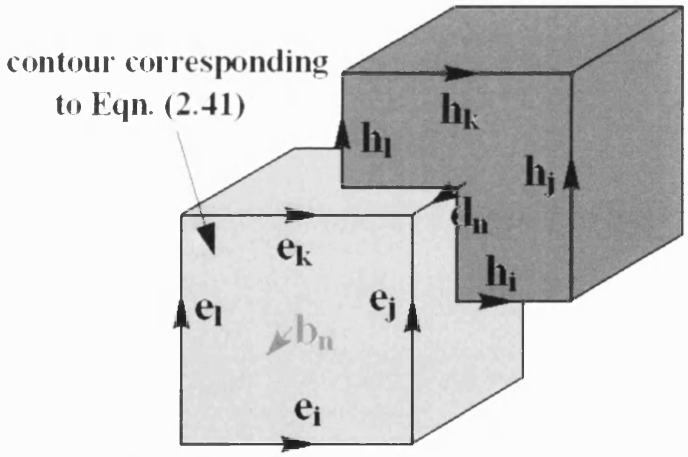

Fig. 2.10. Two orthogonal grid systems.

By creating two orthogonal grid lattices **G** and $\tilde{\mathbf{G}}$ as shown in Fig. 2.10, the spatial discretization of Maxwell's equations is equivalently rewritten as the so-called MGEs. The electric grid voltages **e**, which are the integral values along corresponding grid edges, and the magnetic facet fluxes **b**, which are the integral values across the grid faces, constitute the Faraday's law contour on the primary grid **G**. Both **e** and **b** include distributive information of respective fields, so that no discretization error is introduced. Similarly, the magnetic grid voltages **h** and dielectric facet fluxes **d**

constitute the Ampere's law contour on the dual grid $\tilde{\mathbf{G}}$. The complete discretized set of MGE's can be expressed as,

$$\begin{cases} \mathbf{Ce} = -d\mathbf{b}/dt & \text{Faraday's law} \\ \tilde{\mathbf{C}}\mathbf{h} = d\mathbf{d}/dt + \mathbf{j} & \text{Ampere's law} \\ \mathbf{Sb} = 0 & \text{magnetic Gauss's law} \\ \tilde{\mathbf{S}}\mathbf{d} = q & \text{electric Gauss's law} \end{cases} \tag{2.40}$$

Here, the curl and divergence operators in the continuous form of Maxwell's equations are represented by the matrixes of **C** and **S**. For example, the first formula in Eqn. (2.40) can be expressed as (see the contour shown in Fig. 2.10),

$$\begin{pmatrix} & & & & & \cdot\ \cdot\ \cdot & & & & & \\ 1 & \cdot & 0 & \cdot & 1 & \cdot & 0 & \cdot & -1 & \cdot & 0 & \cdot & -1 \\ & & & & & \cdot\ \cdot\ \cdot & & & & & \end{pmatrix} \begin{pmatrix} e_i \\ \cdot \\ e_j \\ \cdot \\ e_k \\ \cdot \\ e_l \end{pmatrix} = -\frac{d}{dt} \begin{pmatrix} \cdot \\ b_n \\ \cdot \end{pmatrix} \tag{2.41}$$

In addition, the relations between voltages and fluxes can also be expressed in matrix form.

$$\begin{cases} \mathbf{d} = \mathbf{M}_\varepsilon \mathbf{e} \\ \mathbf{b} = \mathbf{M}_\mu \mathbf{h} \\ \mathbf{j} = \mathbf{M}_\sigma \mathbf{e} + \mathbf{j}_S \end{cases} \tag{2.42}$$

where **e**, **h**, **d**, **b**, and **j** are vectors and the **M**'s are matrices. In practical applications, this step of Eqn. (2.42) usually introduces numerical inaccuracy due to the spatial discretization.

In chapter 6, a commercial 3D FIT simulator, CST microwave studio [CST microwave studio 2006], is used to calculate the surface plasmon polaritons in a silver-coated fiber tip.

Chapter 3

Fiber Tapering, Planar Processing, and Interference Lithography Techniques

3.1 Introduction

This chapter provides a brief review of the fabrication techniques used in our works. The sections 3.2 and 3.3 introduce a fiber tapering technique and several basic planar processing techniques, respectively. The last section describes an interference lithography technique. A multi-beam interference exposure system with phase-shift stabilisation is also presented.

3.2 Fiber tapering technique

An optical fiber taper consists of a slim waist and two gradually varied transitions as shown in Fig. 3.1 [Birks 92]. The transition part is an optical link, which connects the un-tapered fiber (a buried waveguide) and the taper waist (an open waveguide) and functions as a mode converter. In the un-tapered fiber region, the propagating mode is confined in the high-index core, and the effective modal index of the core mode separates with those of the cladding modes, which are due to the index contrast between the cladding and the environment. In Fig. 3.1, we plot a single mode fiber, which supports only one core mode. While, in the taper transition region, the core gradually decreases as the fiber diameter decreases. A micron-scale taper waist can be simply regarded as a pure silica cylinder suspended in the environment, and that is a multi-mode waveguide. Thus way, through the taper transitions, the core and cladding modes in the un-tapered fiber are respectively converted to the fundamental and high-order modes in the taper waist as schematically shown in Fig. 3.1.

However, in many cases, confining optical energy in one mode is beneficial. This can be achieved by an adiabatic taper transition [Love 91], where the energy transfer between different modes is negligible. Via such an adiabatic taper transition, a single-mode un-tapered fiber can only excite the fundamental mode in taper waist region.

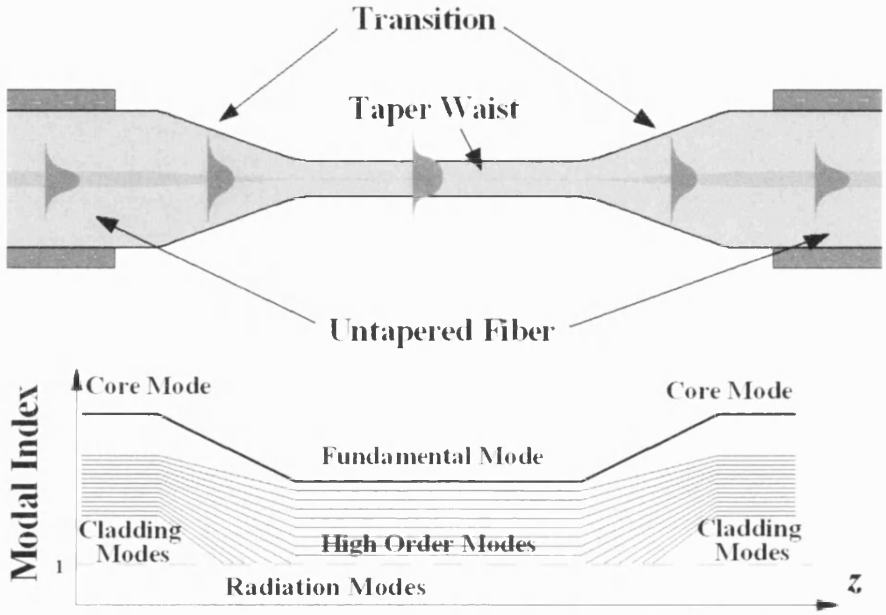

Fig. 3.1. Schematic of a tapered fiber and the evolution of the effective modal index.

For adiabatic propagation to occur, the taper transition has to vary quite slowly in the sense that the local taper length-scale, L_t, is larger than the coupling length-scale, L_b, between relevant modes [Love 91]. The adiabaticity criterion is thus expressed as:

$$L_t(z) \approx \frac{r(z)}{\alpha} > \frac{2\pi}{\beta_1(z) - \beta_2(z)} = L_b(z) \tag{3.1}$$

where z is the axial coordinate, $\beta_{1,2}$ are the propagation constants of the fundamental mode and the most adjacent high-order mode in the transition part, respectively, r is the fiber radius, and $\alpha = |dr(z)/dz|$ is the decreasing slope of the fiber radius along the axis.

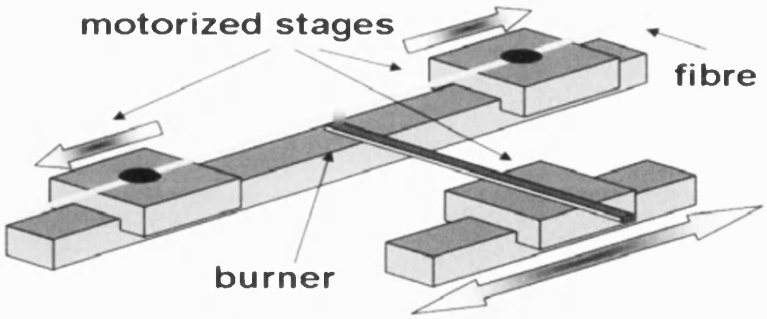

Fig. 3.2. Schematic of the taper rig (courtesy Sergio Leon-Saval).

For fabricating tapers, a "taper rig" consisting of two motorized stages is used to stretch a fiber, whilst another motorized burner stage provides an oxy-butane flame [Birks 92]. The synchronous motion of these three stages is controlled by a LabVIEW program. The "flame brush" moves to and fro along the fiber as the other two stages pull apart. Controlled taper transitions and long uniform taper waists can be produced. Fig. 3.2 shows a schematic of this taper rig. Using this apparatus, a conventional Corning SMF-28 fiber is tapered down to ~10 μm diameter in our works. When the taper waist is 10 cm long and the taper transitions are 2.5 cm long, the transmission loss is typically less than 0.1 dB at a wavelength of 1.55 μm.

3.3 Basic planar processing techniques

In this section, several basic planar processing techniques are described. These include resist dip coating, contact optical lithography, thermal evaporation deposition, chemical wet etching, reactive ion etching, and focused ion beam milling.

3.3.1 Resist dip coating and contact optical lithography

Dip coating is a conventional resist application method, which consists of immersing a sample into a resist tank, withdrawing it at certain rate, and leaving it to dry. Fig. 3.3 shows this process schematically. In the resist dip coating, the resist viscosity and the withdrawal rate are two important parameters, which determine the thickness of the applied resist film.

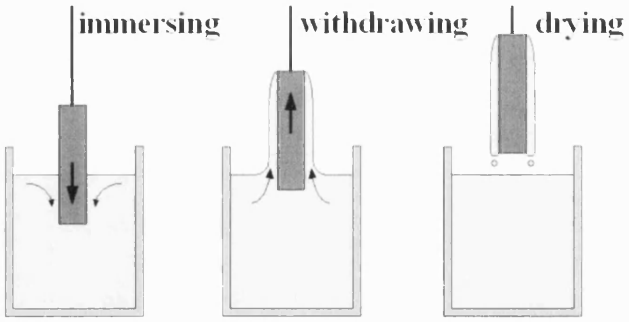

Fig. 3.3. Schematic of the dip-coating process.

After applying a resist film, we can imprint patterns onto this resist layer using contact optical lithography as shown in Fig. 3.4. The image on an opaque photo-mask is projected onto the resist film by a light exposure and a consequent development. During exposure, the mask has to contact against the resist to avoid the maleficent diffraction. In chapter 5, we adopt this technique to produce long period gratings along fiber tapers.

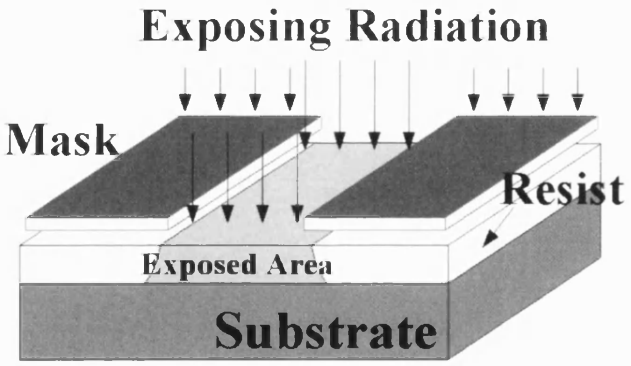

Fig. 3.4. Schematic of contact optical lithography.

3.3.2 Thermal evaporation deposition

Thermal evaporation deposition technique consists of heating a crucible until evaporation of the material to be deposited and condensing material vapour on the substrate surface in form of a thin film. Simultaneously, a quartz crystal thickness monitor is mounted inside the deposition chamber shown in Fig. 3.5 and real-time indicates the deposition thickness. In chapters 4 and 5, we use this technique to deposit metal Au and NiCr.

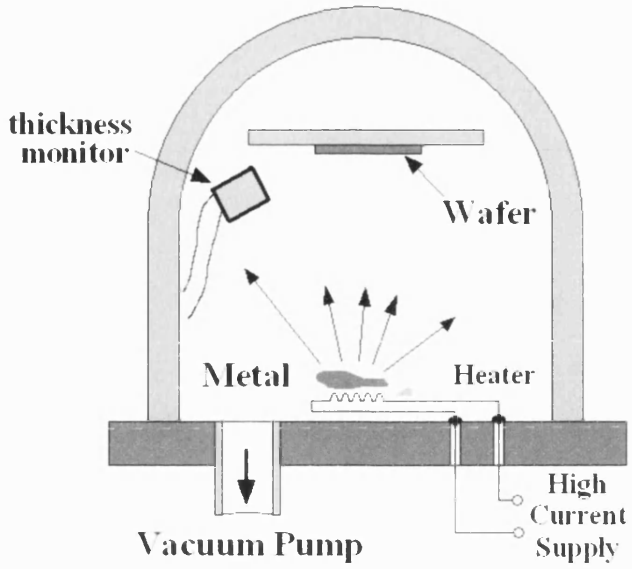

Fig. 3.5. Thermal evaporation system.

3.3.3 Etching (wet etching and dry etching)

Wet etching is usually a chemical process where material is removed from a substrate with the sample immersed in an etch solution. During wet etching, a mask layer protects a specific area of the wafer surface in order to etch a pattern. The drawback of wet etching is its isotropic nature that results in an undercut as shown in Fig. 3.6b. This undercut limits the minimum feature size of wet etching.

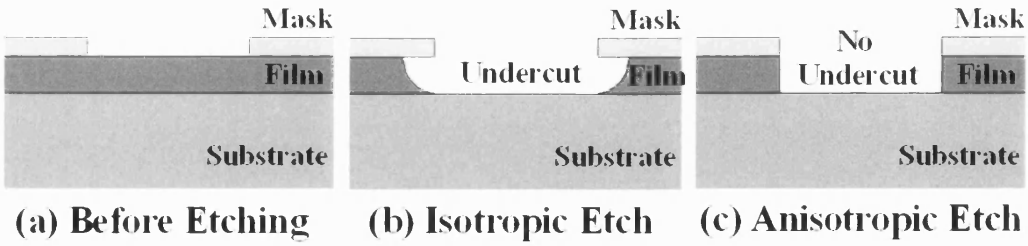

Fig. 3.6. Schematic of the isotropic and anisotropic etch processes.

Hydrofluoric (HF) acid is the most widely used etch solution for silica. A well-controlled solution can be obtained by buffering this acid with ammonium fluoride. In chapter 5, HF etching is used to produce long period gratings along fiber tapers. The typical etch rate in our experiments is around 0.1 μm/min.

Another frequently used chemical solution is the mixture of acetic acid, CH_3COOH, cerium ammonium nitrate, $(NH_4)_2Ce(NO_3)_6$, and water. This solution can

dissolve chromium and chromium alloy and is used in chapter 4. Its composition is: 35 ml acetic acid, 200 g ceric ammonium nitrate, and 1000 ml de-ionised water.

In order to overcome the shortcoming of the isotropic etching, dry etching is introduced. The first example is reactive ion etching (RIE), which refers to an ion-assisted chemical-physical combined etching process: the chemical etching takes place when the material to be etched reacts with the etchant species, which are free radicals generated in the plasma, to form volatile compounds; the physical etching occurs by bombardment sputtering with ions accelerated by the voltage difference between the plasma and the powered electrode. Benefiting from these two etching mechanisms, RIE can create selective and anisotropic etch features as shown in Fig. 3.6c.

In our work presented in chapter 4, we use a RIE/ICP system to create sub-micron scale grooves on fiber tapers. This system has an inductively coupled plasma (ICP) source, which produce much higher plasma densities and therefore a higher etching rate compared to those systems without ICP. Furthermore, RIE/ICP etching offers an independent control to plasma density and energy. Fig. 3.7 schematically shows this system.

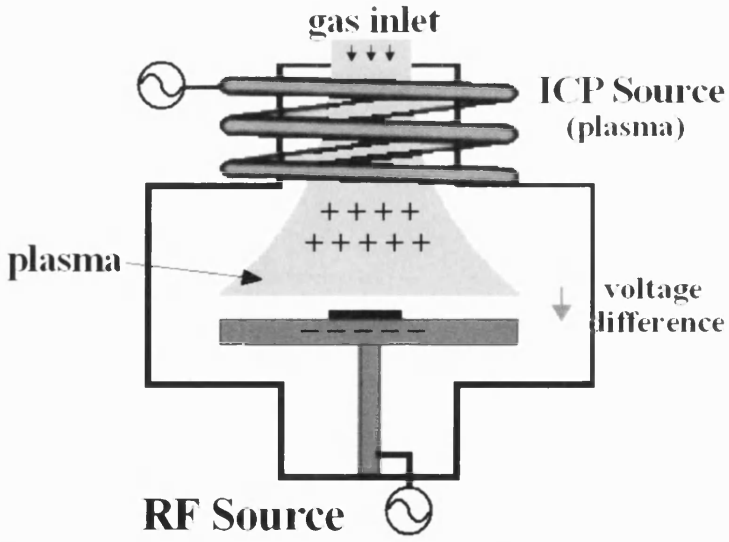

Fig. 3.7. Reactive ion etching process with an inductively coupled plasma source.

The second dry etching technique is known as focused-ion-beam (FIB) etching. A focused Ga^+ beam generated from a liquid metal ion sources (LMIS) [Prewett 91] is raster scanned over the surface of a sample. Energetic beams enable nano-patterning

by bombarding ion towards samples. In some cases, the energetic ion beam will be neutralized before bombardment by an electron beam, so that the defocusing effect caused by charging is minimized. Simultaneously with the ion milling, secondary electrons (or ions) are collected to form a micro image. Fig. 3.8 schematically shows the FIB system. In chapter 5, we use FIB milling to produce deep structures on thin fiber tapers. The features can be several microns deep, and the typical milling rate is around 1 μm^3/min.

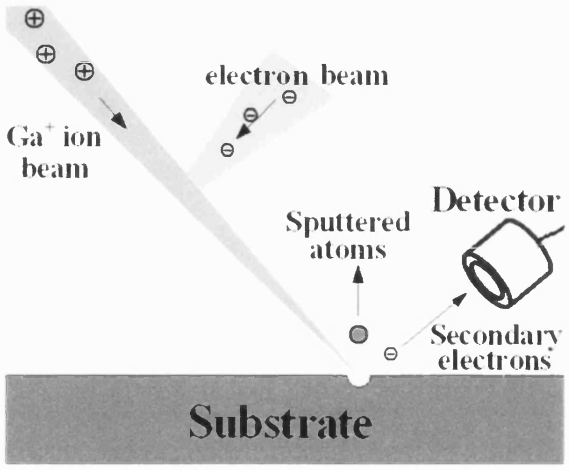

Fig. 3.8. Schematic of focused ion beam process.

3.4 Interference lithography technique

In an interference lithography configuration shown in Fig. 3.9, two or more coherent plane wave beams produce a periodic intensity pattern in the overlapping area. This pattern is then imprinted onto the resist layer, which has been previously applied on the substrate surface. During the exposure, the spatial coherence between the beams has to be maintained; the phase drifts between them must be compensated dynamically. These constitute the interference lithography technique.

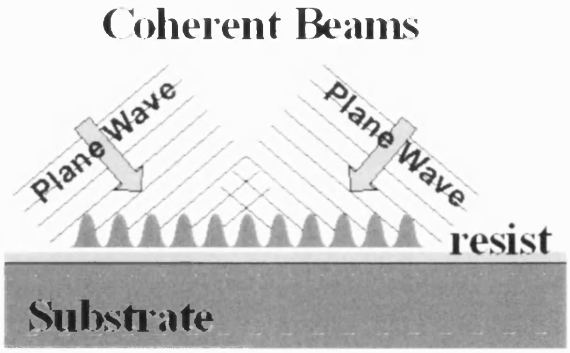

Fig. 3.9. Schematic of the interference exposure.

3.4.1 Interference exposure system

An interference exposure system, which allows us to produce not only one-dimensional Bragg gratings but also two-dimensional periodic patterns, has been built.

A krypton ion laser (Coherent INNOVA 300C) is used as the exposure source. The laser operates in single-line model and provides linearly polarized cw light with a wavelength of 406.7 nm and maximum output power of more than 100 mW. The laser wavelength falls within the sensitivity region of most commercial photo resists, and the time coherence of the single-line laser beam is good enough for the interference exposure.

A vertical layout, as shown in Fig. 3.10, is adopted in our experiments. The sample to be exposed is mounted upside down, and the exposure beams point upward and are symmetrically arranged around the line perpendicular to the wafer. The merit of this vertical configuration is that the system is easy to be extended to multi-beam exposures.

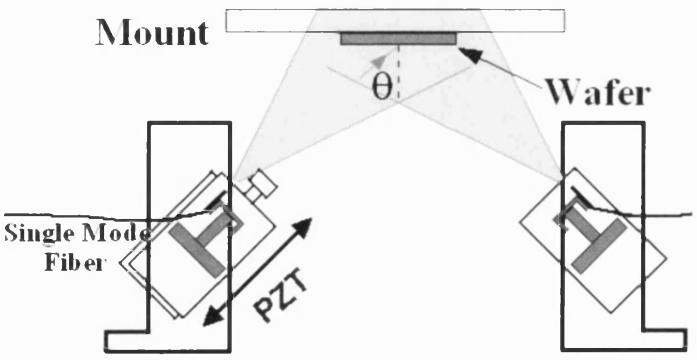

Fig. 3.10. Schematic of the vertical interference exposure configuration.

The light from the laser is first split into several beams and then coupled into endlessly single-mode photonic crystal fibers (ES-PCF, Fig. 3.11a). The pure silica composition of the photonic crystal fibers prohibits the harmful darkening effect occurring in germanosilicate core fibers [Dong 95]. The wanted plane wave front of the exposure beam (Fig. 3.9) is approximately simulated by the far-field illumination of the single mode fiber (see Fig. 3.11b). Therefore, the plane wave condition is only satisfied in a limited exposure area with a diameter of ~5 mm. Across this area, the grating period, Λ, keeps constant and is determined by the exposure wavelength, λ_0, and the half angle of incidence, θ. (see definition in Fig. 3.10)

$$\Lambda = \frac{\lambda_0}{2\sin\theta} \qquad \text{(two - beam exposure)} \qquad (3.1)$$

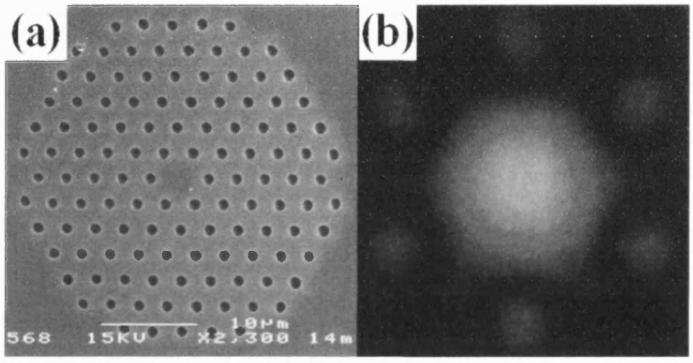

Fig. 3.11. (a). Scanning electron micrograph of endlessly single mode photonic crystal fiber. (b). Photograph of the far field of the single mode fiber.

During interference exposures, the phase differences between exposure beams have to be locked to prevent any drift of fringes. This phase-shift locking function is implemented by a feedback loop system, which consists of one 50:50 beam splitter, two photo detectors, one set of electronic circuit, and one piezoelectric translator (PZT).

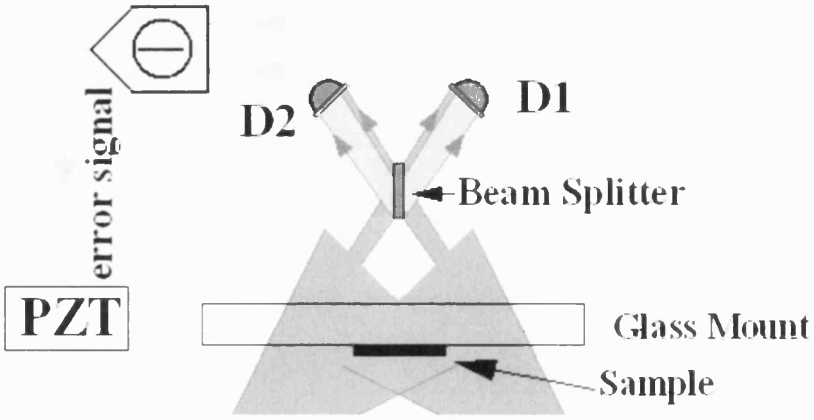

Fig. 3.12. Schematic of the phase-shift locking system. D1, D2, photo detectors; PZT, piezoelectric translator.

As shown in Fig. 3.12, a beam splitter sheet is mounted behind the sample. Two exposure beams are respectively transmitted and reflected through this beam splitter, and produce interference patterns on photo detectors D1 and D2. These two patterns on D1 and D2 have inverse fringes, whose difference provides a feedback error signal. Any phase shift between these two exposure beams is thus compensated by moving one fiber end forward or backward using a piezoelectric translator. The mounting of the PZT and the fiber end has been shown in Fig. 3.10.

The beam splitter sheet and the detectors D1 and D2 are all mechanically fixed on a big exposure stage, where both the glass mount and the sample are also attached on. The stabilization amongst these items is found to be good, since the interference fringe created by this exposure system has a good quality.

For each illumination fiber, in order to control the polarization state and the output power, one rotatable fiber coil polarization controller [Lefevre 80] and one fiber bending unit are used as shown in Fig. 3.13. For endlessly single-mode PCF, transmission loss has a substantial susceptibility to fiber bending [Birks 97], so that the fiber bending unit can provide a broad tuning range for the beam output power.

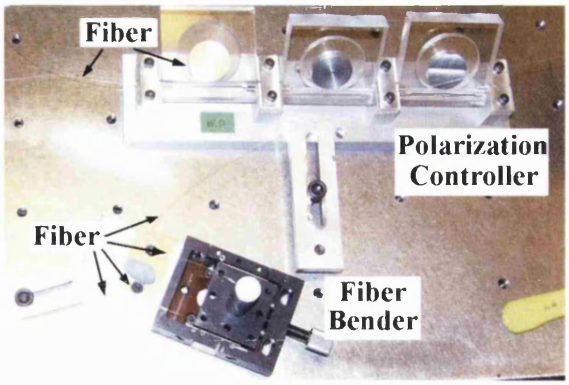

Fig. 3.13. Photograph of the rotatable fiber coil polarization controller and the fiber bending device.

Fig. 3.14 shows a photograph of the exposure stage. The system in this picture has been adjusted for two-beam interference exposure.

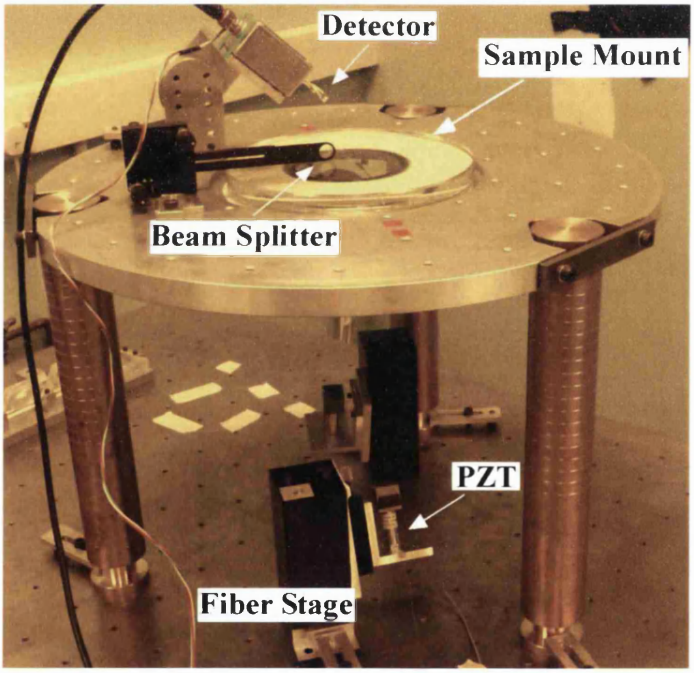

Fig. 3.14. Photograph of the interference exposure stage.

3.4.2 Demonstration of three-beam interference lithography

The above interference exposure system can be easily extended to three-beam exposure cases. To do so, one more fiber stage, as shown in Fig. 3.10, and one more phase-shift locking system, as shown in Fig. 3.12, are needed. Three exposure fiber stages are arranged around the sample with an identical incidence angle θ (see Fig.

3.10). Two phase-shift locking systems are used to compensate the drifts of the phase differences between these beams. (one phase-locking system for two beams)

By setting the polarizations of the exposure beams to be parallel to wafer and arranging these three beams 120° apart, an approximately equilateral triangle pattern was formed in a photoresist layer on a silicon-on-insulator (SOI) wafer. The resist was previously spin coated on the wafer and had a thickness of ~250 nm after soft baking. Fig. 3.15 shows a SEM image and photograph. The pitch, Λ, is determined by the exposure wavelength, λ_0, and the incidence angle, θ.

$$\Lambda = \frac{2\lambda_0}{3\sin\theta} \qquad \text{(three - beam exposure)} \qquad (3.2)$$

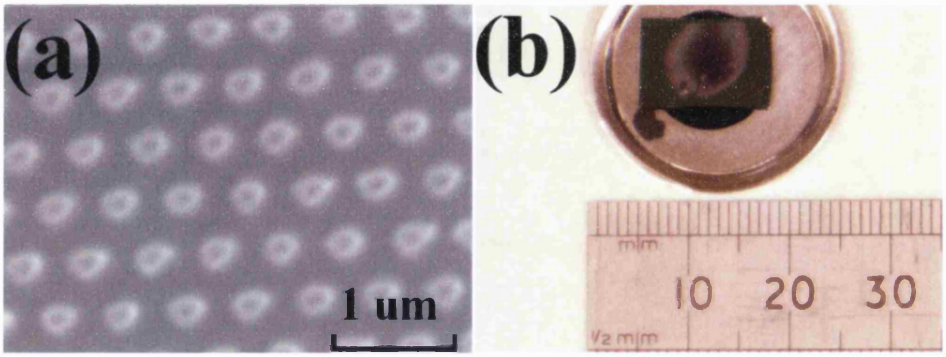

Fig. 3.15. (a) Scanning electron micrograph and (b) photograph of a hexagonal pattern in a photoresist layer produced by three-beam interference lithography.

The advantage of our multi-beam interference lithography technique over the pixel scanning electron beam lithography and the multi-dimensional interference lithography [Zengerle 87] is its time and cost efficiency. The triangle pattern shown in Fig. 3.15 was produced in a ~3 minute-long exposure with each beam of 350 μW and the distance from fiber end to wafer of 15 cm. The SEM imaging indicated that the lattice pitch was uniform over an area of ~25 mm^2 with a variation of less than 2%. However, the drawback of this technique is the poor control to unit size and detailed features.

If this two-dimensional periodic pattern is transferred into the substrate SOI wafer, we can produce a photonic crystal planar waveguide, whose guided mode properties and dispersive behaviours are of importance for understanding photonic crystals [Zengerle 87].

Chapter 4

Surface Bragg Gratings on Fiber Tapers

4.1 Introduction

With the extensive use of optical fibers in telecommunication systems, in-line fiber devices are receiving more attention than free-space optical devices due to their intrinsic compatibility with fiber links. One such example is the fiber taper in a directional fiber coupler [Mortimore 85]. With decreasing taper diameter, the evanescent field tail of the guided mode spreads out across the silica surface, which can be exploited in applications such as evanescent coupling [Barclay 04] and optical sensing [Ding 05].

In order to enrich the functionality of fiber tapers, introducing longitudinal Bragg gratings is a straightforward method. However, due to the disappearance of the germanium core and the evanescent mode field, the conventional UV-writing technique is unsuitable for a micron-scale fiber taper [Hernandez 04]. In this chapter, two surface Bragg grating structures written on micron-scale fiber tapers [Ding 06] are presented. We describe the fabrication, investigate the optical spectral properties theoretically and experimentally, and discuss potential applications of these devices.

4.2 Fiber tapers decorated with Au surface Bragg gratings

A gold Bragg grating has been created on the surface of a micron-scale fiber taper [Ding 06]. The selection of gold as the grating material is due to the large permittivity contrast between gold and environment. This dramatically enhances the mode coupling induced by the surface grating, which would otherwise be very weak due to the low field overlap. This section presents the fabrication, theoretical treatment, spectral measurements, and potential applications of this device.

4.2.1 Device description

A fiber taper with a uniform waist was produced by heating and stretching a piece of conventional single-mode fiber (Corning SMF-28 fiber with single-mode cutoff wavelength of less than 1260 nm). The diameter of the taper waist was ~10 μm, the lengths of the waist and the transitions were 20 and 25 mm respectively, and the excess loss resulted from the fiber tapering process was less than 0.1 dB at a wavelength of 1.55 μm. This fiber taper was mounted on a microscope slide (Fig. 4.1) and stored in a sealed container prior to further processing for the sake of cleanliness.

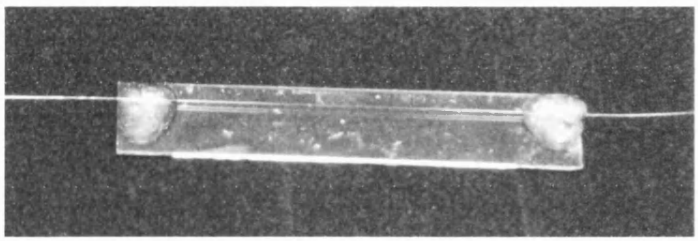

Fig. 4.1. Fiber taper mounted on a piece of glass slide with glue on both ends.

In order to produce a gold Bragg grating on this fiber taper, several planar processing steps as shown in Fig. 4.2 were carried out.

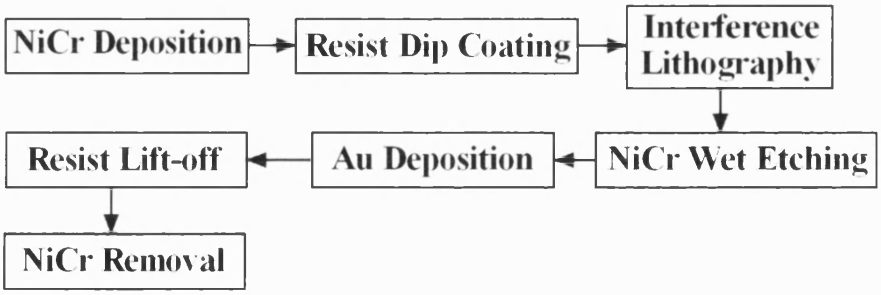

Fig. 4.2. Flow chart of the fabrication process of the Au grating fiber taper.

Firstly, a 20 nm thick NiCr (Ni80/Cr20 alloy) layer was deposited on the top side of the taper by thermal evaporation. The taper was then dip-coated with undiluted Shipley resist S1813. After two dip coatings and soft baking, the resist thickness was ~250 nm, which was estimated accordingly to the consequent lithographic condition.

The resist thickness is related to the resist viscosity, the withdrawal rate of dip coating, and the taper diameter. As shown in Fig. 4.3, the liquid pressure, P_{st}, inside the resist layer is determined by the surface tension coefficient, γ, and the taper

diameter, D, in form of Eqn. (4.1). The bigger the taper diameter, the lower is the liquid pressure, and the thicker is the resist film.

$$P_{st} = \frac{2\gamma}{D} \tag{4.1}$$

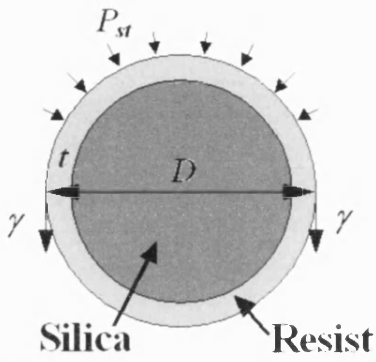

Fig. 4.3. Schematic of the liquid pressure inside the resist layer.

Then a Bragg grating was produced by interference exposure and development. The exposure system described in section 3.4 was used. Two beams, each with output power of 350 μW, made exposure for ~4 minutes. The exposed taper was located ~25 cm from the end of the illumination fibers (see Figs. 3.10 and 3.11), and the incident angle θ was ~23.5°. In this step, the previously deposited NiCr layer prevented multiple reflections of the exposure beams inside the taper, which would otherwise degrade the fringe quality. Then, the sample was developed in a diluted Microposit 351 solution (1 part Microposit 351 : 6 parts DI water) for 20 seconds.

After development, a solution of cerium ammonium nitrate and acetic acid, whose composition has been described in chapter 3, was used to etch away the NiCr layer through the resist mask. After wet etching for ~30 seconds, the silica surface beneath the NiCr layer was exposed in the area between resist strips, and a small undercut in the NiCr layer appeared, as shown in Fig. 4.4.

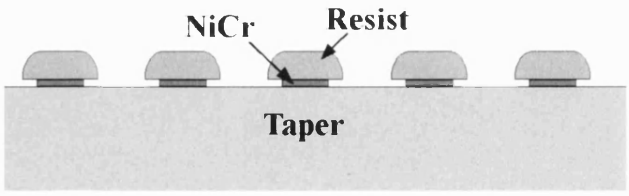

Fig. 4.4. Schematic of the resist and NiCr layers after wet etching.

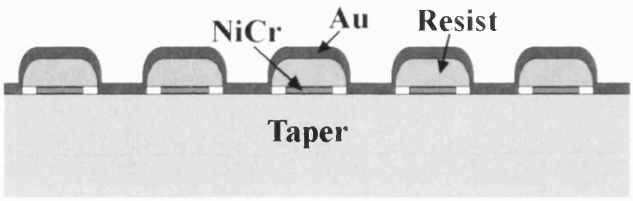

Fig. 4.5. Schematic of sample after Au deposition.

Subsequently, a 3 nm NiCr, followed by 50 nm of Au, was deposited as shown in Fig. 4.5. Here, the thin NiCr layer enhanced the adhesion between the Au layer and the silica substrate. The small undercut created in the previous step helped to produce a clean edge in the following lift-off process, in which step the sample was rinsed by acetone and its surface is gently wiped with a clean Q-tip.

In the last step, the residual NiCr in the gaps between the gold strips was removed using the solution of cerium ammonium nitrate and acetic acid. A periodic gold grating on the taper surface was then left.

Fig. 4.6 shows scanning electron micrographs of three taper samples a, b and c. The taper diameters are ~10 μm, the grating lengths are ~5 mm, and the Au thicknesses are 10, 20 and 50 nm respectively.

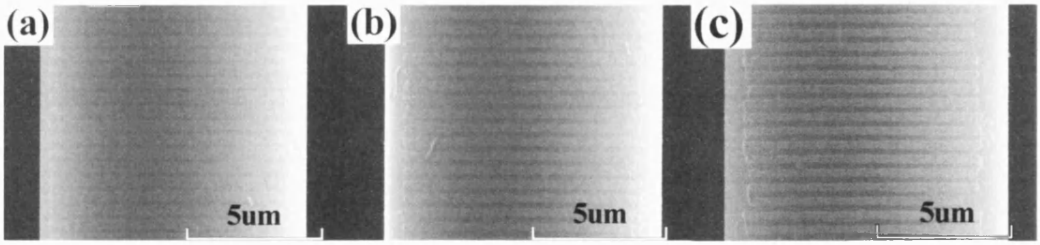

Fig. 4.6. Scanning electron micrographs of sample a, b, and c. The Au thicknesses were 10, 20, and 50 nm respectively. A 3 nm NiCr was laid beneath the Au layer.

Table 4.1 list the measured parameters of each sample, which have been calibrated by a precise SEM test specimen.

Parameters	Sample (a)	Sample (b)	Sample (c)
Au Thickness (nm)	10	20	50
Diameter (μm)	9.6	10.0	10.2
Period (nm)	510.0	508.6	505.9

Table 4.1. Measured parameters of Au grating fiber tapers.

4.2.2 Theoretical treatment

Due to the loss of cylindrical symmetry in gold strips, the mode coupling induced by the surface grating is not limited by the azimuthal order of the modes of the fiber tapers. The input fundamental mode, which is converted from the core mode of the un-tapered fiber through the adiabatic transition [Love 86], excites different backward modes at different wavelength via the Bragg grating. The following phase matching condition determines which mode is excited at a given wavelength [Hill 97].

$$\frac{2\pi}{\Lambda} = \beta_0(\lambda, D) + \beta_i(\lambda, D) \tag{4.2}$$

Here, Λ is the grating period, λ is the wavelength, D is the taper diameter, and β_i is the propagation constant of the i^{th} order mode.

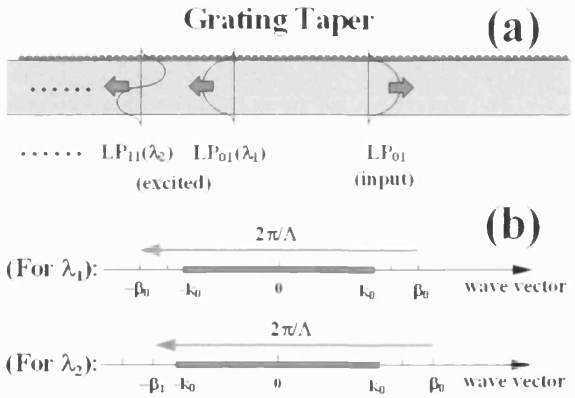

Fig. 4.7. Sketches of the surface grating taper in (a) real and (b) reciprocal spaces.

Fig. 4.7 schematically shows the mode coupling in real and reciprocal space [Russell 85]. With a fixed grating wave vector, $2\pi/\Lambda$, different backward modes are excited at different wavelengths. For example, in Fig. 4.7b, a backward fundamental mode with propagation constant of $-\beta_0(\lambda_1)$ is excited at the wavelength of λ_1; while a backward high-order mode with propagation constant of $-\beta_1(\lambda_2)$ is excited at a shorter wavelength of λ_2. Here, the fundamental and high-order modes are respectively the LP_{01} and LP_{11} modes (Linear Polarized modes) as shown in Fig. 4.7a. As the wavelength further decreases, the arrow of the grating wave vector will fall in the continuous region from $-k_0$ to k_0 (see Fig. 4.7b). That means the excited wave will leave the fiber taper as radiation.

On the other hand, the strength of the mode coupling can be quantified by the coupling coefficient κ [Erdogan 97]:

$$\kappa = -\frac{i\omega c\mu}{4}\int_{A_\infty} \Delta\varepsilon(x,y)[\hat{\mathbf{e}}_f(x,y)\times\hat{\mathbf{h}}_b^{\,*}(x,y)]\cdot\hat{\mathbf{a}}_z dA \tag{4.3a}$$

where the subscripts f and b denote the forward and backward modes, $\hat{\mathbf{a}}_z$ is the unit vector along the taper axis, $\Delta\varepsilon$ is the permittivity perturbation caused by the grating, and the caret symbol denotes the field normalization as follows.

$$\frac{1}{2}\int_{A_\infty} [\hat{\mathbf{e}}_f(x,y)\times\hat{\mathbf{h}}_f^{\,*}(x,y)]\cdot\hat{\mathbf{a}}_z dA = -\frac{1}{2}\int_{A_\infty} [\hat{\mathbf{e}}_b(x,y)\times\hat{\mathbf{h}}_b^{\,*}(x,y)]\cdot\hat{\mathbf{a}}_z dA = 1 \tag{4.3b}$$

Eqns. (4.3a) and (4.3b) can be deduced from Eqn. (2.35).

In order to obtain a large coupling coefficient, a big field overlap with the grating structure is preferred. Therefore, the conventional UV technique writes Bragg gratings in the core region of fibers. However, in our 10 μm-diameter fiber tapers, the field overlap with surface structures is small. For achieving a strong mode coupling, we need a large permittivity contrast, which can be satisfied by using gold as the grating material. The large permittivity contrast between the grating material and environment relax the requirement to taper diameter. Otherwise, a much thinner taper, which will bring severe fabrication problems, is needed.

For modelling purposes, the complex dielectric constant of gold can be expressed in the Lorentz-Drude model [Rakic 98]:

$$\varepsilon(\omega) = 1 + \frac{f_0\omega_p^{\,2}}{-\omega^2 - i\omega\Gamma_0} + \sum_{j=1}^{k}\frac{f_j\omega_p^{\,2}}{\omega_j^{\,2} - \omega^2 - i\omega\Gamma_j} \tag{4.4}$$

where ω_p is the plasma frequency; the frequency ω_j, strength f_j, and lift time $1/\Gamma_j$ represents the j^{th} oscillator in this model. The second term refers to the intraband free-electron behaviour, and the third term accounts for interband effects. For gold, the following parameters are adopted [Rakic 98]:

$$\omega_p = 1.37188\times10^{16}, \begin{cases} f_0 = 0.76, \omega_0 = 0, \Gamma_0 = 8.05202\times10^{13} \\ f_1 = 0.024, \omega_1 = 6.30488\times10^{14}, \Gamma_1 = 3.66139\times10^{14} \\ f_2 = 0.01, \omega_2 = 1.26098\times10^{15}, \Gamma_2 = 5.24141\times10^{14} \\ f_3 = 0.071, \omega_3 = 4.51065\times10^{15}, \Gamma_3 = 1.32175\times10^{15} \\ f_4 = 0.601, \omega_4 = 6.53885\times10^{15}, \Gamma_4 = 3.78901\times10^{15} \\ f_5 = 4.384, \omega_5 = 2.02364\times10^{16}, \Gamma_5 = 3.36362\times10^{15} \end{cases} \tag{4.5}$$

Here, the units of ω and Γ are radians per second. Fig. 4.8 shows the real and imaginary parts of the dielectric constant of gold in the near-infrared wavelength region. The real part of the dielectric constant of gold is significantly different from

that of air, while the imaginary part, which corresponds to the absorption coefficient, is close to 0.

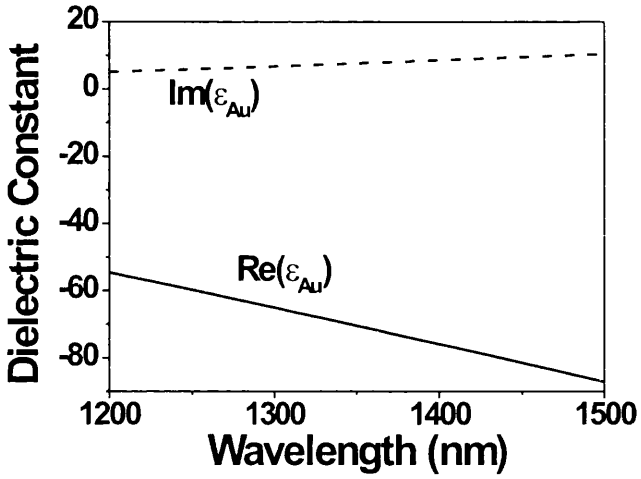

Fig. 4.8. Dielectric constant of gold in the near-infrared wavelength region.

If the surrounding medium is changed and has a refractive index of n_{ext}, the previously used resonant condition, Eqn. (4.2), must change to be:

$$\frac{2\pi}{\Lambda} = \beta_0(\lambda, D, n_{ext}) + \beta_i(\lambda, D, n_{ext}) \tag{4.6}$$

And the resonant condition of the radiation mode coupling also becomes,

$$\frac{2\pi}{\Lambda} \leq \beta_0(\lambda, D, n_{ext}) + n_{ext} \cdot k_0 \tag{4.7}$$

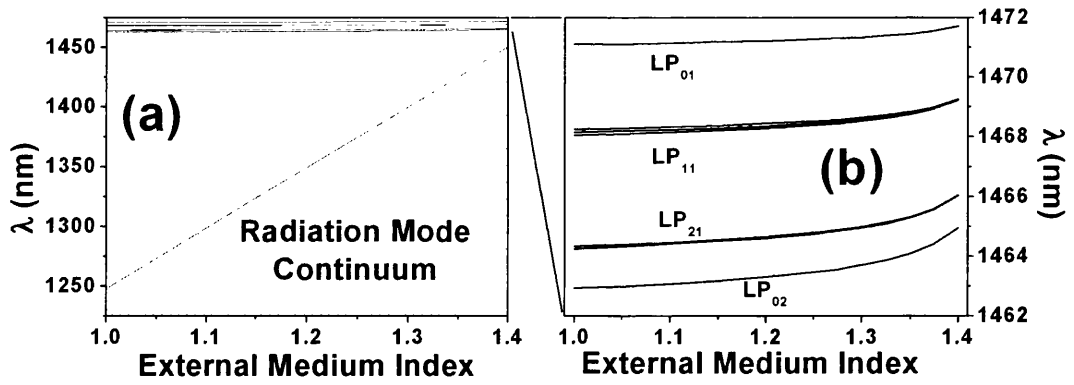

Fig. 4.9. (a) Calculated resonant wavelengths as a function of the external medium index. (b) Magnified view of top part of Fig. (a).

Fig. 4.9 shows the variation of the resonant wavelength with the external medium index. The parameters used in the calculations are: D = 10.4 μm and Λ = 510.4 nm. For each excited guided mode, the sensitivity of the resonant wavelength to the external medium index increases as the mode approaches the cut-off, at which the mode field largely penetrates into the environment. With the same reason, to a higher order mode excitation, the resonant wavelength presents a higher sensitivity to n_{ext}.

For the radiation mode excitation, the edge of the coupling continuum region, λ_R, has an approximately linear variation with the external medium index as shown in Fig. 4.9. The slope $d\lambda_R / dn_{ext}$ is nearly constant over a large range. This characteristic is favourable for sensing applications. However, the question is if we can discern this edge.

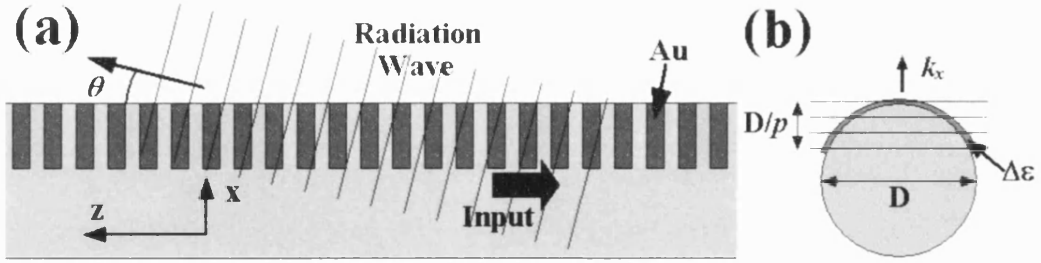

Fig. 4.10. Sketches of the radiation mode coupling in (a) longitudinal and (b) cross-sectional views.

Fig. 4.10 shows sketches of a Au grating taper, where the radiation mode is assumed to be a plane wave with transverse and longitudinal wave vector components of k_x and k_z. Substituting this plane wave into the coupling coefficient Eqn. (4.3a), a requirement to k_x can be derived:

$$|k_x| \leq p\pi / D \tag{4.8}$$

where D/p denotes the effective height of the Au strips as shown in Fig. 4.10b. If k_x is out of this range described in Eqn. (4.8), the integral in Eqn. (4.3a) will average out due to the transverse oscillatory field distribution of the plane wave across the half-ring shaped Au strips, and the strength of the radiation coupling will decrease.

According to Eqn. (4.8), a bigger taper diameter results in a more stringent limit on k_x and therefore a more discernable edge of the radiation-coupling continuum.

From Eqn. (4.8) and using $k_z = \sqrt{(n_{ext}k_0)^2 - k_x^2}$, the limiting relation for k_z can be obtained as

$$n_{ext}k_0 - \frac{p^2\pi^2}{2n_{ext}k_0D^2} \le k_z \le n_{ext}k_0 . \tag{4.9}$$

Substituting Eqn. (4.9) into the resonant condition, the edge of the radiation-coupling continuum falls in the following region:

$$\lambda_R(1 - \frac{p^2\Lambda\lambda_R}{8D^2n_{ext}}) \le \lambda \le \lambda_R \tag{4.10}$$

where λ_R was obtained from Eqn. (4.7). Fig. 4.11 shows the calculated radiation coupling edge for D = 10.4 μm, Λ = 510.4 nm, and p = 3.5.

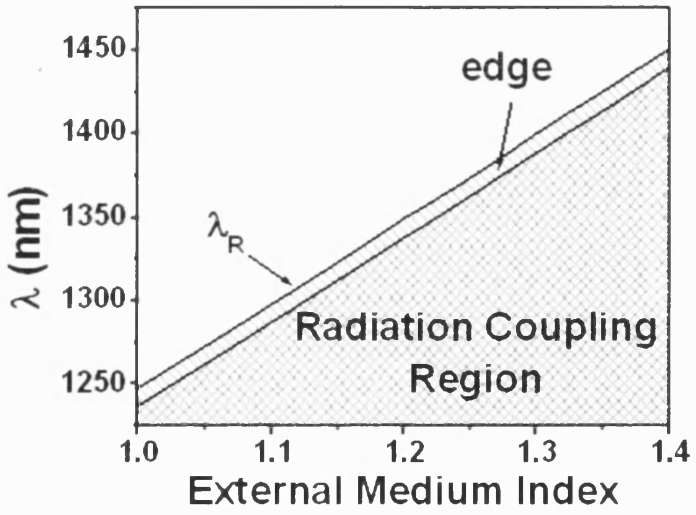

Fig. 4.11. Edge of the radiation-mode-coupling continuum.

4.2.3 Spectral measurements and analysis

Optical characterization was carried out using the experimental setup shown in Fig. 4.12, which comprises an ultrabroadband supercontinuum source based on an endlessly single mode photonic crystal fiber (ES-PCF) [Wadsworth 04], a fiber optic circulator and two optical spectrum analyzers (OSAs). For convenience, the endlessly single mode PCF and the input fiber of the circulator were cleaved and butt-coupled.

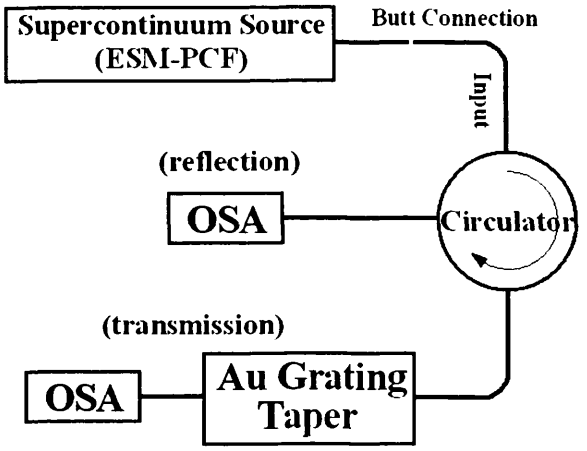

Fig. 4.12. Experimental setup for spectral measurements.

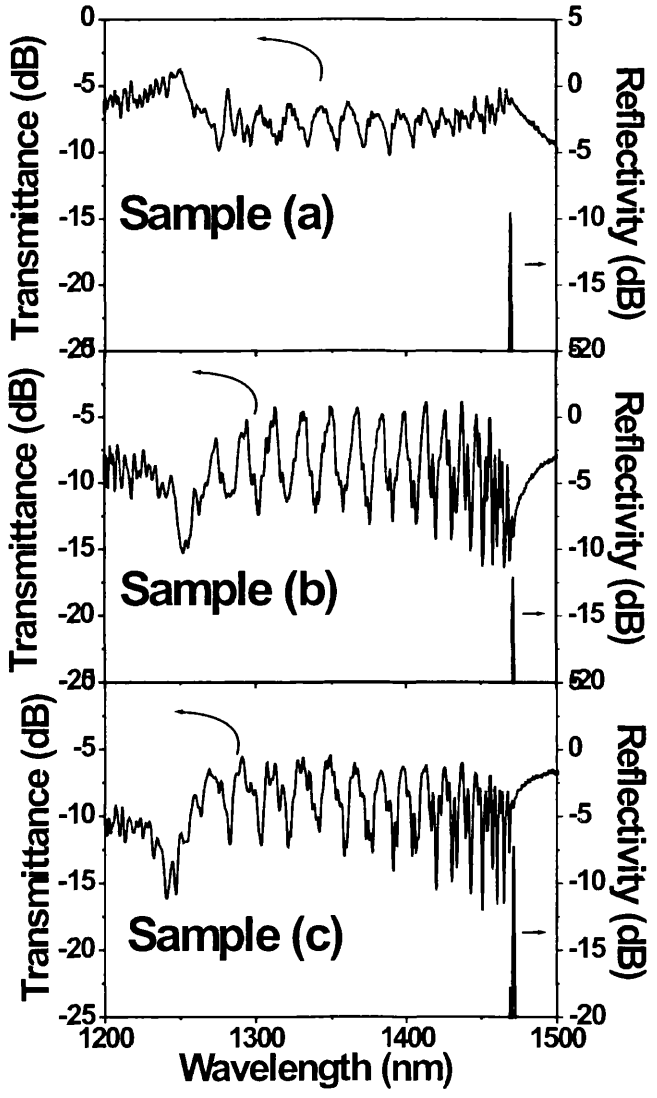

Fig. 4.13. Transmittance (upper curves) and reflectivity (lower peaks) spectra of sample a, b, c. The measurement resolution was 1 nm.

Fig. 4.13 shows the transmittance and reflectivity spectra of the three grating taper samples (a, b, and c) with a measurement resolution of 1 nm. A number of transmission dips appear and indicate the coupling from the forward fundamental mode to various backward guided modes. Amongst these backward modes, only the fundamental mode is converted back into the core mode of the un-tapered single mode fiber through the adiabatic taper transition and is observed in the reflectivity spectrum; other backward modes are ultimately converted into cladding modes and are damped at the lossy interface between the polymer coating and silica fiber.

The deep transmission dips, shown in Fig. 4.13, indicate that the grating-induced mode coupling is very strong.

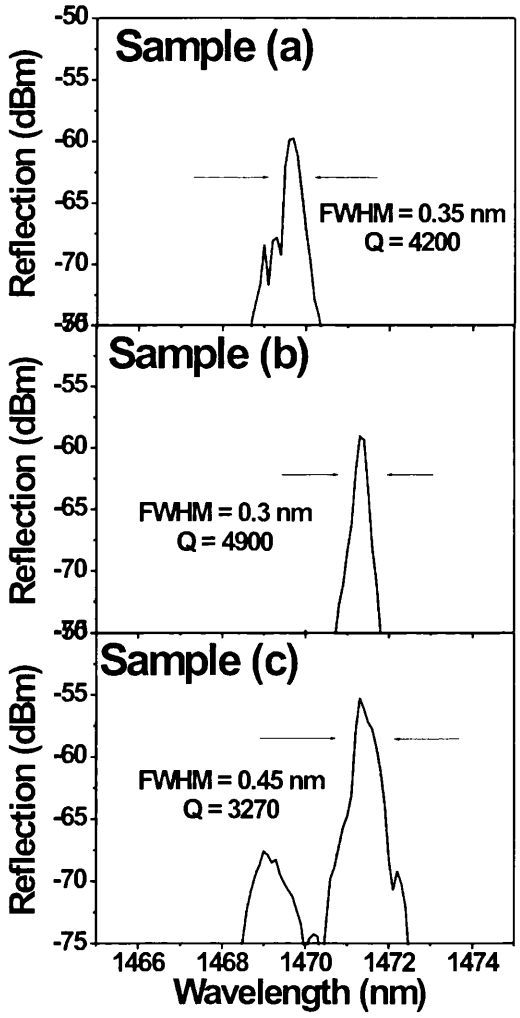

Fig. 4.14. Magnified views of the reflected spectra in Fig. 4.13 with a resolution of 0.1 nm.

Fig. 4.14 shows magnified reflected spectra with a high resolution of 0.1 nm. The full-width half-maximum (FWHM), $\Delta\lambda$, of sample b is ~0.3 nm, which is nearly consistent with the relation $N/2 \approx \lambda_R/\Delta\lambda \equiv Q$ [Erdogan 97]. Here, λ_R is the resonant wavelength, the period number N is obtained from the grating length, 5 mm, divided by the grating period ~500 nm, and the Q factors represent the finesse of the spectra.

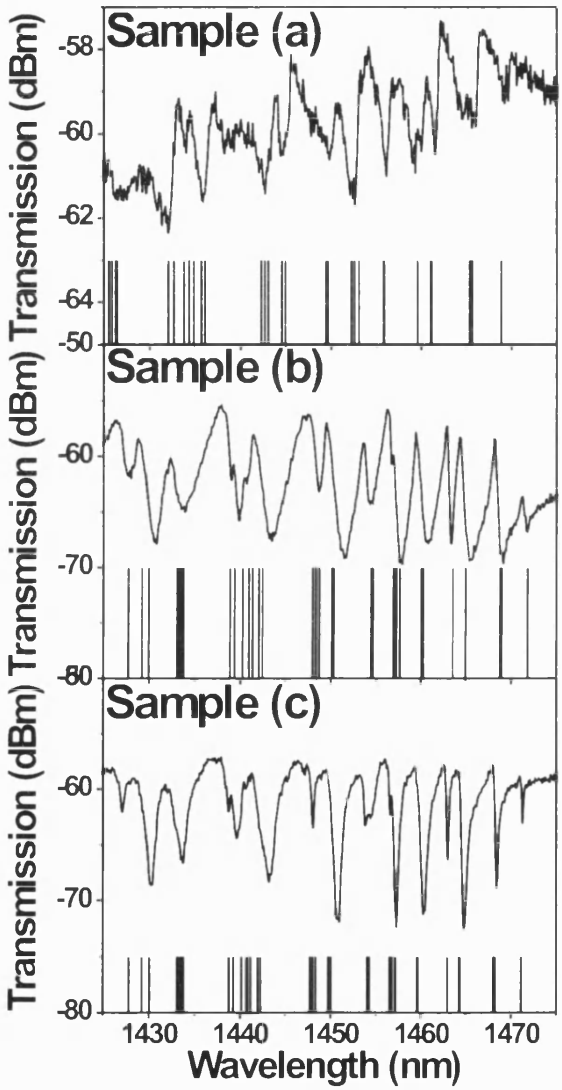

Fig. 4.15. Magnified transmitted spectra (upper curves) of samples with a resolution of 0.1 nm and calculated resonant wavelengths (vertical lines) of few mode couplings.

Fig. 4.15 shows the magnified transmitted spectra with a resolution of 0.1 nm. Each vertical line in the lower parts of the pictures labels the calculated resonant wavelength of mode-coupling between different pairs of modes using the method described in last subsection. In the calculation, the geometrical parameters of the

samples, i.e. the taper diameter and the grating period, are slightly altered from the measured ones, so as to obtain good fits between calculations and the measured results. Table 4.2 lists these parameters and their deviation from the measured values.

Parameters	Sample (a)	Sample (b)	Sample (c)
Diameter (μm)	9.7 (1.0%)	10.3 (3%)	10.4 (2%)
Period (nm)	509.8 (-0.04%)	510.7 (0.4%)	510.4 (0.9%)

Table 4.2. Parameters of Au grating fiber tapers used in calculations. The values in parentheses stand for the deviation of the values in Table 4.2 from those in Table 4.1.

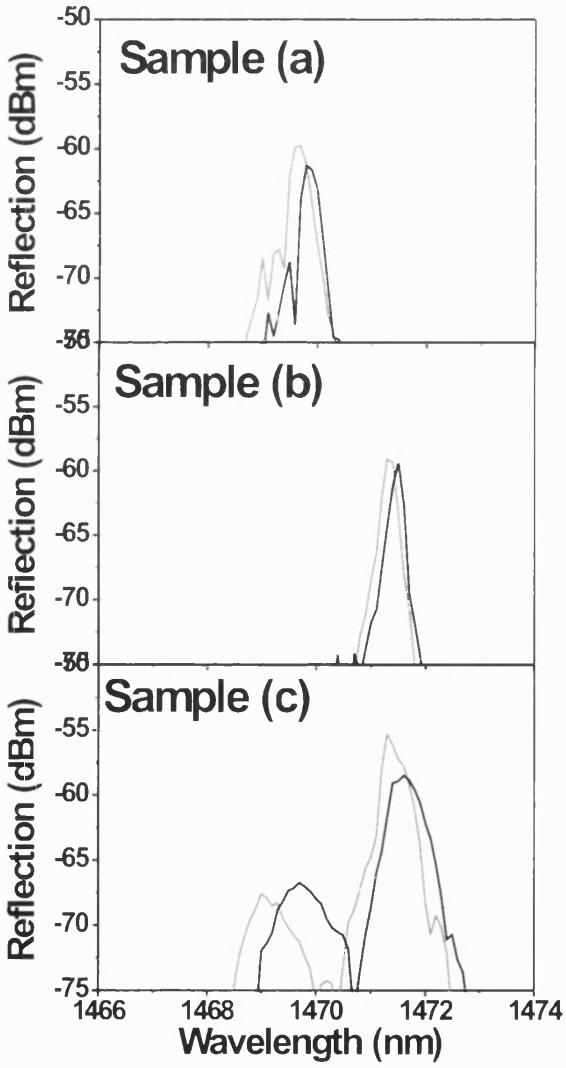

Fig. 4.16. Reflected spectra of the samples immersed in water (black) and air (gray). The measurement resolution is 0.1 nm.

Figs. 4.16 and 4.17 respectively show the reflection and transmission spectra when the samples are immersed in water. For comparisons, the gray curves in Fig. 4.16 show the reflected spectra of samples suspended in air. It indicates that the resonant wavelength of the fundamental mode coupling, which corresponds to the reflection peak, increases with increasing index of the external medium. In Fig. 4.17, the vertical lines are the calculated resonant wavelengths. All grating taper parameters used in the calculation are from Table 4.2, and the refractive index of water is taken as 1.33. The agreement between calculated and measured results is good.

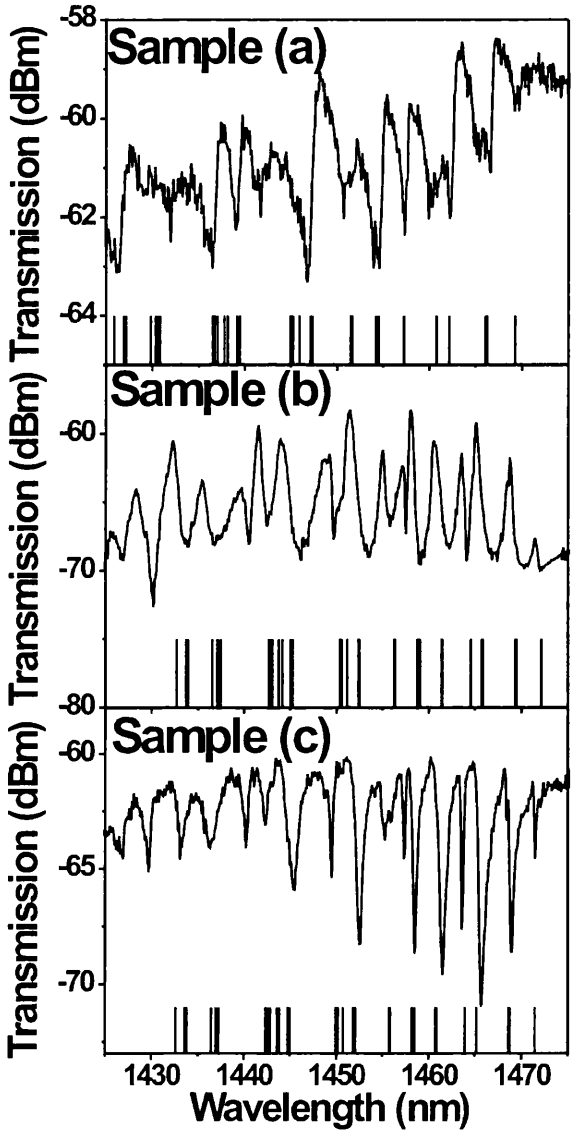

Fig. 4.17. Transmitted spectra of the samples immersed in water. The vertical bars are the calculated resonant wavelengths. The grating taper parameters are shown in Table 4.2.

Due to using a small wavelength range for plotting pictures, the spectra in Fig. 4.17 conceal one important feature, which is shown in Fig. 4.18. Comparison between the transmittance spectra of sample c immersed in air and water reveals a radiation-coupling induced transmission dip, which lies at the edge of the radiation-coupling continuum and is ~20 nm wide. In subsection 4.1.2, we have discussed this coupling, whose spectral position can be expressed by Eqn. (4.10).

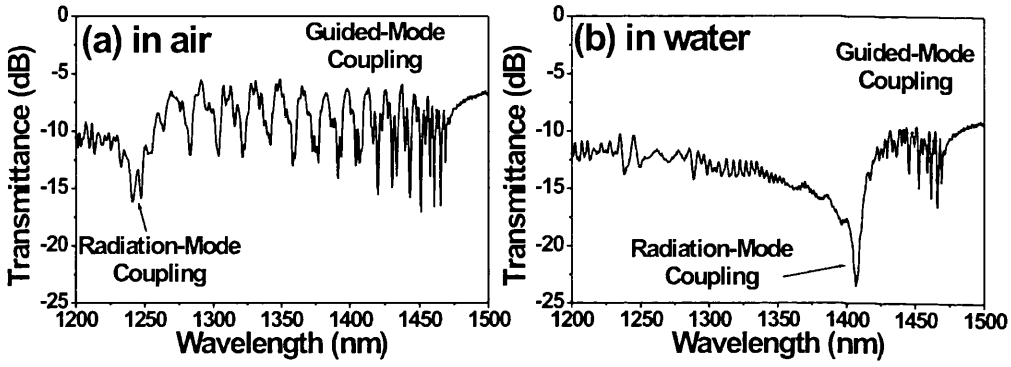

Fig. 4.18. Transmittance spectra of sample c immersed in (a) air and (b) water with a resolution of 1 nm.

In Fig. 4.18, the coupling occurring at the edge of the radiation continuum is found to be stronger than the guided mode couplings. It has a discernable spectral width and a high sensitivity to the surrounding medium, which suggests applications in the area of refractometric sensing. The oscillations appearing to the left of this dip are due to an etalon effect associated with the fiber butt coupling and can be removed by fusion splicing. And the water absorption induced transmission dip, which should be around 1390 nm, is much weaker than the grating coupling features.

Furthermore, the transmission spectra of sample c immersed in different Cargille optical liquids are also measured and shown in Fig. 4.19.

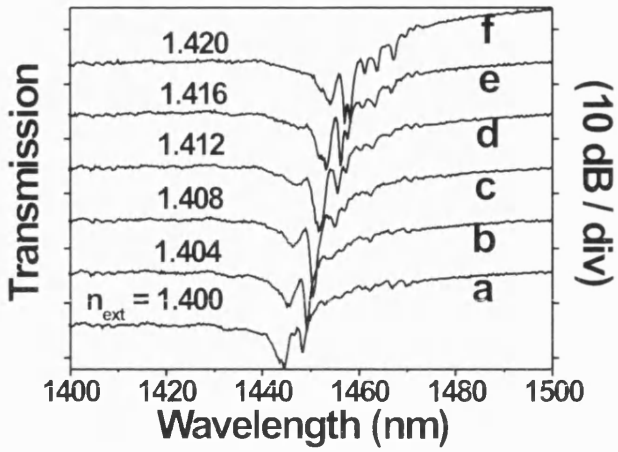

Fig. 4.19. Transmitted spectra of sample c immersed in different Cargille optical oils.

Cauchy dispersion equations [Jenkins 81] are used to provide the refractive index of the Cargille optical liquids at the experimental wavelengths. The external refractive index changes from 1.400 to 1.420 in going from curve (a) to (f), and the radiation coupling induced transmission dip moves towards longer wavelengths. Their resonant wavelengths are plotted in Fig. 4.20 as a function of the external refractive index (squares). The error bars represent the bandwidths of the transmission dips. The measured resonant wavelengths of the coupling to the LP_{01} and LP_{02} modes, which have the narrowest spectral feature in transmission spectra, are also shown in the top part of Fig. 4.20 using squares.

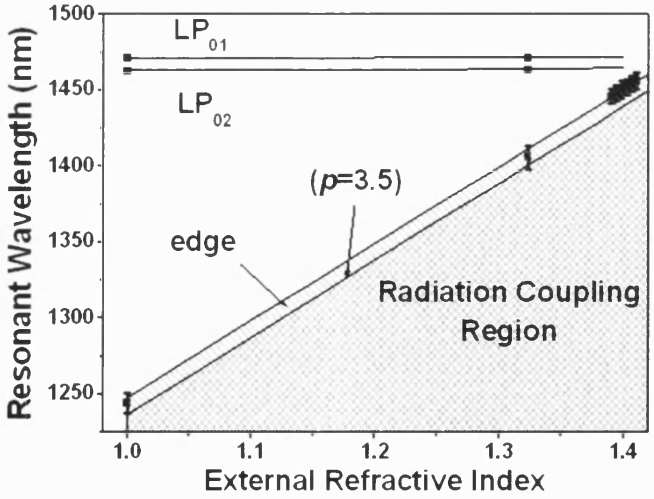

Fig. 4.20. Measured resonant wavelengths of sample c (squares) as a function of the external refractive index. The error bars represented the bandwidths. The solid lines were the calculated results.

In Fig. 4.20, all the measured resonant wavelengths fit well with the calculated results, which are shown by the solid curves and obtained from Eqns. (4.6), (4.7), and (4.10). In the calculation, the grating taper parameters in Table 4.2 are used. It is apparent that the coupling occurring at the edge of the radiation continuum has a higher sensitivity to the external refractive index than guided mode coupling. This is due to the fact that the radiation wave expands more widely into the external medium and brings more information about the external medium. In addition, this sensitivity is constant over a large range from n_{ext} = 1 to 1.41, whose upper limit is determined by the ability to discern the transmission dip. The resonant condition of the radiation coupling, Eqn. (4.7), can be approximately expressed as:

$$\lambda_R = [n_0(\lambda_R, D, n_{ext}) + n_{ext}]\Lambda \approx (n_{silica} + n_{ext})\Lambda, \tag{4.11}$$

so that,

$$d\lambda_R / dn_{ext} \approx \Lambda \tag{4.12}$$

Scheme	Sensitivity	Q Factor	Δn_{ext} (RIU*)
FBG	<100 (nm/RIU)	~10,000	5×10^{-3}
LPG	~2,000 (nm/RIU)	~50	1×10^{-2}
Tilted FBG	-	-	1×10^{-1}
SPR	~50,000 (nm/RIU)	~10	2×10^{-2}
Au Grating Taper	~500 (nm/RIU)	~50	4×10^{-1}

Table 4.3. Characteristics of various fiber refractometers.

* RIU, refractive index unit

Table 4.3 compares the characteristics of different fiber refractometer sensor devices, which include UV written fiber Bragg gratings (FBG) in side-polished schemes [Schroeder 01], fiber long period gratings (LPG) [James 03], tilted FBGs [Laffont 01], and surface plasmon resonance (SPR) fiber tapers [Diez 01]. For fiber Bragg grating and long period grating sensors, the high sensitivities are only obtained over a limited refractive index range where the excited backward (Bragg grating) or forward (long period grating) mode expands widely. For fiber Bragg grating sensors, in order to discern the narrow transmission dips, expensive spectrometric facilities are needed. That is another disadvantage for this device. The tilted FBG refractometers have oblique grating fringes in fiber cores and exploit radiation-mode coupling.

However, serious mixing with cladding mode coupling hampers their practical application [Erdogan 96]. As for SPR fiber taper sensors, which make use of surface plasmon resonance properties in metal-coated tapers, they only work in a narrow refractive index range, although with a very high sensitivity [Homola 99].

In Table 4.3, the sensitivity is defined as $d\lambda_R / dn_{ext}$, Q factor is $\lambda_R / \Delta\lambda$, and Δn_{ext} is the working range of the refractometric sensor. Here, λ_R denotes the resonant wavelength, and $\Delta\lambda$ is the typical spectral width.

Apart from the backward mode coupling discussed above, there is another consequence of the loss of cylindrical symmetry in our Au grating tapers. That is the introduction of polarization dependence. The setup used to study this characteristic is shown in Fig. 4.21. Supercontinuum light was first passed through a polarizing cube beamsplitter (extinction ratio 40 dB) and launched into a conventional single mode fiber. A rotatable fiber coil polarization controller was applied to this fiber and allowed adjustment of the polarization state. One fiber optic circulator and two optical spectrum analyzers (OSAs) were connected as shown in Fig. 4.12 and used to measure transmitted and reflected spectra. The polarizing cube beamsplitter was fixed during experiment, so that the coupling efficiency into the fiber end was constant during the measurement.

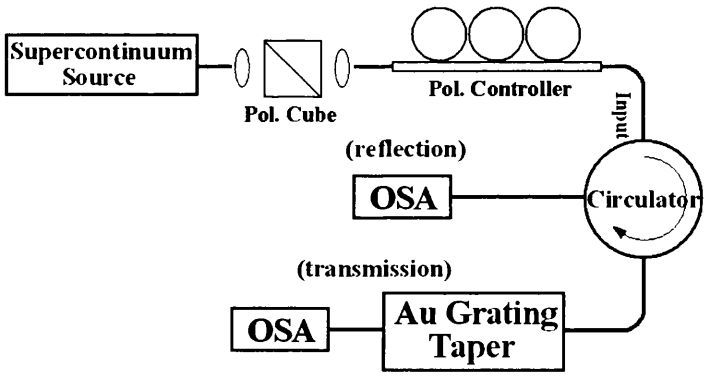

Fig. 4.21. Setup used to study polarization dependence.

Fig. 4.22 shows the measured transmission and reflection spectra in two different input polarization states (black and red curves). A grating taper sample with a Au thickness of 40 nm was used. The transmission dips and reflection peaks represent the mode coupling caused by this grating. The spectra demonstrate a strong dependence on input polarization.

Due to the coiled pigtails in the input and output of the circulator, to the black and red curves, we do not know the exact direction of the input polarization compared with the Au grating strips. However, one possible explanation for this large difference, ~10dB, between the spectra for the two input polarization states is as follows: when the input polarization direction is parallel to the Au strips (i.e. horizontal), the metal absorption is enhanced, so that the intensity of the transmitted and reflected light decreases. This phenomenon is analogous to the polarization dependence described in a metal-coated slab waveguide [Sarid 81], where TM modes suffer much weaker attenuation than TE modes.

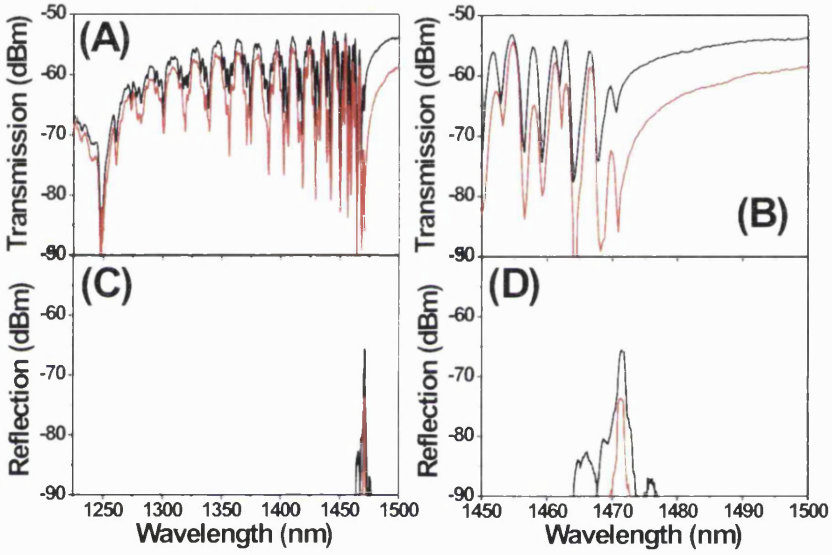

Fig. 4.22. Transmitted (A)(B) and reflected (C)(D) spectra measured at two different polarization states (black and red curves). (B) and (D) were the magnified views of (A) and (C) respectively. The measurement resolution was 1 nm.

4.2.4 Summary

When a longitudinal Bragg grating is created on the surface of a micron-scale fiber taper, the overlap of the evanescent field with the grating structure causes a number of mode couplings. This has been studied in gold Bragg grating fiber tapers fabricated using interference lithography and metal lift-off techniques. This is the first example of producing longitudinal structures along micron-scale fiber tapers. The spectral characteristics have been measured and treated theoretically. The backward coupling to guided and radiation modes and its variation with the refractive index of

the external medium have been studied. A feature occurring at the edge of the radiation coupling continuum shows a high sensitivity to the external medium index and an application in refractometric sensing has been presented.

4.3 Fiber tapers with surface corrugation Bragg gratings

In contrast to last section, this section describes a study of a fiber taper with a surface corrugation Bragg grating. The reflection properties suggest applications in optical fiber filtering.

4.3.1 Working principles

In the absence of a large permittivity contrast such as that between gold and air, mode coupling in a surface grating fiber taper will be very weak due to the small field overlap. Decreasing the taper diameter is a solution but not a good one, since fabrication in a thin fiber taper is a big challenge and only shallow surface structures can be made due to the limit of resist thickness and mechanical robustness. Therefore, in surface corrugated tapers, strong dips in transmission spectra are not expected. This section will thus investigate the reflected spectral properties and deal with mode couplings under the "weak coupling" assumption [Erdogan 97].

Fig. 4.23 shows a fiber taper with a grating taper waist and an adiabatic transition. In the waist part, the input fundamental mode, which is converted from the core mode of the un-tapered fiber via the adiabatic transition, is coupled into a variety of backward modes by a cylindrically asymmetric surface corrugation grating. Amongst all the excited modes, only the backward fundamental mode is ultimately converted into the core mode of the input fiber; other modes are converted into cladding modes and strongly damped due to the lossy interface between the silica fiber and polymer coating [Love 86]. In this way, the grating taper waist acts as a functional part and the adiabatic transition works as a filter, which removes all unwanted backward high-order modes.

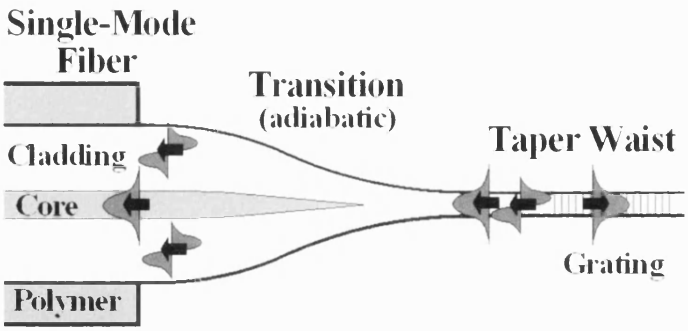

Fig. 4.23. Schematic diagram of a surface grating fiber taper.

Considering only the backward fundamental mode, the resonant condition of a Bragg grating can be expressed as,

$$\lambda_R = 2\Lambda \cdot n_{eff} \tag{4.13}$$

where λ_R is the resonant wavelength, Λ is the grating period, and $n_{eff} = \beta_0 / k_0$ is the effective modal index.

In order to enrich the spectral response of a Bragg grating, a variation of the resonant wavelength along the grating is favourable; otherwise the reflection spectrum will be just a peak. However, introducing variations in the grating period is difficult [Xu 95]. Suggested by Eqn. (4.13), we decided to vary the effective modal index, n_{eff}, along the grating and keep the grating period Λ constant. This can be done via altering the taper diameter along a surface corrugation grating taper. In this way, the effective modal index and the coupling coefficient become functions of the axial coordinate z. Flexible manipulation of the reflection spectrum then becomes possible.

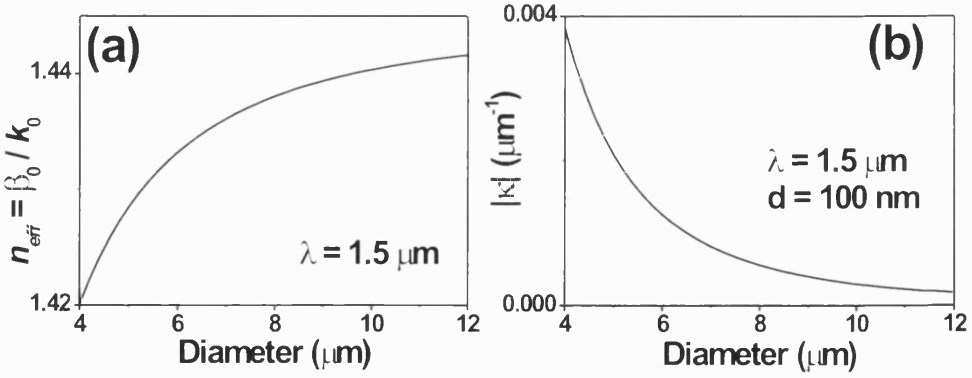

Fig. 4.24. Calculated diameter dependence of (a) effective modal index and (b) coupling coefficient.

Fig. 4.24 shows the dependence of the effective modal index and the coupling coefficient on the taper diameter. The curves in Fig. 4.24 are calculated at a wavelength of 1.5 μm, and we assume that a semi-circular groove (see schematic diagram in Fig. 4.25) is etched on the surface with a depth of 100 nm. The calculation methods of the effective modal index of the eigen-mode and the coupling coefficient have been introduced in chapter 2 and Eqn. (4.3), respectively. From Fig. 4.24, it is clear that only when the taper diameter decreases to the micron scale, do the diameter dependences become significant. For example, when the taper diameter decreases from 10 μm to 6 μm, the effective modal index has a change of 0.007, which is bigger than the refractive index difference between the core and the cladding of a conventional SMF-28 fiber. This big adjustment range provides a freedom to flexibly manipulate the resonant condition of Eqn. (4.13).

Experimentally, the diameter variation in a fiber taper is limited by another factor: if the diameter along the taper is non-uniform, the thickness of the resist film applied on the taper will vary, so that the quality of the interference lithographic patterns will be degraded.

4.3.2 Theoretical treatment

Fig. 4.25 shows a sketch of the variable-diameter grating fiber taper. The taper diameter D is a function of the axial coordinate z. The grating period is constant in the range from $z = 0$ to L. The etch grooves are assumed to be semi-circular.

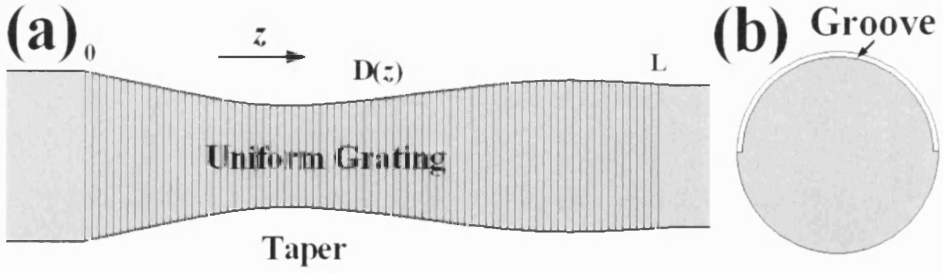

Fig. 4.25. (a) Longitudinal and (b) cross sectional views of a variable-diameter grating fiber taper.

In reflection spectra, only the coupling between two contra-propagating fundamental modes needs to be considered. These two modes are respectively expressed as,

$$\mathbf{E}_f(x,y,z) = A_f(z)\exp[i\int_0^z \beta_0(z')dz']\hat{\mathbf{e}}_f(x,y,z) \tag{4.14a}$$

$$\mathbf{E}_b(x,y,z) = A_b(z)\exp[-i\int_z^L \beta_0(z')dz']\hat{\mathbf{e}}_b(x,y,z) \tag{4.14b}$$

where, $\hat{\mathbf{e}}_{f,b}$ represent normalized fundamental modes, $\beta_0(z)$ is the mode propagation constant, and $A_{f,b}(z)$ is the field amplitude.

With the "weak coupling" assumption,

$$A_f(z) \approx A_0, \quad |A_b(z)| << |A_0| \tag{4.15}$$

the coupling equation is given by,

$$\frac{dA_b(z)}{dz} = \frac{A_0}{n_{eff}(z)}\exp[-i\int_0^L \beta_0(z')dz']\exp[i2\int_0^z \beta_0(z')dz']\kappa(z) \tag{4.16}$$

where the effective modal index is $n_{eff}(z) = \beta_0(z) / k_0$ and the coupling coefficient is

$$\kappa(z) = -\frac{i\omega c\mu}{4}\int_{A_\infty} \Delta\varepsilon(x,y,z)[\hat{\mathbf{e}}_f(x,y,z)\times\hat{\mathbf{h}}_b^*(x,y,z)]\cdot\hat{\mathbf{a}}_z dA \tag{4.17a}$$

$$\frac{1}{2}\int_{A_\infty} [\hat{\mathbf{e}}_f(x,y,z)\times\hat{\mathbf{h}}_f^*(x,y,z)]\cdot\hat{\mathbf{a}}_z dA = 1 \tag{4.17b}$$

The reflectivity of the grating taper is given by

$$R(\lambda) = \left|\frac{A_b(z=0)}{A_0}\right|^2 \tag{4.18}$$

and is a function of the taper diameter profile

$$R(\lambda) = \sigma\{D(z)\} \tag{4.19}$$

4.3.3 Device description

Using the taper rig developed by Tim Birks et al, any monotonically decreasing taper diameter profile can be produced [Birks 92]. Three types of taper sample with different diameter profile were produced:

- Type I: uniform taper diameter;
- Type II: V-shaped taper diameter;
- Type III: linearly decreasing taper diameter.

Planar fabrication processes, like those described in subsection 4.1.1, were then carried out. Fig. 4.26 shows the flow chart for these processes.

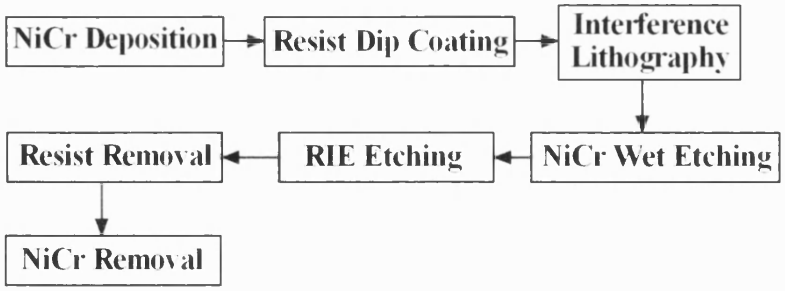

Fig. 4.26. Flow chart of the fabrication process.

After NiCr deposition and resist dip coating on a fiber taper, a uniform Bragg grating in a resist layer was produced by interference exposure and development. After removing the NiCr layer between the resist strips by wet etching, reactive ion etchings with trifluoromethane (CHF_3) and an inductively coupled plasma source were used to create surface corrugations on the taper. An Oxford Plasmalab 80 plus ICP system was used. The flow rate of the CHF_3 gas was 7 sccm (standard cubic centimetres per minute), the forward power was 50 W, the ICP power was 500 W, the DC Bias was 180 V, the chamber pressure was 5 mbar, the strike pressure was 30 mbar, and the ramp rate of the pressure was 8. The etch rate to pure silica is around 14 nm/min.

Finally, the residual resist and NiCr were removed. Fig. 4.27 shows a scanning electron micrograph of a grating fiber taper of type I. The ~10 mm-long grating lies in the middle of the uniform-diameter taper waist, which is 20 mm long. The two taper transitions are 20 mm long. The measured waist diameter and grating period are 9.72 μm and 522.4 nm, respectively. From the known etch rate (≤14 nm/min for the sub-micron-wide trenches) and time (~14 minutes), the depth of the etched grooves is estimated to be between 150 and 200 nm.

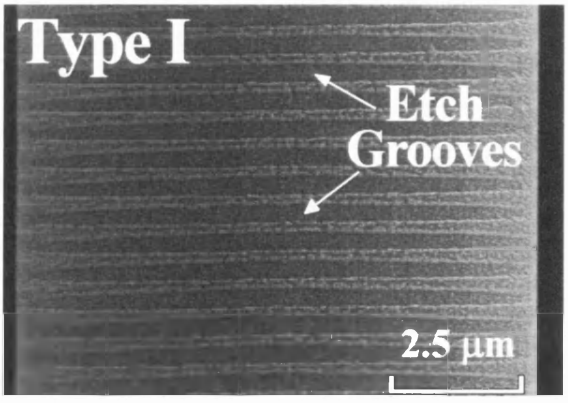

Fig. 4.27. Scanning electron micrograph of a surface corrugation grating taper.

Constant period surface corrugation Bragg gratings were also produced on two variable-diameter taper waists (type II and III). The grating periods of these two samples are 521.8 nm (type II) and 533.6 nm (type III), respectively. A series of SEM images were then taken to determine the taper diameter profiles in the grating regions, which are shown in Fig. 4.28.

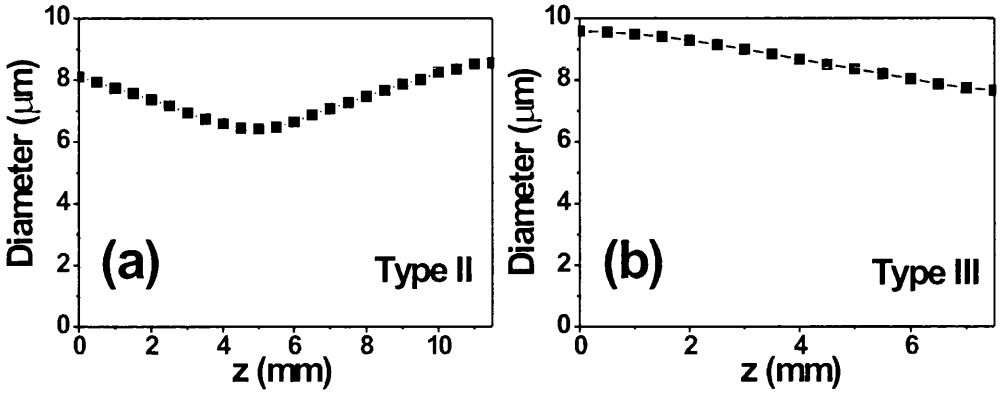

Fig. 4.28. Diameter profiles in the grating regions of (a) type II and (b) type III tapers.

4.3.4 Spectral measurements and analysis

Measurements were made using an ultrabroadband supercontinuum source, generated from an endlessly single mode photonic crystal fiber (ES-PCF), an optical circulator and two optical spectral analysers (OSAs). (see Fig. 4.12)

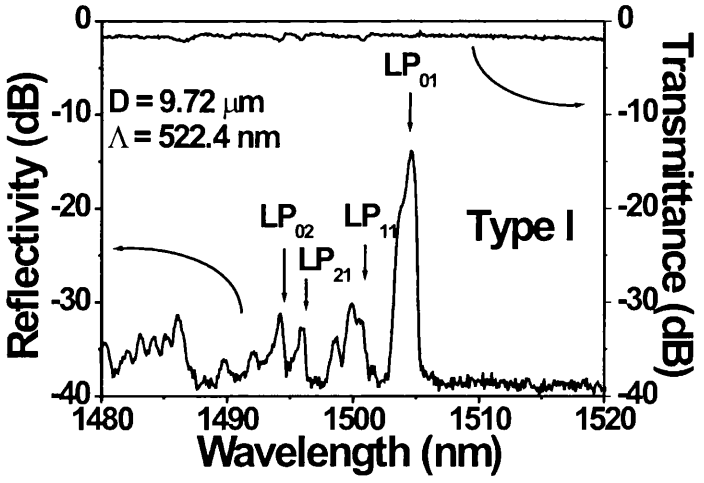

Fig. 4.29. Transmittance (upper curve) and reflectivity (lower curve) spectra of the type I sample. A measurement resolution of 0.5 nm was used.

Fig. 4.29 shows the transmittance and reflectivity spectra of the sample of type I (see the SEM image in Fig. 4.27). First of all, it is clear that there is no dip appearing in the transmittance spectrum, and the ~0 dB transmittance verifies the "weak coupling" supposition used in the previous theoretical treatment. Note that this is the total transmission loss after all processing steps. Secondly, multiple peaks appear in the reflectivity spectrum due to coupling to different backward modes. The FWHM of the main peak is ~0.7 nm for a measurement resolution of 0.5 nm. Using the measured taper diameter (D = 9.72 μm) and grating period (Λ = 522.4 nm), the calculated resonant wavelengths of the corresponding modes are shown in Fig. 4.29 and agree with these reflection peaks, which are all located on the shorter wavelength side of the main peak. The strength of the coupling to high-order modes is suppressed by at least 10 dB comparing with the coupling to the fundamental mode. This is ascribed to the filtering effect of the adiabatic taper transition on high-order modes, as described previously. In another sample prepared with a longer, therefore more adiabatic, taper transition of 25 mm, a higher suppression of 20 dB had been obtained.

For diameter-variable grating fiber tapers (type II and III), Figs. 4.30 a and b show the measured (M) and calculated (C) reflectivity spectra of the samples. The non-uniform waist diameter profiles cause broadening of the reflection peaks to 5.2 nm and 3.7 nm, respectively.

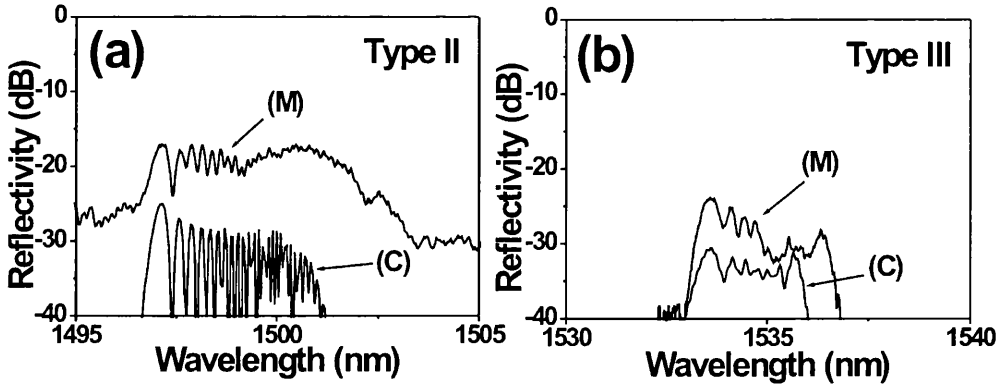

Fig. 4.30. Measured (upper curves) and calculated (lower curves) reflection spectra of samples of (a) type II and (b) type III.

In Fig. 4.30a, the V-shaped diameter profile of the taper of type II produces many dips in the spectrum. The reflected components from the two sides of the V-

shaped grating waist add constructively or destructively. In the calculation, the measured diameter profile (Fig. 4.28a) and the grating period (Λ = 521.8 nm) are used. The etched grooves are assumed to be semi-circular, and the width of the etched strip is 50% of the grating period. The etch depth of the grating is adjusted for obtaining agreement with measurement.

For the sample of type III, the interference effect between two sides of the grating region disappeared. However, the sum of the reflected components is still dependent on the wavelength. For different wavelengths, the reflection occurs in different grating regions with different intensity. Therefore, undulations can still be found in the spectrum of Fig. 4.30b, although they become more separated and shallower than those in Fig. 4.30a. The calculation in Fig. 4.30b uses the diameter profile shown in Fig. 4.28b and the grating period of Λ = 533.6 nm.

Fig. 4.31 schematically illustrates the effects discussed above.

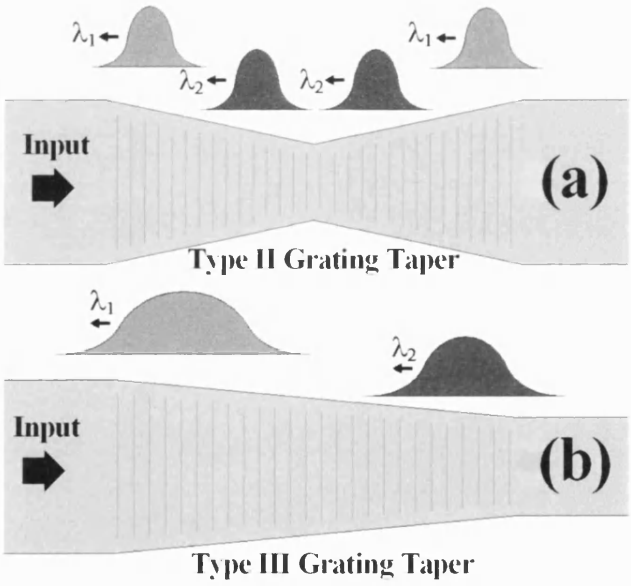

Fig. 4.31. Interferometric sums of reflected fields at different wavelengths in grating tapers of (a) type II and (b) type III.

The results from these three surface grating taper samples experimentally verify the principle presented in subsection 4.2.1. Novel control to the spectral properties of an optical filter device is achieved by altering the shape of the fiber taper, which is much easier than varying the grating period. In this way, the reflection spectrum becomes a function of the diameter profile (Eqn. 4.19).

4.3.5 Summary

This section has presented a second example of producing longitudinal structures along micron-scale fiber tapers. A reflection-based optical fiber filter has been fabricated by writing a surface corrugation Bragg grating on a fiber taper. The grating taper waist and the adiabatic taper transition play the roles of functional part and unwanted mode remover, respectively. The reflection spectrum can be manipulated by altering the shape of the fiber taper. This method of using a constant grating period and a variable taper diameter is much more straightforward and easier than writing a variable-period grating.

4.4 Conclusions

Transferring planar fabrication processing techniques to the curved surface of a micron-scale fiber taper poses a challenge. In this chapter, we have described a suitable technology. As examples, two devices with Bragg gratings along micron-scale fiber tapers have been described. Their possible applications as refractometric sensors and optical fiber filters were presented.

Chapter 5

Other Longitudinal Structures on Fiber Tapers

5.1 Introduction

The last chapter presents methods for creating Bragg gratings on fiber tapers. Using the interference lithography technique, periodic patterns were produced. But, if more complicated patterns are required, other fabrication techniques, such as contact optical lithography and focused ion beam milling, have to be adopted. This chapter presents the application of these two techniques to fiber tapers. The motivation is, still, to explore applications as fiber taper devices.

5.2 Contact optical lithography technique applied to fiber tapers (long period gratings)

5.2.1 Contact optical lithography technique

As mentioned in chapter 3, contact optical lithography [Shon-Roy 98] can deal with various patterns previously produced on photo masks. Its minimum feature size is limited by optical diffraction. When light irradiates an aperture in a photo mask, the width of the transmitted beam expands behind the aperture as shown in Fig. 5.1. If we want to weaken this influence of optical diffraction, a resist layer must be put in close proximity to the photo mask. However, this requirement is hard to be fulfilled for fiber tapers. The curved surface of fiber tapers is intrinsically not compatible with a planar photo mask. Therefore, applying contact optical lithography to fiber tapers will suffer severe diffraction problems and can only produce large-sized features.

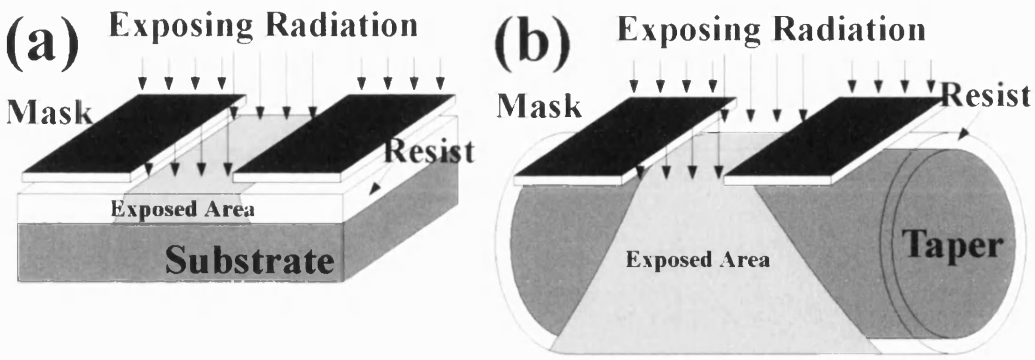

Fig. 5.1. Expansion of the beam behind the photo-mask causes optical diffraction problem in (a) a planar sample and (b) a fiber taper sample.

5.2.2 Fabrication of long period grating fiber taper

Long period gratings have been fabricated along fiber tapers using contact optical lithography technique [Shon-Roy 98].

Firstly, a photo mask was produced on a glass slide following the flow chart shown in Fig. 5.2. A 200 nm thick of NiCr layer was deposited on the glass slide, and then photolithography and wet etching were applied.

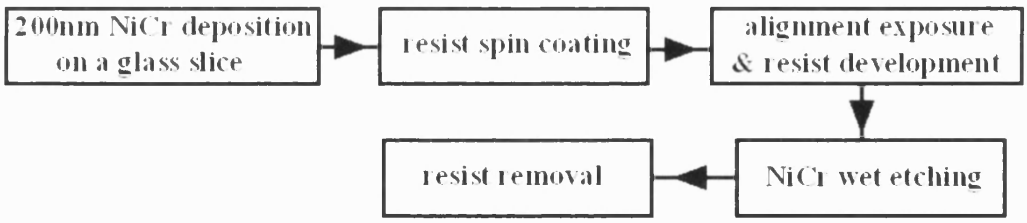

Fig. 5.2. Flow chart of process used to produce photo-masks.

The resulted photo mask had a grating period of 200 μm and a filling fraction of ~50% as shown in Fig. 5.3.

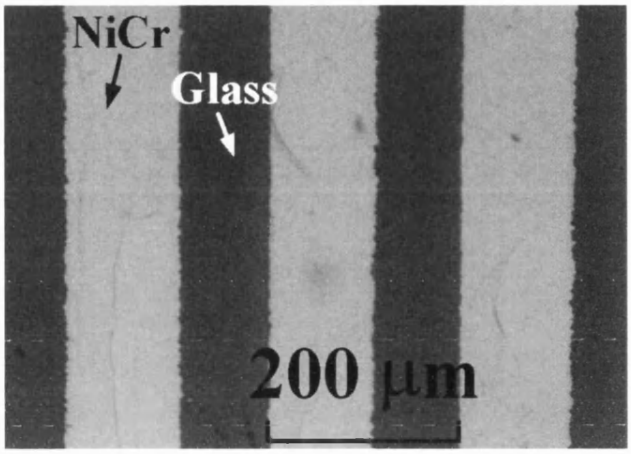

Fig. 5.3. Photo-micrograph of the photo-mask.

In the next step, a fiber taper with a uniform-diameter and several-cm-length waist was mounted on a microscope slide (see Fig. 4.1). Photo resist dip coating was applied. Aligning this fiber taper with the photo mask (see Fig. 5.4), we produced periodic resist rings in the taper waist region after exposure and development. These rings were approximately radially symmetric, since the exposing light can penetrate the transparent fiber taper and illuminate the resist on the backside.

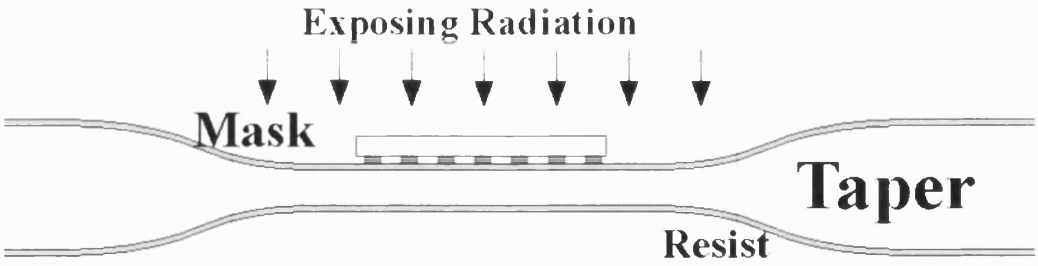

Fig. 5.4. Exposure of the LPG fiber taper.

In the development step, the resist on both ends of the taper was removed, so that two more resist dip coatings, which stopped near the edges of the grating, were required after that. The newly applied resist layer protected the fiber taper in the subsequent HF etching step and determined the length of the grating area.

Finally, after HF etching and resist removal, a periodic modulation of the taper diameter was left in the taper waist. Fig. 5.5 showed the photo micrograph of this long period grating fiber taper. In order to enhance the colour contrast, this picture was taken before resist removal. The taper diameter, D, was 12 μm, the grating period, Λ,

was 200 μm, the grating length, L, was 11 mm (corresponding to 55 periods), and the etch depth, d, was ~0.3 μm.

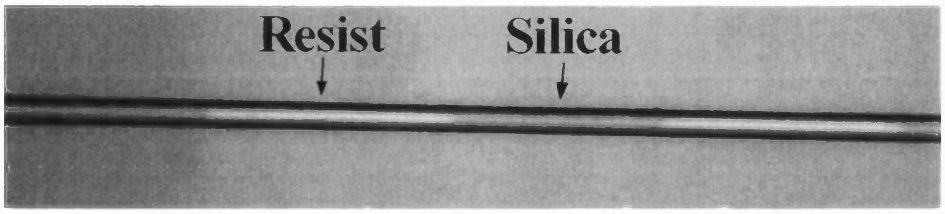

Fig. 5.5. Photo micrograph of the long period grating taper sample. D = 12 μm, Λ = 200 nm, L = 11 mm, d = 0.3 μm.

5.2.3 Theoretical treatment and spectral characterisation

Due to the radial symmetry of the etched grooves, this long period grating taper shows small polarization dependence; grating induced mode couplings occur only amongst forward LP_{0m} modes. The resonant wavelength can be expressed as a function of the grating period and the taper diameter:

$$\lambda_R = \Lambda[n_0(\lambda_R, D) - n_m(\lambda_R, D)] \tag{5.1}$$

where, n_m is the effective modal index of the LP_{0m} mode.

Fig. 5.6a is the transmission spectrum of the sample shown in Fig. 5.5. Coupling between the fundamental mode and the LP_{02} mode occurs at a wavelength of 888.5 nm. The bandwidth of the transmission dip, ~30 nm, is consistent with the relation $\Delta\lambda \approx 2\lambda_R / N$ [Erdogan 97], where λ_R is the resonant wavelength and N = 55 is the number of periods. By controlling the etch depth, the depth of the transmission dip can increase. Fig. 5.6b shows the transmission spectrum of another sample, where a depth greater than 15 dB is observed. The parameters of this LPG taper sample are shown in Fig. 5.6b.

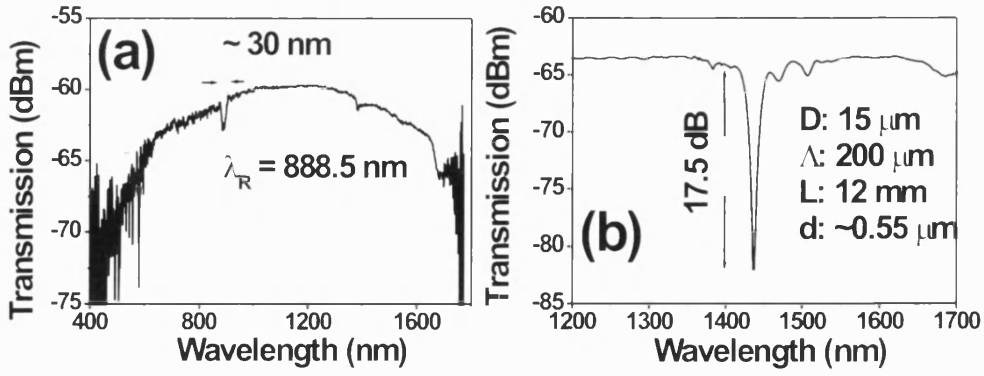

Fig. 5.6. Transmission spectra of (a) the sample shown in Fig. 5.5 and (a) a new sample.

A series of LPG taper samples had been made with different taper diameter and grating period. Fig. 5.7 shows the calculated (solid curves) and measured (solid dots) resonant wavelengths. Only the coupling between the LP_{01} and LP_{02} modes is considered. In calculations, Eqn. (5.1) is used. The fit between the calculated and measured values is very good.

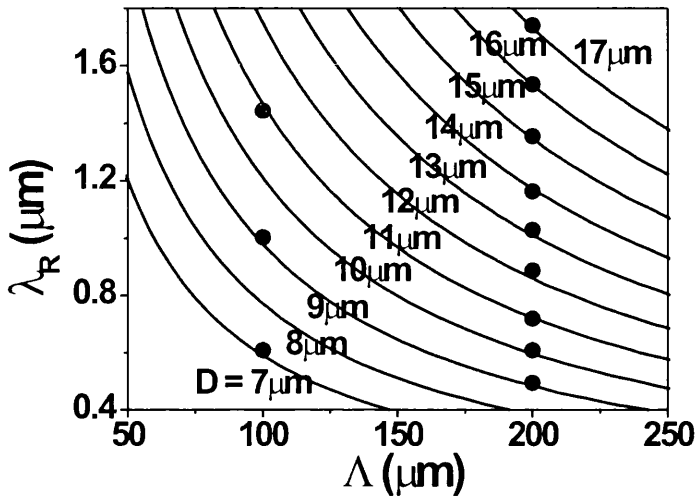

Fig. 5.7. Resonant wavelengths of LPG fiber tapers as a function of grating period Λ and taper diameter D. The calculated curves are based on Eqn. (5.1). The measured values are shown by solid circles.

5.2.4 Summary

Due to serious optical diffraction problems, the application of contact optical lithography on a fiber taper is only suitable for producing large-sized features. Using this technique together with HF etching, radially symmetric long period grating grooves have been written on the surface of fiber tapers. These devices can be used as wide band filters [Vengsarkar 96] and optical sensors [Chiang 00]. The LPG fiber tapers fabricated with lithographic technique have the merit of small polarization dependence, compared with those produced by CO_2 laser heating [Kakarantzas 02].

5.3 Focused Ion Beam milling technique applied to fiber tapers (micro-cavities)

5.3.1 Focused Ion Beam milling technique

Focused Ion Beam (FIB) milling is a powerful tool for producing high-resolution deep features in various substrates [Gierak 99]. It can write arbitrary patterns with small feature size (~10 nm [Gamo 97]) and without a mask. In ref. [Gibson 05], the application of FIB milling in silica fiber has proven to be successful. Here, we use this technique to write micro-cavity structures along fiber tapers. Numerical simulations and initial fabrication trials are demonstrated, although spectral measurements have not been carried out due to bad fabrication qualities.

5.3.2 FDTD simulations

Before fabrication, it is useful to anticipate optical responses of the proposed micro-cavity structured fiber tapers. This can be done using a commercial FDTD [Taflove 97] simulation package, OptiFDTD [OptiFDTD 5.0].

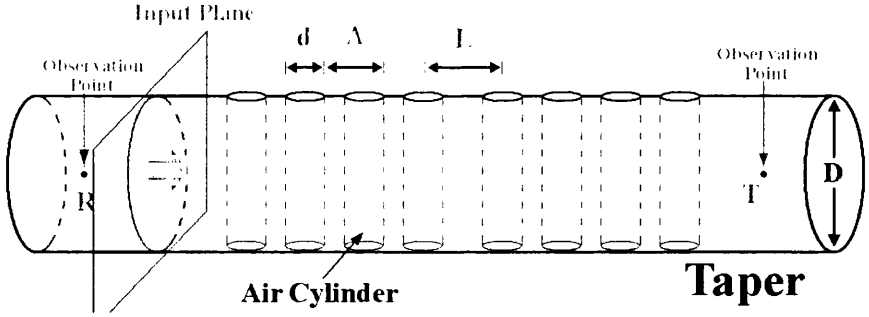

Fig. 5.8. Sketch of the first simulated structure. Air cylinders are arranged along the fiber tapers.

Fig. 5.8 shows the first simulated micro-cavity structure, which consists of two reflectors and one cavity. The taper diameter is 2 μm, the cavity length, L, is 800 nm, and each reflector extremity consists of four periodically arranged air cylinders with the diameter of d = 400 nm and the period of Λ = 600 nm.

OptiFDTD automatically generated a transverse modal field distribution for this waveguide and launched it into the micro-cavity structure from the input plane shown in Fig. 5.8. The input polarization was set to be perpendicular to the direction of the air cylinders. The time variation of the input wave was modulated with a

Gaussian pulse of the required bandwidth. Two on-axis observation points (T and R in Fig. 5.8) were set in front of and behind the micro-cavity structure respectively. The field evolutions recorded at these two points were used to calculate the transmittance and reflectivity spectra through a Fourier transformation processing [Mekis 96].

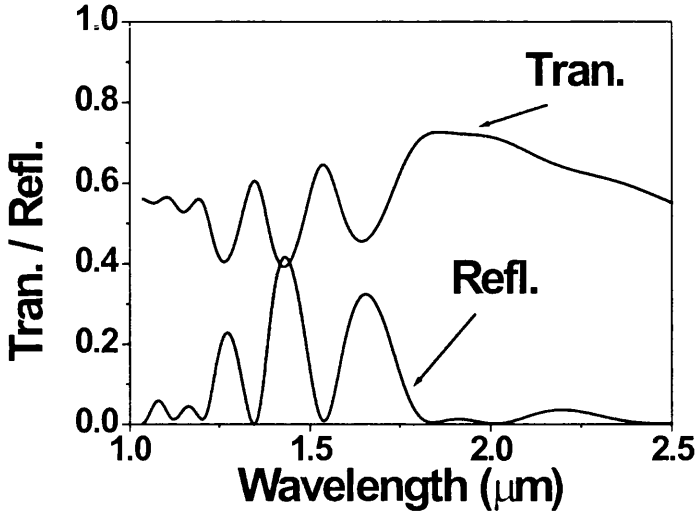

Fig. 5.9. Transmittance (upper curve) and reflectivity (lower curve) spectra of the structure shown in Fig. 5.8.

Fig. 5.9 shows this transmittance and reflectivity spectra. The expected micro-cavity spectral features, for example a narrow peak in transmission spectrum and a narrow dip in reflection spectrum [Foresi 97], do not appear. This might be ascribed to the curved surfaces of the air cylinders: most of the reflected waves from the air cylinder surfaces are off-axial and coupled to radiation or high-order modes; they do not interfere with the reflected components from other air cylinders; so that the micro-cavity spectral features do not appear.

A second micro-cavity taper structure, in which air cylinders are substituted by infinite air slices, is shown in Fig. 5.10. Now, all transverse interfaces between silica and air are planar and normal to the propagation direction. The reflected waves will thereby not be scattered to off-axial directions.

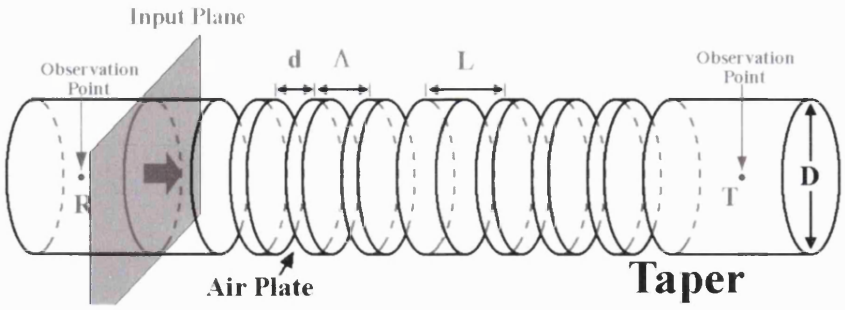

Fig. 5.10. Sketch of the second simulated structure. Infinite air slices vertically insert the fiber taper.

Assuming the taper diameter to be 4 μm, the thickness of the air slices to be 391.6 nm, the period to be 661.8 nm, and the cavity length to be 941.6 nm, the simulated transmittance and reflectivity spectra are shown in Fig. 5.11. The spectral characteristics of a micro-cavity are revealed.

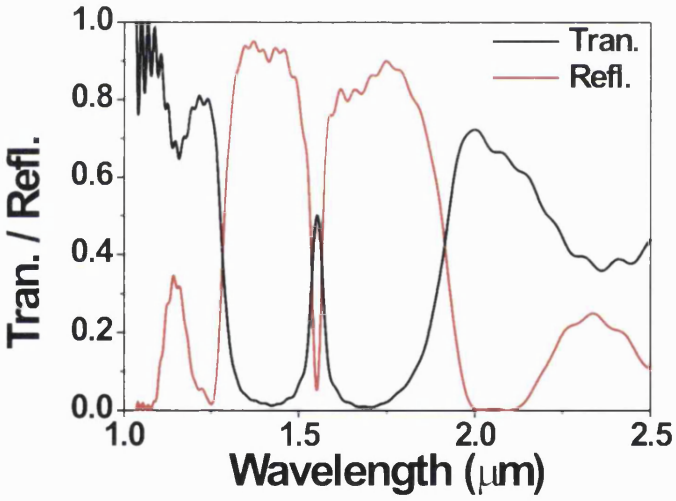

Fig. 5.11. Transmittance (black) and reflectivity (red) spectra of the structure shown in Fig. 5.10.

Taking into account the practical fabrication limitation, air slots with a width of 3 μm rather than infinite air slices are used in Fig. 5.12. Here, the taper diameter is 4 μm, the air slot thickness is 395 nm, the period is 667 nm, and the cavity length is 951 nm. The input polarization is parallel to the direction of the air slots. Fig. 5.13 shows the simulated spectra, where the micro-cavity spectral characteristics are

retained. In all above simulations, the mesh size was set to be 30 nm for obtaining a good numerical precision [Taflove 97].

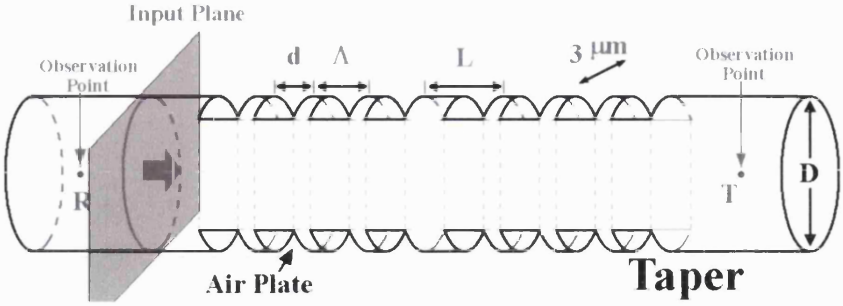

Fig. 5.12. Sketch of the third simulated structure. The infinite air slices in Fig. 5.10 are substituted by the air slots with width of 3 μm.

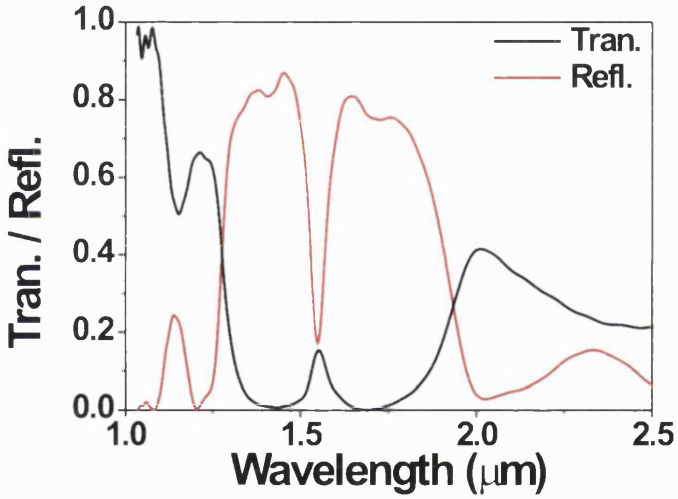

Fig. 5.13. Transmittance (black) and reflectivity (red) spectra of the structure shown in Fig. 5.12.

Comparing Figs. 5.11 and 5.13, we find the width of the pass band of the micro-cavity filter becomes broad as the air slot width decreases. This implies that, in order to maintain the micro-cavity spectral characteristics, the air slots should be wide enough. In fabrication, this requirement constitutes a trade-off with the demand of mechanical robustness.

5.3.3 Fabrication

The fabrication can be separated into two stages: preparation of fiber tapers and FIB milling.

In the first stage, a fiber taper was made and mounted on a microscope slide. An appropriate taper tension was introduced in the mounting step, so that the freestanding taper would not drift during FIB milling. However, too strong a tension would make the taper fragile and likely to snap. The mounting step was therefore very crucial. In experiments, we did this fiber stretching process by adding a drop of glue in the suspending part of the fiber taper.

After preparation of the fiber taper, a layer of NiCr was deposited on the top to make sample electrical conductive. Then, FIB milling was carried out in School of Physics of University of Exeter with the assistance of Dr. Andy Murray and Prof. Bill Barnes. A combined FIB/SEM system (FEI's DualBeam^{TM}) was used. The etch rate was around 1 μm^3/min.

The FIB milling machine could completely drill through our thin tapers, but taper snapping occurred frequently. Fig. 5.14 shows a row of holes in a 1.77 μm-diameter fiber taper. The bright dot in the middle of each hole verifies that the holes have been drilled through.

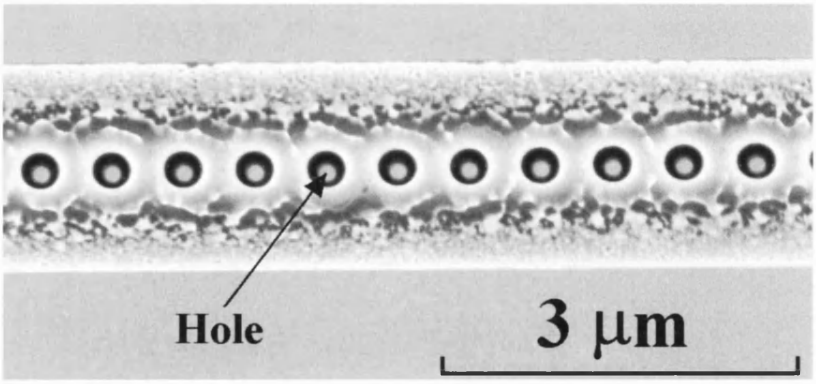

Fig. 5.14. Scanning electron micrograph of drilled holes on a fiber taper.

Fig. 5.15 shows a scanning electron micrograph of a micro-cavity structured fiber taper. The taper diameter is 3.1 μm, the air slots have a width of 850 nm and a thickness of 425 nm, the period is 730 nm, and the cavity length is 1.04 μm. Comparing with the required sizes shown in Fig. 5.12, more efforts are still needed to make these air slots wider.

Due to the poor fabrication quality and the unsuccessful handling, the fiber taper shown in Fig. 5.15 broke when we tried to remove its NiCr coating. Hence, the optical characterisation to this sample had not been carried out yet.

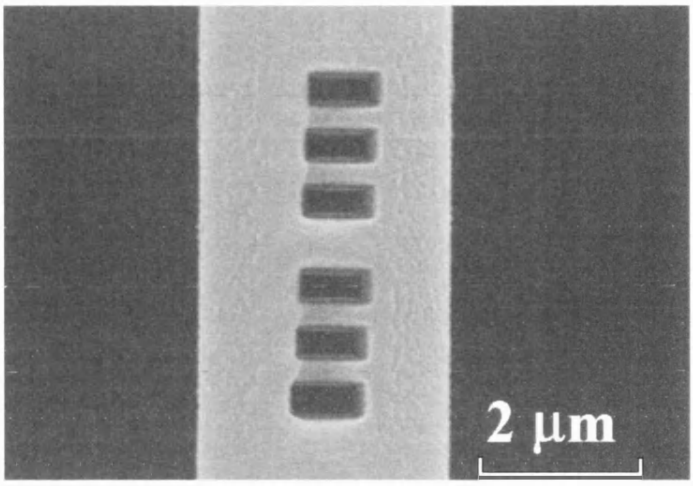

Fig. 5.15. Scanning electron micrograph of drilled square holes on a fiber taper.

5.3.4 Summary

FIB milling has shown potentials for producing longitudinal structures directly in fiber tapers. The advantage of this technique is its high resolution and ability to etch deep trenches. Preliminary works in simulation and fabrication are promising, but more effort is still needed to produce a real device. The drawback of this device is its fragility, which also makes fabrication difficult.

5.4 Conclusions

Contact optical lithography and focused ion beam milling techniques have been used to form longitudinal structures along fiber tapers. Using contact optical lithography and HF etching, long period radially symmetrical groove gratings have been produced on the surface of fiber tapers. This radial symmetry helps eliminate polarization dependence in devices. However, due to serious optical diffraction, this technique is only suitable for large-sized features. On the other hand, with the high resolution and deep etching capability of the FIB milling, producing sophisticated structures directly in fiber tapers has been explored. Numerical simulations and trial fabrication have been done. But, more research is still needed to overcome the taper snapping problem before a real device can be made.

Chapter 6

Internal Excitation and Superfocusing of Surface Plasmon Polaritons on an Apertureless Silver-Coated Fiber Tip

6.1 Introduction

This chapter presents our studies to another tapered optical fiber device: an apertureless silver-coated fiber tip. The goal was to obtain field concentration at the silver apex based on surface plasmon polaritons (SPPs). This phenomenon is known as superfocusing. The excitation of SPPs from fiber waveguide modes via this device is studied theoretically.

The first section briefly explains SPPs and the superfocusing phenomenon in metallic tips. Their applications in scanning near-field optical microscopy and the idea of internally exciting SPPs in a finite thick silver-coated fiber tip are also presented. The subsequent three sections investigate this internal excitation and superfocusing using analytical and numerical methods. The last section summarizes our conclusions.

6.1.1 Surface plasmon polaritons (SPPs)

Following the pioneering work of Ritchie [Ritchie 57], surface plasmon polaritons (SPPs) have been widely recognized in the field of surface science. SPP are charge density waves on the surface of materials with free electrons (metals, plasmas, etc.) coupled to the electromagnetic field and propagating along the interface of this conductor and a dielectric medium. It is possible to excite SPPs via light if appropriate phase-matching conditions are satisfied. In order to solve out SPP modes on surface of metal, Maxwell's theory is used, and the dielectric function of metals can be fitted using a Lorentz-Drude model [Rakic 98].

The properties of SPP waves are strongly dependent on geometry [Maier 06]. For the simplest case of a single flat interface, the wave profiles and the wave vectors of SPPs are schematically shown in Fig. 6.1. Here, a TM field is confined at the metal-dielectric boundary with tangential wave-vector of [Burnstein 74],

$$\beta_{12} = k_0\sqrt{\frac{\varepsilon_1\varepsilon_2}{\varepsilon_1+\varepsilon_2}}, \text{ or } \beta_{13} = k_0\sqrt{\frac{\varepsilon_1\varepsilon_3}{\varepsilon_1+\varepsilon_3}} \tag{6.1}$$

where k_0 is the free-space wave vector, ε_1 is the metal dielectric constant, ε_2 and ε_3 are the dielectric constants of the surrounding media.

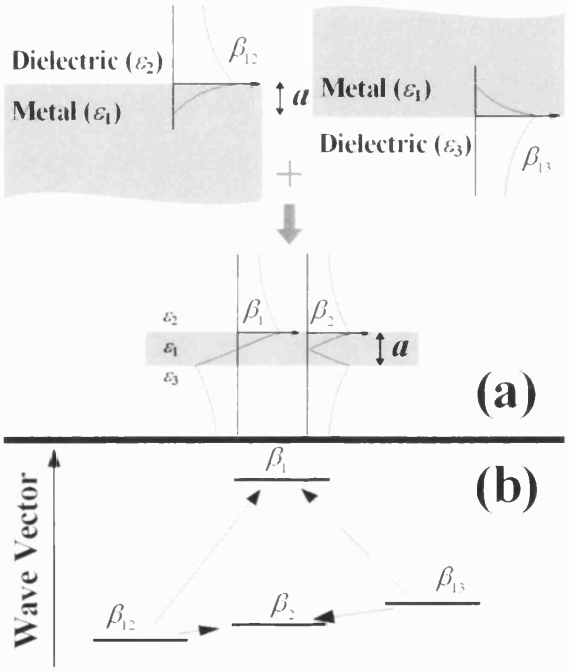

Fig. 6.1. SPPs at flat metal-dielectric interfaces in (a) real and (b) wave vector spaces.

When the single interface is transformed to a double-interface geometry as shown in Fig. 6.1a, the SPP fields in two single-interface structures are constructively or destructively superposed (Fig. 6.1a), and two hybrid SPP modes with wave vectors of β_1 and β_2 are formed (Fig. 6.1b). In the wave vector coordinate shown in Fig. 6.1b, the degeneracy of β_{12} and β_{13}, supposing $\varepsilon_2 = \varepsilon_3$, is lifted. The two branches of β_1 and β_2 can be expressed as [Sarid 81]:

$$\frac{\sqrt{\beta^2-k_0^2\varepsilon_1}/\varepsilon_1+\sqrt{\beta^2-k_0^2\varepsilon_2}/\varepsilon_2}{\sqrt{\beta^2-k_0^2\varepsilon_1}/\varepsilon_1-\sqrt{\beta^2-k_0^2\varepsilon_2}/\varepsilon_2}\times\frac{\sqrt{\beta^2-k_0^2\varepsilon_1}/\varepsilon_1+\sqrt{\beta^2-k_0^2\varepsilon_3}/\varepsilon_3}{\sqrt{\beta^2-k_0^2\varepsilon_1}/\varepsilon_1-\sqrt{\beta^2-k_0^2\varepsilon_3}/\varepsilon_3} = \exp(-2a\sqrt{\beta^2-k_0^2\varepsilon_1}) \tag{6.2}$$

where a is the metal thickness. As a decreases, the separation between β_1 and β_2 increases.

As an example, for a silver film, Fig. 6.2 shows the variation of $n_{1,2} = \beta_{1,2} / k_0$ with silver thickness at a wavelength of 1.55 μm.

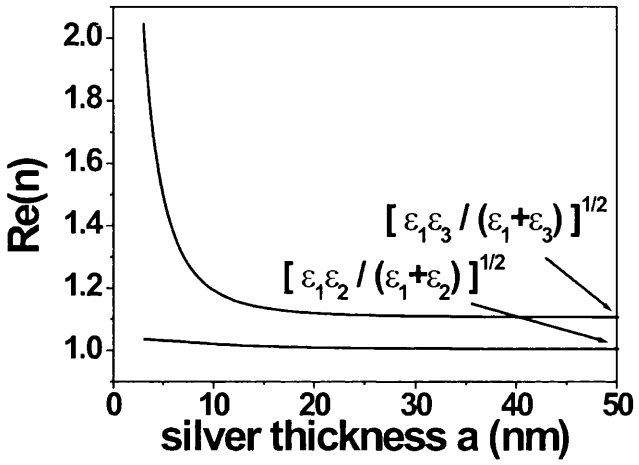

Fig. 6.2. Dispersion curves of real part of the effective indices of the SPP modes in a silver film. Here $\varepsilon_2 = 1$, $\varepsilon_3 = 1.21$, $\lambda = 1.55$ μm, and $\varepsilon_1 = -103+8i$.

The above SPP phenomena have counterparts in cylindrical geometries, where the TM polarization corresponds to radial polarization [Al-Bader 92]. Fig. 6.3 shows the geometry change from single-interface to double-interface and the superposition of the SPP wave profiles in the cylindrical case. The wave vectors of the hybrid SPPs in the double-interface geometry split as well. In reference [Prodan 03], it is shown that this splitting is analogous to that occurring in a covalent bond: i.e. when two isolated atoms approach each other, the superposed modes are formed and the atomic energy levels split.

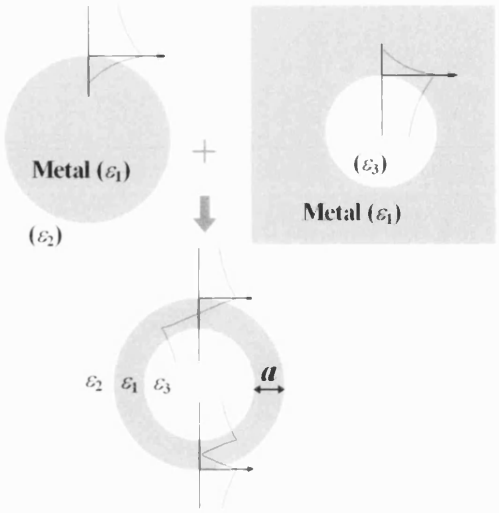

Fig. 6.3. SPPs at cylindrical metal-dielectric interfaces.

In above discussions, the metal dielectric constant is approximately regarded as a large negative value, which enables surface guiding of the electromagnetic field. Considering a realistic metal, the dielectric constant has a non-zero imaginary part, which signifies dissipation and reduces the propagation length of SPPs. A real dielectric constant can be expressed with Lorentz-Drude model [Rakic 98]:

$$\varepsilon(\omega) = \varepsilon^{(f)}(\omega) + \varepsilon^{(b)}(\omega) \tag{6.3}$$

Here, the first term is the Drude or free-electron term referring to intraband excitations; the second one is the Lorentz term referring to inter-band transitions. They have the following forms, respectively:

$$\varepsilon^{(f)}(\omega) = 1 - \frac{f_0 \omega_p^{\ 2}}{\omega^2 + i\omega\Gamma_0}, \qquad \varepsilon^{(b)}(\omega) = \sum_{j=1}^{N} \frac{f_j \omega_p^{\ 2}}{\omega_j^{\ 2} - \omega^2 - i\omega\Gamma_j} \tag{6.4}$$

where, ω_p is the plasma frequency, N is the number of the oscillators with resonant frequency ω_j, strength f_j, and damping constant Γ_j. In this chapter, our investigations concentrate on the metal silver in the visible and near-infrared for obtaining a relatively small metal dissipation.

6.1.2 SPP Superfocusing on a conical silver tip

As shown in Fig. 6.2, the modal index splitting in a flat silver film causes the upper mode branch to rise to infinity as the film is thinned [Nerkararyan 97]. This property has an important consequence: as the mode index increases, the effective wavelength of the SPP mode, $\lambda_0 k_0/\beta$, decreases, and the mode energy is dramatically concentrated in both transverse and longitudinal dimensions. This phenomenon is

known as superfocusing and has a counterpart in the cylindrical geometry [Stockman 04]. Moreover, in the planar geometry shown in Fig. 6.1, the SPP superfocusing is only dependent on the film thickness; whereas, in the cylindrical geometry shown in Fig. 6.3, both the metal thickness and the cylinder radius can influence superfocusing. This will be discussed in next sections.

The SPP superfocussing in the cylindrical geometry, for example in a silver cone, can be dealt with in a spherical coordinate system with an expansion basis of spherical Bessel functions [Babadjanyan 00]. In Fig. 6.4, the origin of the spherical coordinate system is set at the apex, the polar axis is set along the axis of the cone, the cone apex angle is 2α, and the regions inside and outside the cone are filled with silver (ε_1) and dielectric (ε_2) respectively. Considering a radially polarized mode, the magnetic field has only the azimuthal component (H_φ), and the electric field has both radial and zenithal components (E_r, E_ϑ). Assuming $\alpha << 1$ and that the metal dissipation is insignificant, the field amplitudes and propagation constant near the apex obey following relations [Babadjanyan 00]:

$$|H_\varphi| \sim r^{-1/2},\ |E_r|, |E_\vartheta| \sim r^{-3/2},\ \beta \sim r^{-1} \tag{6.5}$$

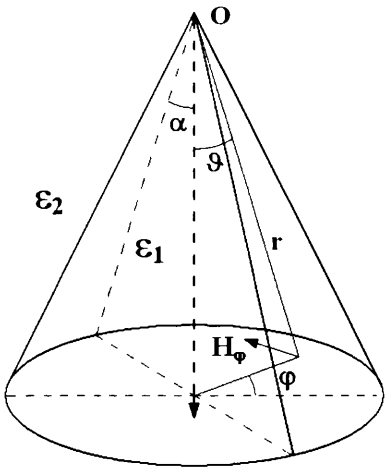

Fig. 6.4. A silver cone (adapted from ref. [Babadjanyan 00]).

The above results can also be obtained by calculating eigen-modes in a cylindrical silver waveguide [Novotny 94]. To corroborate Eqn. (6.5), we use the methods described in section 2.2. In the cylindrical coordinate system shown in Fig. 6.5, the radially-polarized eigen-modes have field components of H_ϕ, E_r, and E_z.

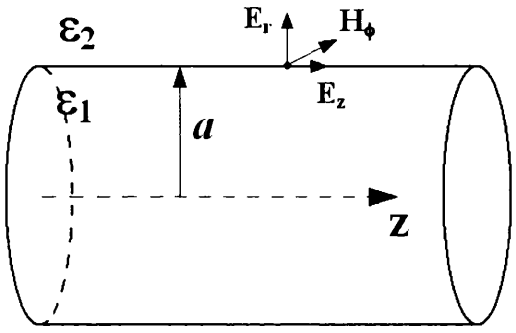

Fig. 6.5. Geometry of a metal cylinder waveguide.

Fig. 6.6 shows the field amplitudes in the outer vicinity of the silver surface as a function of radius a. The effective modal index, $n_{eff} = \beta/k_0$, is also plotted. Here, we have made energy normalization to the calculated eigen-mode. This means that the metal dissipation is ignored and the mode energy for different radius a is same.

As a approaches zero, the asymptotic behaviours of the field amplitudes and the modal index, which are linearly fitted in Fig. 6.6, are consistent with Eqn. (6.5). The parameters used in the calculations are: $\varepsilon_1 = -56+3i$, $\varepsilon_2 = 1$, and $\lambda_0 = 1.06$ μm.

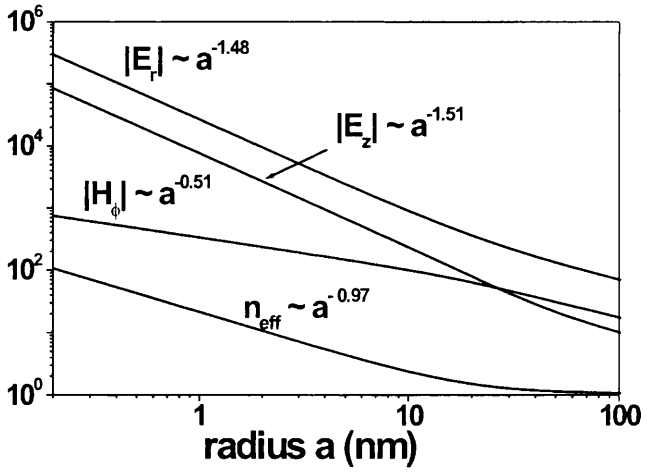

Fig. 6.6. Effective modal index and field amplitudes in the outer vicinity of the silver surface as a function of the radius a.

6.1.3 Scanning near-field optical microscopy (SNOM)

SPP superfocusing at a silver tip can find applications in scanning near-field optical microscopy. In order to explain how, a brief review of SNOM is given as follows:

The central goal of SNOM is to break the diffraction limit in spatial resolution and to allow optical imaging and spectroscopy on the nanometer scale [Betzig 91]. Most early works on SNOM are based on the transmission of light through a nanometer scale hole in an opaque screen [Betzig 92, Pohl 84, Lewis 84]. In an Al-coated fiber tip, this hole is formed at the apex, and the light transmission through the subwavelength aperture will be ultimately limited by mode cut-off [Sanchez 99].

With increasing interest and investigations in SPPs, exciting highly localized SPPs in a nano-scale tip nowadays becomes another solution to obtain high-resolution near-field optical information [Eckert 00, Milner 01, Sanchez 99]. This idea has been realized using external excitation with either direct diffraction-limited illumination (Fig. 6.7) [Adam 98] or prism total-internal-reflection illumination (Fig. 6.8) [Ashino 98]. A localized SPP, which brings high-resolution near-field information, is excited in the probe tip, and its energy is finally collected by a detector. The used tip can be coated or un-coated with metal.

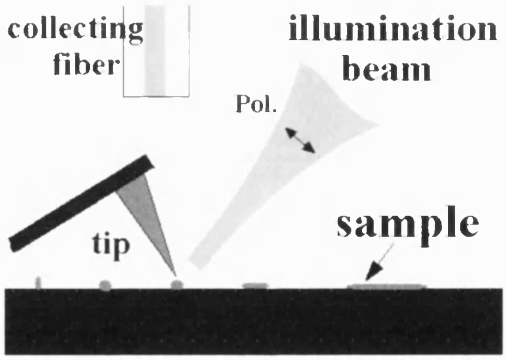

Fig. 6.7. SPP excitation in a direct illumination scheme.

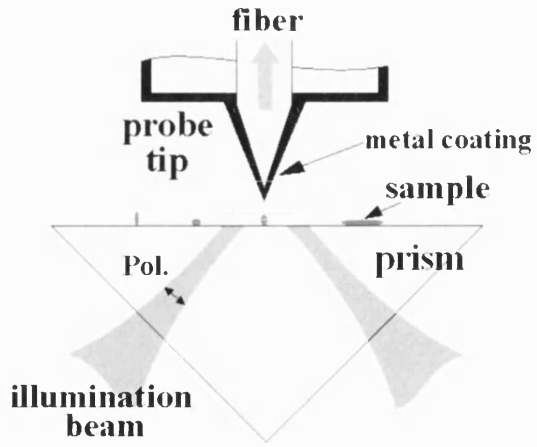

Fig. 6.8. SPP excitation in a prism total-internal-reflection scheme.

However, external excitation configurations have an intrinsic drawback: the parasitic far-field light that is not generated from the localized SPPs will mix with the near-field signal. Furthermore, in the direct illumination scheme, the SPP excitation is strongly dependent on the incident angle and the polarization; in the prism scheme, the sample has to be transparent. If SPPs can be excited internally from a fiber waveguide mode, all the above drawbacks are overcome. Moreover, sample heating during measurements will be minimized and the system complexity will be reduced.

Such an internal excitation of SPPs has been proposed in a finite thickness apertureless silver-coated fiber tip as schematically shown in Fig. 6.9 [Bouhelier 03, Vaccaro 03, Janunts 05]. In all these references, radially polarized modes, whose modal field symmetry leads to constructive interference and field enhancement at the apex, are suggested. The radially polarized modes can be efficiently generated in free space by mode conversion using, for example sectioned phase plates [Grosjean 05, Quabis 05].

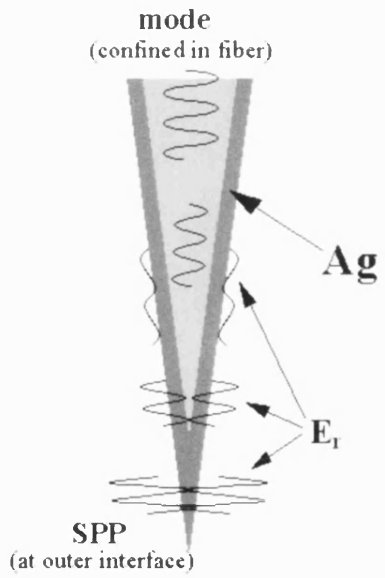

Fig. 6.9. Schematic of the mode evolution along an apertureless silver-coated fiber tip.

An analytical model was presented in reference [Janunts 05] to describe the coupling from a fiber waveguide mode to the SPP on the outer surface of a silver-coated fiber tip. However, these authors ignored the metal dissipation, which should be substantial, and assumed that the SPP modes confined on the inner and outer silver surfaces were nearly isolated. Therefore, the coupling between the outer and inner SPP modes was treated with a perturbation assumption. This over-simplified model is only suitable for a thick silver coating.

On the other hand, in references [Bouhelier 03, Vaccaro 03], authors studied SPP superfocusing using simulation methods (multiple multipole method [Hafner 90] and finite integration technique [Weiland 77], respectively). But, their studies are limited to the apex vicinity region and cannot describe the mode conversion occurring far away from the apex. This is also the shortcoming of reference [Babadjanyan 00], which has been mentioned in subsection 6.1.2.

In the following sections, we adopt both analytical and numerical methods to study this mode conversion process from fiber waveguide modes to the SPP mode on an apertureless silver-coated fiber tip. The evolution of the local modal indices as a function of the fiber radius is described, the condition that permits SPP excitation from fiber waveguide modes is discussed, and four influencing mechanisms during this mode conversion are quantitatively dealt with. Our results lead to an improved understanding of how an efficient energy transfer to a region far below the diffraction limit at the silver apex can be achieved.

6.2 Conversion of Fiber Waveguide Modes to SPP Modes

As shown in the lower part of Fig. 6.3, a cylindrical fiber coated with a silver layer has two metal-dielectric interfaces. The silica fiber radius is a, and the outer radius is $b = a + t$, where t is the silver thickness. We separate this double-interface waveguide into two single-interface waveguides as shown in Fig. 6.10. The silica waveguide (Fig. 6.10b) is buried in silver with radius of a, and the silver waveguide (Fig. 6.10c) is surrounded by air with radius of b. ε_1, ε_2, and ε_3 are respectively the dielectric permittivities of silica, silver and air.

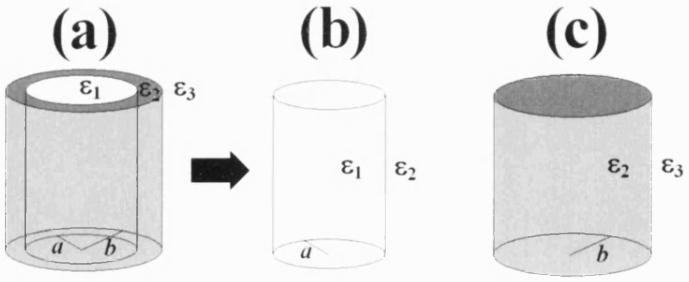

Fig. 6.10. Schematic of (a) silver-coated silica fiber, (b) silica waveguide buried in silver, and (c) silver waveguide in air.

Fig. 6.11 shows the effective modal indices of the radially polarized modes in the two single-interface waveguides: the upper curves are the modes of the buried silica waveguide (Fig. 6.10b). Many modes can be supported in this waveguide, and are labelled as 'inner-SPP mode' and 'TM_{0n} modes' respectively. The lower curve is the mode of the silver waveguide (Fig. 6.10c), and is labelled as 'outer-SPP mode'. Here, the TM_{0n} modes have similar field distributions with those TM_{0n} modes in the usual silica waveguide surrounded by air. As the external medium of the silica waveguide gradually changes from silver to air, the modal indices of the TM_{0n} modes change continuously. The inner- and outer-SPP modes, on the other hand, do not have counterparts in a usual silica waveguide. They are surface-guiding modes with most of the field distributed inside or outside the silver layer respectively.

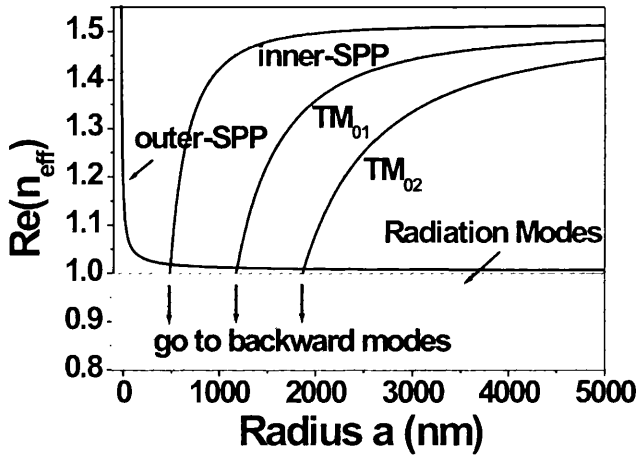

Fig. 6.11 Effective modal indices of the radially polarized modes in a silica waveguide surrounded by silver (upper curves) and a silver waveguide immersed in air (lower curve). The radii of these two waveguides are respectively a and $b = a + t$.

The methods used to calculate these eigen-modes have been introduced in section 2.2. In calculations, the following parameters are used: $\lambda_0 = 1.55$ μm, $t = 40$ nm, $\varepsilon_1 = 2.25$ (silica), $\varepsilon_2 = -103+8i$ (Ag), and $\varepsilon_3 = 1$ (air). In Fig. 6.11, the real parts of the effective modal indices are plotted as a function of the radius a. As the radius a decreases, all the modes in the buried silica waveguide (Fig. 6.10b) are cut off, and the mode energy is transferred to radiation or backward propagating modes. This is the situation occurring in an apertured Al-coated fiber tip. On the other hand, the

modal index of the outer-SPP mode in the silver waveguide (Fig. 6.10c) increases as a decreases. Mode Superfocusing occurs at the silver apex.

We next consider the eigen-modes of the double-interface waveguide shown in Fig. 6.10a. Fig. 6.12 plots the modal index variation with radius a for a 40 nm thick silver layer.

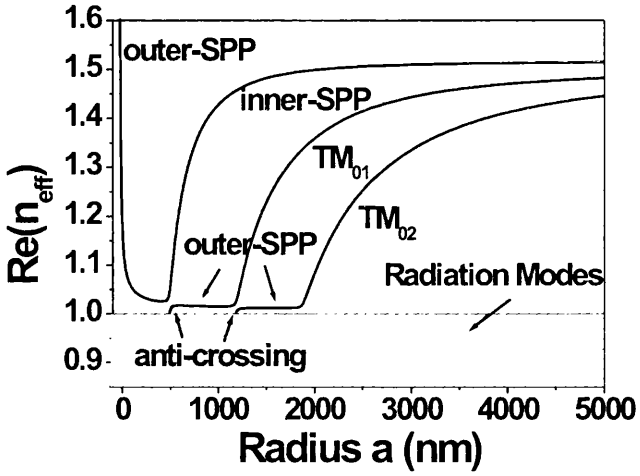

Fig. 6.12. Effective modal indices of a silver-coated fiber waveguide as a function of a. The silver thickness is 40 nm; all other parameters are same with those in Fig. 6.11.

Comparing with Figs. 6.11 and 6.12, a gap appears at each crossing point of the modal index curves. This phenomenon is called mode anti-crossing and is due to the mode splitting effect mentioned in subsection 6.1.1, which arises from the interaction between the modes of the buried silica waveguide (Fig. 6.10b) and those of the silver waveguide (Fig. 6.10c). Actually, this mode splitting effect happens in all radii a. But, when the two modes have equal modal index, the phase matching condition is satisfied, the interaction length of these two modes along the fiber increases, and the mode splitting effect is discernable.

Furthermore, due to the mode anti-crossing, the different parts in each mode branch show different physical significances. For a large a, the field distribution of the mode is similar to that in the buried silica waveguide (Fig. 6.10b); for a small a, the mode field distribution is similar to that in the silver waveguide (Fig. 6.10c). This property corresponds to the mode conversion from a fiber waveguide mode to the outside SPP mode.

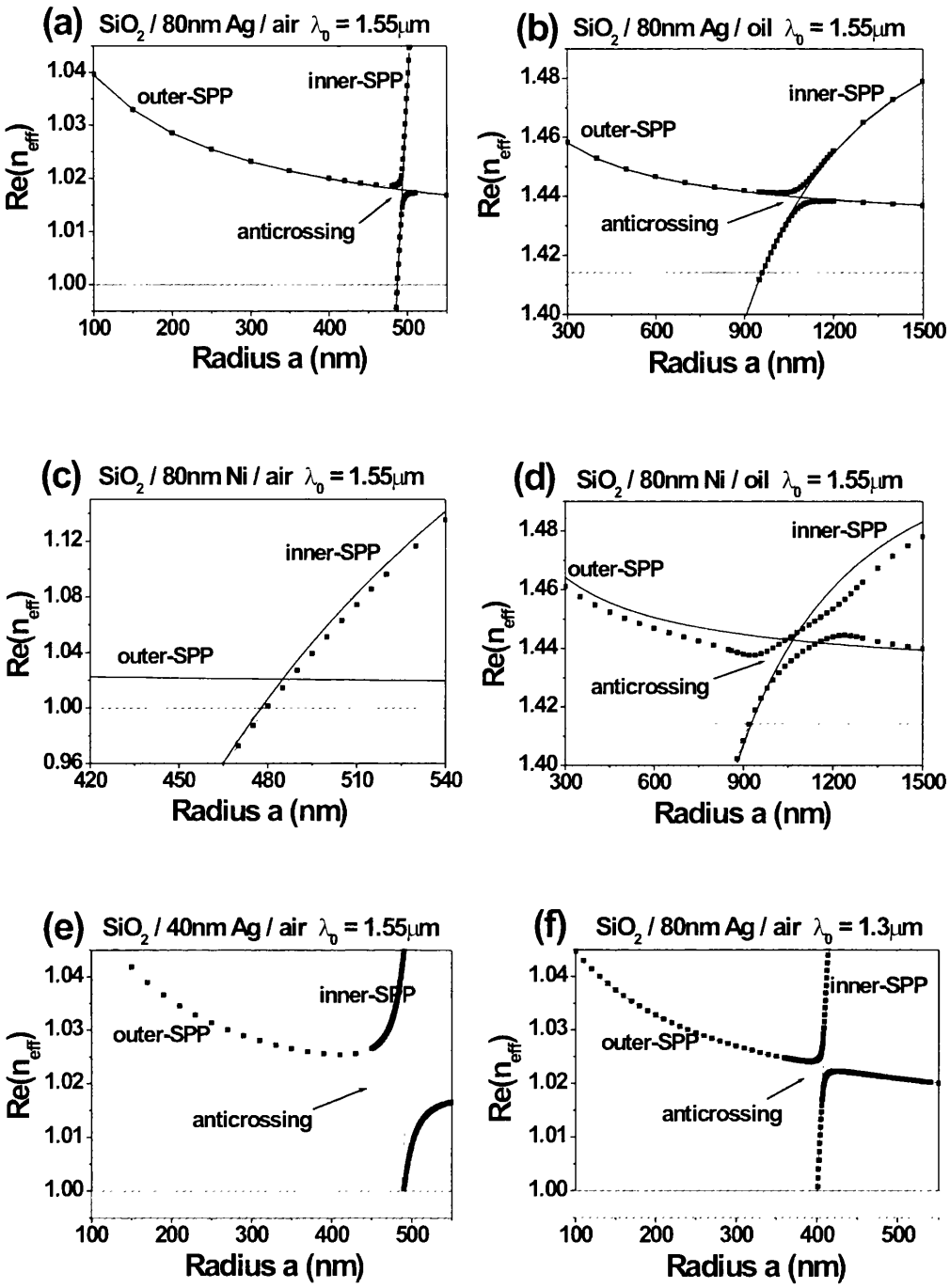

Fig. 6.13. Modal index curves as a function of the radius *a*. The detailed parameters for each picture are described in the text. As *a* decreases, the inner-SPP in (c) is cut off, whereas those in the other panels are converted to outer-SPPs.

In order to study the mode anti-crossing in more detail, calculations with different metals, external media, metal thickness and wavelength were made. The real parts of the modal indices are plotted as a function of radius *a*. The curves with symbols in Figs. 6.13a-d are the modal index evolutions of the silver- (Figs. 6.13a and

b) or nickel- (Figs. 6.13c and d) coated fibers surrounded by air (Figs. 6.13a and c) or oil (Figs. 6.13b and d). The modal indices of two single-interface waveguides (Figs. 6.10b and c) are also plotted as solid curves without symbols. The hatched areas indicate the radiation mode continua, which lie below the refractive indices of the external media. The dielectric constant of silica is 2.25, the surrounding medium is air ($\varepsilon = 1$) or oil ($\varepsilon = 2$), the metal thickness is 80 nm, and the wavelength is 1.55 μm. At this wavelength, the dielectric constants of silver and nickel are -103+8i and –34+46i respectively [Rakic 98]. In Figs. 6.13e and f, the metal and external media are silver and air respectively. In 6.13e, the silver thickness is decreased to 40 nm; in 6.13f, the wavelength is changed to 1.3 μm, so that the silver dielectric constant becomes -72+5i [Rakic 98].

The results in Fig. 6.13 illustrate that the mode anti-crossing is affected by the choice of metal, external medium, metal thickness, and wavelength. If nickel rather than silver is used as the coating, as shown in Fig. 6.13c, the strong absorption from the Ni layer weakens the interaction between the outer-SPP and inner-SPP modes. The structure can then be regarded as two isolated metal-dielectric interfaces, and the mode anti-crossing is suppressed. On the other hand, increasing the external medium index increases the penetration depth of the outer-SPP mode in the metal layer and enhances the field overlap and the interaction between the outer-SPP and inner-SPP modes. The suppressed mode anti-crossing in Fig. 6.13c is revived in Fig. 6.13d. For similar reasons, the metal thickness and the wavelength can also influence the mode anti-crossing. In Fig. 6.13e, decreasing the silver thickness makes the interaction between the outer-SPP and inner-SPP modes stronger. In Fig. 6.13f, changing the silver dielectric constant by altering the wavelength makes the anti-crossing gap wider.

Altogether, if the mode anti-crossing appears, the conversion from the mode confined inside a fiber waveguide to the SPP mode outside a silver coating can be realized in a finite-thickness silver-coated fiber by gradually decreasing the fiber radius. The excited outer-SPP mode superfocus as it approaches the apex. In the following two sections we will investigate this process.

6.3 Mode Propagation toward the silver apex

Fig. 6.14 shows a sketch of an apertureless finite-thickness silver-coated fiber tip. The inner and outer radii (a and b) are a function of the axial distance from the apex, z. The taper angle is $\alpha \approx |da/dz|$. Both the taper angle and the silver thickness, t, are constant in the range from $b(z)$ = 10 nm to $a(z) = a_0$. The dielectric constants of silica and air are 2.25 and 1 respectively.

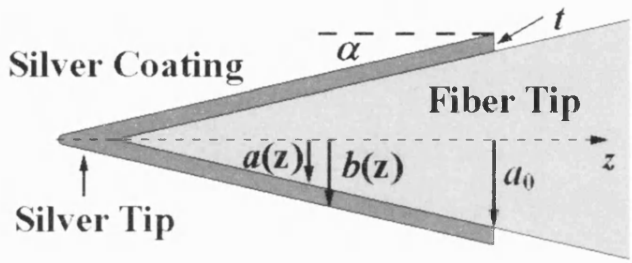

Fig. 6.14. Sketch of an apertureless finite-thickness silver-coated fiber tip.

6.3.1 Mode projection at the edge of the silver coating

As shown in Fig. 6.14, the silver layer is only coated in the region $a < a_0$. At the edge of this silver coating, the input field of the bare fiber is projected onto the eigen-mode basis of the silver-coated fiber (inner-SPP, TM_{0n} modes, and radiation).

Assuming the input field is the TM_{01} mode of the bare fiber, the input energy is mostly projected onto the inner-SPP and the TM_{01} modes of the silver-coated fiber. The mode projection efficiencies are dependent on the wavelength, the silver thickness, and the value of a_0. Fig. 6.15 shows the calculated mode projection efficiency P, which is obtained from the following expression [Snyder 83]:

$$P = \left| \frac{1}{2} \int_{A_\infty} [\hat{\mathbf{e}}_s(x,y) \times \hat{\mathbf{h}}_f(x,y)] \cdot \hat{\mathbf{a}}_z dA \right|^2 \tag{6.6}$$

where the subscripts f and s represent the mode of the bare fiber and the silver-coated fiber respectively, and the carets indicate the mode normalization.

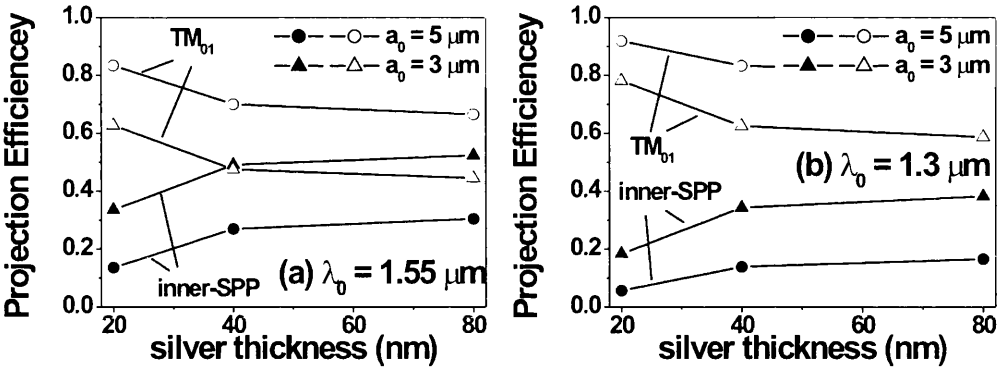

Fig. 6.15. Mode projection efficiencies from the input TM_{01} mode of the bare fiber to the inner-SPP (solid symbols) and TM_{01} (open symbols) modes of the silver-coated fiber. The wavelength is (a) 1.55 μm or (b) 1.3 μm. The edge of the silver coating is at the position of a_0 = 5 μm (circle symbols) or a_0 = 3 μm (triangle symbols).

Based on the calculations shown in Fig. 6.15, as the silver thickness and wavelength increase, more energy is projected onto the inner-SPP mode. Furthermore, moving the edge of the silver coating towards the apex also increases the projection efficiency onto the inner-SPP mode. Note that, here, we assume the input field to be a TM_{01} mode of the bare fiber.

To precisely determine the input field condition is very complicated and out of our investigations. Depending on the mode coupling occurring in the tapered bare fiber region before the silver coating, the realistic input field should be a superposition of the eigen-modes of the bare fiber. Therefore, more energy will be projected onto the high-order modes of the silver-coated fiber, which correspond to the lower mode branches in Fig. 6.12.

All the modes excited in the silver-coated fiber region interact with each other as they approach the apex. Some part of the mode energy will be transferred to the outer-SPP mode via those mode anti-crossings shown in Fig. 6.12. In the next subsection, we will discuss this mode coupling effect. The edge of the silver coating is assumed to be at a_0 = 5 μm, which is practical from a fabrication point of view.

6.3.2 Inter-modal coupling

In a non-uniform optical waveguide, due to the loss of translational symmetry, energy coupling occurs amongst different local modes, and the inter-modal coupling can be analytically treated with coupled-mode theory [Snyder 83].

Considering a non-absorbing silver-coated fiber tip, i.e. the imaginary part of the silver permittivity is assumed to zero, the transverse field distribution in each cross section of the fiber tip can be expanded in an orthonormal basis set of the local modes, $\hat{\mathbf{e}}_j$ and $\hat{\mathbf{h}}_j$ [Snyder 83]:

$$\mathbf{E}_t(x,y,z) = \sum_j b_j(z)\hat{\mathbf{e}}_{tj}[x,y,\beta_j(z)] \tag{6.7a}$$

$$\mathbf{H}_t(x,y,z) = \sum_j b_j(z)\hat{\mathbf{h}}_{tj}[x,y,\beta_j(z)] \tag{6.7b}$$

where the subscript t denotes the transverse component, $\beta_j(z)$ is the propagation constant, and $b_j(z)$ is the complex amplitude coefficient.

Before mode cut-off, the modal index difference between a forward guided mode and a radiation or backward mode is greater than that between two adjacent forward guided modes. The couplings from the forward guided mode to the radiation and backward modes are weaker than that between forward modes and so that can be neglected. The coupled equations can be expressed as:

$$db_j/dz = i\beta_j b_j + \sum_l C_{jl} b_l \tag{6.8}$$

where the coupling coefficient between forward modes l and j is

$$C_{jl}(z) = \frac{1}{4}\int_{A_\infty} [\hat{\mathbf{h}}_j^* \times \frac{\partial \hat{\mathbf{e}}_l}{\partial z} - \hat{\mathbf{e}}_j^* \times \frac{\partial \hat{\mathbf{h}}_l}{\partial z}] \cdot \mathbf{a}_z dA = \frac{\omega\varepsilon_0}{4(\beta_j - \beta_l)} \int_{A_\infty} \hat{\mathbf{e}}_j^* \cdot \hat{\mathbf{e}}_l \frac{\partial n^2}{\partial z} dA \tag{6.9}$$

However, the integral in (6.9) is ambiguous when applied to a silver-coated fiber tip. At the silver-dielectric interfaces, $\partial n^2/\partial z$ is a Dirac delta function, and the normal components of the electric fields are discontinuous. In appendix A1, we show how this problem can be solved by recasting Eqn. (6.9) in the form:

$$C_{jl} = \frac{\omega\varepsilon_0}{4(\beta_j - \beta_l)} \int_{A_\infty} [\hat{\mathbf{e}}_{zj}^* \cdot \hat{\mathbf{e}}_{zl} + \frac{\hat{\mathbf{d}}_{rj}^* \cdot \hat{\mathbf{d}}_{rl}}{\varepsilon^{(-)}\varepsilon^{(+)}}] \frac{\partial n^2}{\partial z} dA \tag{6.10}$$

where the subscripts z and r represent the longitudinal and radial components of the fields, $\mathbf{d}$ is the electric displacement, and $\varepsilon^{(-)}\varepsilon^{(+)}$ is the product of the permittivities on both sides of the silver surfaces. No ambiguity exists in Eqn. (6.10).

6.3.3 Metal dissipation

In order to include metal dissipation effect into the propagation equation (6.8), we sub-divide each micro-section into a non-absorbing silver-coated waveguide with a decreasing radius (Section A) and an absorbing silver-coated waveguide with a

constant radius (Section B) as shown in Fig. 6.16. Sections A and B have same lengths and are arranged alternately. Inter-modal coupling and metal dissipation are thus taken into account separately.

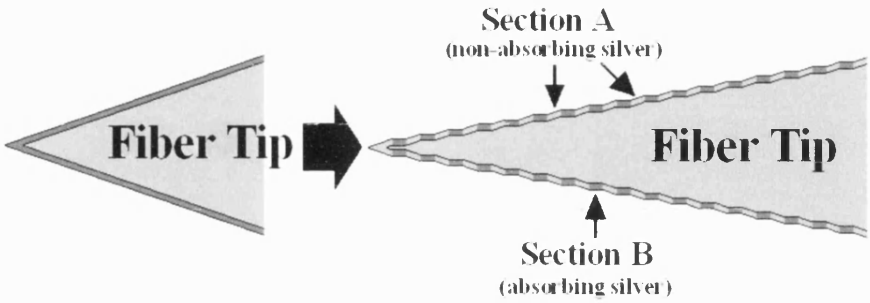

Fig. 6.16. Schematic of sectional sub-division process.

If we suppose that the effective indices of local modes are approximately continuous at each boundary between sections A and B, which is satisfied for a silver-coated fiber waveguide in the near-infrared based on our calculations, the section boundaries do not introduce significant scattering or reflection. We only need replace the propagation constant β in Eqn. (6.8) with a new value of $\beta^{(P)}$, which is the propagation constant of the local mode in the realistic absorbing silver-coated fiber and has a non-zero imaginary part. The new coupled-equations, which include both inter-modal coupling and metal dissipation, become:

$$db_j/dz = i\beta_j^{(P)} b_j + \sum_l C_{jl} b_l \tag{6.11}$$

Substituting the spatial distribution of dielectric constant

$$\varepsilon(r,z) = \varepsilon_{in} + (\varepsilon_M - \varepsilon_{in})\vartheta(r - a(z)) + (\varepsilon_{out} - \varepsilon_M)\vartheta(r - b(z)) \tag{6.12a}$$

$$\text{where } \vartheta(z) = \begin{cases} 0, & z < 0 \\ 1, & z > 0 \end{cases} \tag{6.12b}$$

into Eqn. (6.10), we obtain an expression for the coupling coefficient:

$$C_{jl}(z) = \frac{\pi\omega\varepsilon_0\alpha}{2(\beta_j - \beta_l)}$$
$$\{[\hat{\mathbf{e}}_{zj}^{\,*}(r=a)\cdot\hat{\mathbf{e}}_{zl}(r=a) + (\varepsilon_0^{\,2}\varepsilon_{in}\varepsilon_M)^{-1}\hat{\mathbf{d}}_{zj}^{\,*}(r=a)\cdot\hat{\mathbf{d}}_{zl}(r=a)](\varepsilon_M - \varepsilon_{in})a(z) \tag{6.13}$$
$$+[\hat{\mathbf{e}}_{zj}^{\,*}(r=b)\cdot\hat{\mathbf{e}}_{zl}(r=b) + (\varepsilon_0^{\,2}\varepsilon_{out}\varepsilon_M)^{-1}\hat{\mathbf{d}}_{zj}^{\,*}(r=b)\cdot\hat{\mathbf{d}}_{zl}(r=b)](\varepsilon_{out} - \varepsilon_M)b(z)\}$$

C_{jl} is inversely proportional to the propagation constant difference, β_j - β_l, and this relation explains why only coupling between adjacent forward modes are

considered in Eqn. (6.8). On the other hand, C_{jl} is proportional to the taper angle, α, but the length of the fiber tip is inversely proportional to the taper angle. The total coupling effect between two guided modes is therefore nearly independent to the taper angle.

At different wavelengths, Fig. 6.17 shows the modal energy evolution of the top mode branch in Fig. 6.12 with the fiber radius a. In calculations, we assume only inner-SPP mode of the silver-coated fiber is excited at the position of $a_0 = 5$ μm.

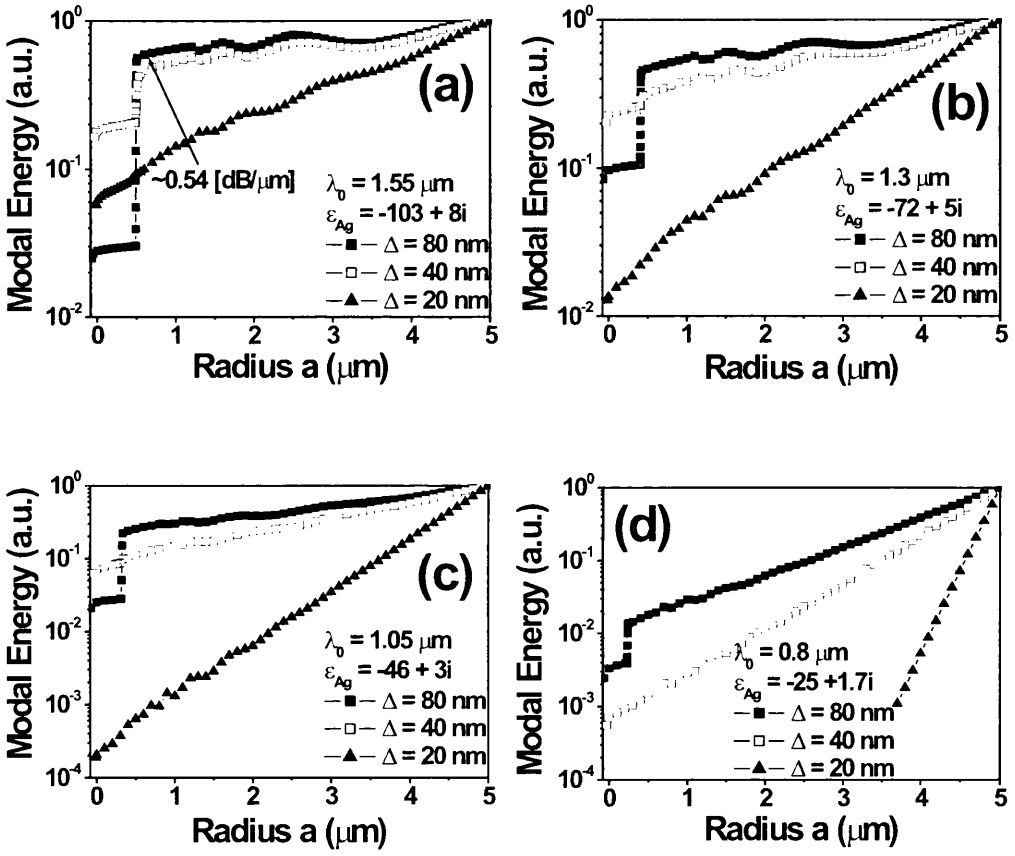

Fig. 6.17. Mode energies of the top branch in Fig. 6.12 as a function of radius a. Different wavelengths and silver thickness are used. The taper angle is $\alpha = 5°$. The input field is an inner-SPP mode of the silver-coated region.

In Fig. 6.17, the metal dissipation is manifest by the sloping evolution curves. As silver thickness decreases, metal dissipation leads to a greater propagation loss, since there is a greater fraction of field distributed in the silver layer of a thinner silver-coated fiber [Al-Bader 92, Berini 01]. At the same time, the inter-modal coupling results in an undulation in each evolution curve and a steep downward step near the anti-crossing. As the silver thickness decreases, the anti-crossing induced

mode branch gap broadens as shown in Figs. 6.13a and 6.13e, the adjacent two mode branches are separated more apart, the mode-coupling coefficient decreases according to Eqn. (6.13), and the inter-modal coupling near the anti-crossing becomes weak. That is displayed in Fig. 6.17 as a decreasing downward step in the energy evolution curves. The silver thickness is therefore an important factor in the optimization design process.

Another important parameter shown in Fig. 6.17 is the wavelength. As it decreases, the absolute value of the real part of the silver dielectric constant decreases with the consequence that the outer-SPP and inner-SPP modes penetrate the silver layer more deeply. This widens the anti-crossing induced mode branch gap as shown in Figs. 6.13a and 6.13f, separates the mode branches, and decreases the inter-modal coupling coefficient. On the other hand, due to the increase of the field overlap with the silver layer and the increase of the imaginary part of the silver permittivity, the metal dissipation increases.

In Fig. 6.18, we change the input field to be the TM_{01} mode in the bare fiber region, and this input field is projected at the edge of the silver coating (a_0 = 5 μm). The silver thickness is 80 nm, the wavelength is 1.55 μm, and the other parameters are the same as those in Fig. 6.17a. The mode energy evolution of the top (SPP) and second (TM_{01}) mode branches (see Fig. 6.12) are calculated taking into account the combined effects of mode projection, inter-modal coupling, and metal dissipation.

In the silver-coated region, a strong inter-modal coupling between the inner-SPP and TM_{01} modes occurs, and an intense undulation of the energy evolution curves (black and green curves) appears. At the anti-crossing position, this inter-modal coupling results in an upward step of the mode energy of the top mode branch. This is different with the situation in Fig. 6.17, where the mode energy evolution curve of the top mode branch steps downward, since the second (TM_{01}) mode branch is nearly empty due to the input field condition.

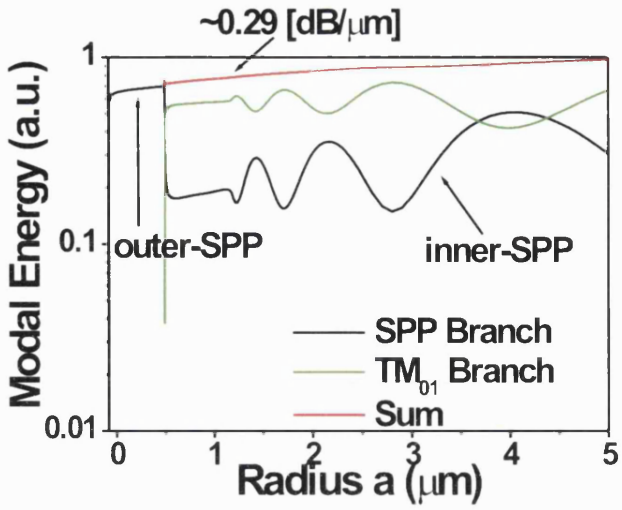

Fig. 6.18. Mode energies of the top branch (black curve) and the second branch (green curve) in Fig. 6.12 as a function of the radius *a*. The wavelength is 1.55 μm, the silver thickness is 80 nm, and the taper angle is 5°.

In Fig. 6.18, the red curve is the sum of the black and green curves. Its slope (~0.29 dB per 1 μm decrease in radius), which is proportional to the total metal dissipation, is less than that in Fig. 6.17a (~0.54 dB/μm): Because the only difference between these two cases is the input field condition, the discrepancy in the dissipation induced propagation loss is from the fact that the TM_{01} mode has less field overlap with the silver layer than the inner-SPP mode.

As mentioned in subsection 6.3.1, the real input field is more complicated than those adopted in Figs. 6.17 and 6.18 due to the mode coupling in the tapered bare fiber region before the silver-coated region. Nevertheless, the mechanisms of mode projection, inter-modal coupling, and metal dissipation are still valid. The input energy is distributed amongst the set of radially polarized eigen-modes of the silver-coated fiber by mode projection. The high-order modes suffer less metal dissipation during propagation due to the smaller field overlap with the silver layer. At the mode anti-crossings, the inter-modal couplings enhance due to the approaching of the modal indices, and the mode energy is transferred between different mode branches. If the energy is coupled from the lower mode branches to the upper mode branches, it will be delivered to the outer-SPP mode at the apex. If the mode energy is coupled into the lower mode branches, it will be removed from the fiber tip by radiation or reflection.

6.4 Radiation Coupling

When the fiber radius decreases below the mode cut-off, only the outer-SPP mode remains, so that the coupling amongst guided modes stops. The outer-SPP mode can only couple with radiation. This coupling effect is strongly dependent on the taper angle and will influence both transverse field confinement and propagation loss. On the other hand, this radiation coupling is hard to deal with analytically since radiation wave gradually leaves away from the waveguide as it propagates and the interaction length between the guided mode and the radiation is indeterminate. Hence, in the following sub-sections, we first give a crude treatment based on the criterion for an adiabatic propagation [Love 91], and then follow it by a more precise numerical study based on the finite integration technique [Weiland 77].

6.4.1 Adiabaticity criterion

For adiabatic propagation to be valid, a length-scale criterion, which is derived from simple physical principle, is required [Love 91]. This is that the local taper length-scale should be larger than the coupling length-scale of relevant modes.

The local taper length-scale, L_t, is the height of a right circular cone with base coincident with the local cross-section and apex angle equal to the local taper angle. The local coupling length-scale of two modes, L_b, is taken to be the beat length of these two modes. They can be expressed as [Love 91]:

$$L_t(z) \approx b(z)/\alpha \tag{6.14a}$$

$$L_b(z) = 2\pi/\mathrm{Re}[\beta_1(z) - \beta_2(z)] \tag{6.14b}$$

where $\beta_{1,2}$ are the propagation constants of the outer-SPP mode and the radiation, respectively.

Since the silver-coated fiber tip is surrounded by air, we assume the effective modal index of the radiation to be one. The adiabaticity criterion, $L_t > L_b$, leads to:

$$\alpha(z) < \alpha_0(z) = b(z) \cdot \mathrm{Re}[n_1(z) - 1]/\lambda_0 \tag{6.15}$$

where $\alpha_0(z)$ is the critical taper angle for adiabatic propagation and $n_1(z)$ is the effective index of the outer-SPP mode.

Such a simple criterion is not rigorous, but provides a useful guide to the fiber tip shape minimizing propagation loss due to power coupling out of the considered local mode and simultaneously being short enough for practical application.

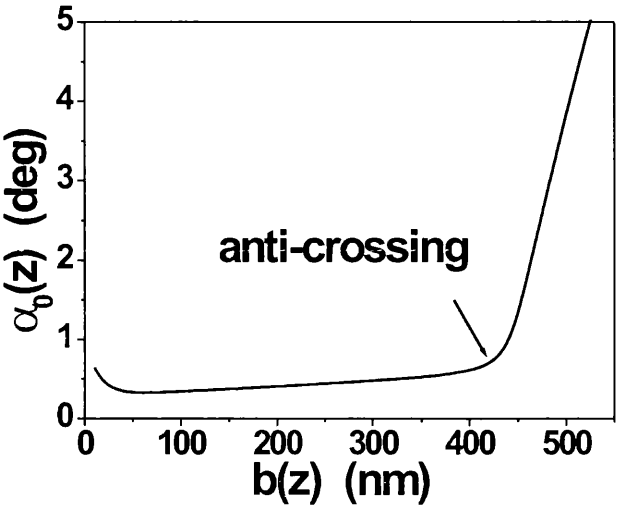

Fig. 6.19. Critical taper angle for adiabatic propagation as a function of outer fiber radius *b*. The silver thickness is 40 nm and the wavelength is 1.3 μm.

Fig. 6.19 shows the variation of $\alpha_0(z)$ with outer fiber radius *b*. It is clear that the adiabaticity requirement is easily satisfied before the anti-crossing point but difficult below. Therefore, radiation coupling mainly occurs in the vicinity region of the silver apex, where the outer-SPP mode is excited and the field widely distributes outside. This result is also approximately consistent with the behavior of the modal coupling coefficient (Eqn. (6.13)), which varies as $C \sim b^{-1/2}$ due to the fiber radius dependence of the propagation constant, $\beta \sim b^{-1}$, and the electric fields, $|E_{z,r}| \sim b^{-3/2}$ (see Eqn. 6.5 and Fig. 6.6) [Babadjanyan 00].

6.4.2 Numerical simulations

Using the finite integration technique described in chapter 2, numerical simulations were carried out on the structure shown in Fig. 6.20a (structure 1). A broadband radially polarized light pulse was injected from the right hand side and the fields at successive time steps were calculated. Before entering the fiber tip region, the input wave propagated through a 4 μm long uniform cylindrical waveguide, which helped to establish the true field profile of the outer-SPP mode. The silver thickness was 40 nm and the inner fiber radius *a* at the wider end was 140 nm. A silver hemi-sphere with radius of 10 nm was placed at the apex to avoid computational singularity. The frequency-dependent silver dielectric function in near-infrared (from 0.8 μm to

1.55 μm) was approximated by a Drude model, which shows a very good fit with the Lorentz-Drude model used in previous sections [Rakic 98]. The simulated fiber tip, which was below the anti-crossing, only sustains one guided mode (outer-SPP mode), so that, simulation results are dominated by radiation coupling and metal dissipation.

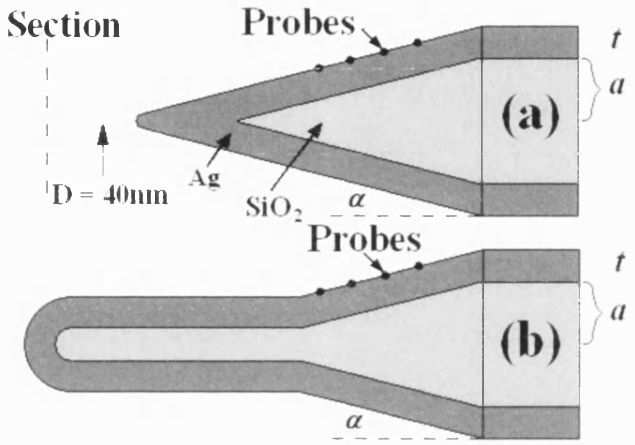

Fig. 6.20. Simulation structure 1 (a) and 2 (b) used in this subsection.

Fig. 6.21 shows the simulated distributions of the electric field amplitude for a silver-coated fiber tip. The results demonstrate that the field is strongly enhanced at the apex. The longitudinal fringes arise from interference between the forward wave and the backward reflection from the apex.

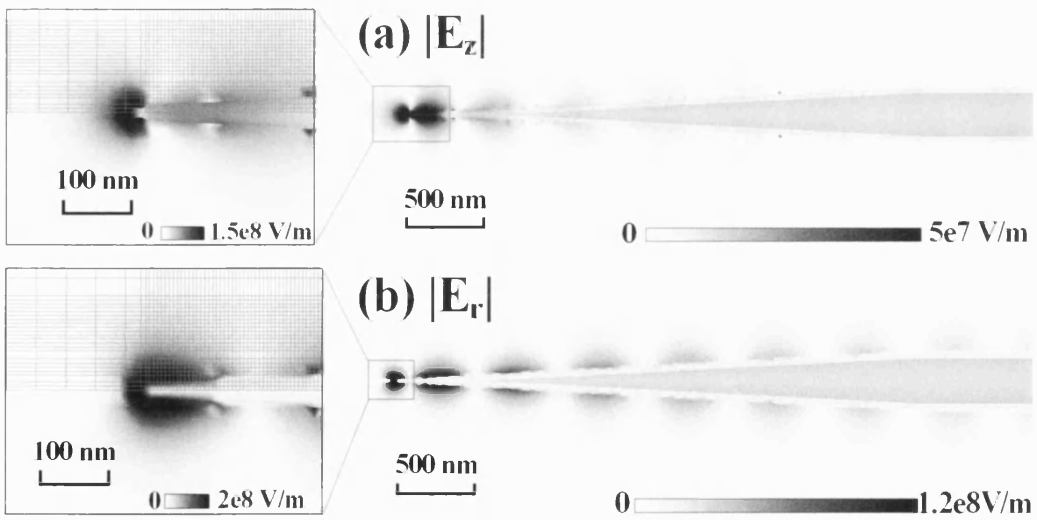

Fig. 6.21. Simulated distributions of (a) $|E_z|$ and (b) $|E_r|$ for $\lambda_0 \approx 1.3$ μm. The lattices in the magnified windows are the simulation meshes. The darker area corresponds to stronger field. The taper angle is 3° and the silver thickness is 40 nm.

The radial distributions of the longitudinal and radial electric field amplitudes behind the silver apex (see the plane section in Fig. 6.20a) are shown in Figs. 6.22a and 6.22c. As the taper angle increases from 3° to 15°, the enhanced radiation coupling causes the transverse field confinement to decrease.

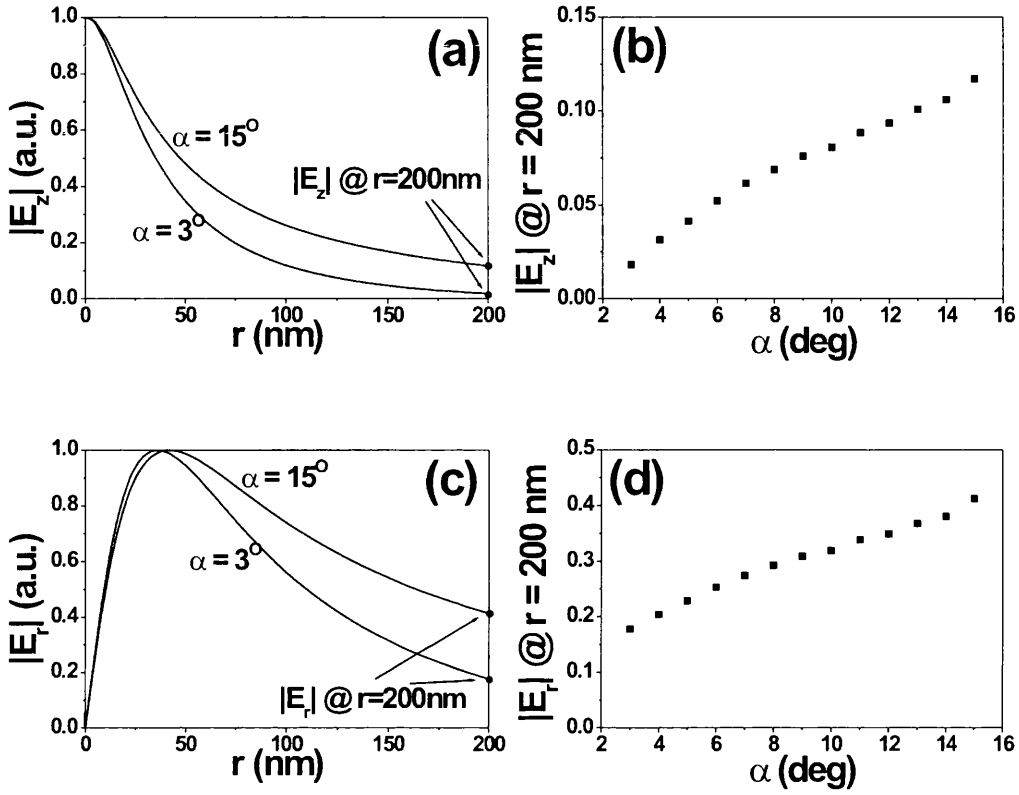

Fig. 6.22. Radial variation of (a) longitudinal and (c) radial electric field amplitudes over the cross section shown in Fig. 6.20a. The section is in air and 40 nm from the silver apex. The field amplitudes at r = 200 nm are shown in (b) and (d) as a function of taper angle.

In addition to the transverse field confinement, the radiation coupling also influences the propagation loss. In order to quantify this effect, we calculated the time variation of the magnetic fields at a series of probe points along the outer silver surface (see Fig. 6.20a) as the input pulse propagated along the fiber tip. Reflected pulses were removed from the data. After Fourier transformations, the frequency-domain amplitudes at $\lambda = 1.3$ μm were used to calculate the forward modal energies at each cross section at this wavelength. We assume that all non-radiative energy is confined in the local field of the outer-SPP mode, for which the field distribution, therefore the mode energy, is known if the magnetic field amplitude at the outer silver

surface is given. Because the outer-SPP mode has enhanced field amplitude at the silver surface, which is the signal, our approach can depress the error induced by the mixture of the radiation field in the recorded local field. The solid dots in Fig. 6.23a show this modal energy evolution as a function of the outer fiber radius b for a taper angle of 3°. The modal energy evolution calculated from Eqn. (6.11) is also shown by the solid curve. The latter ignores radiation coupling but takes into account metal dissipation. The close agreement of these two results shows the small influence of radiation coupling for this taper angle.

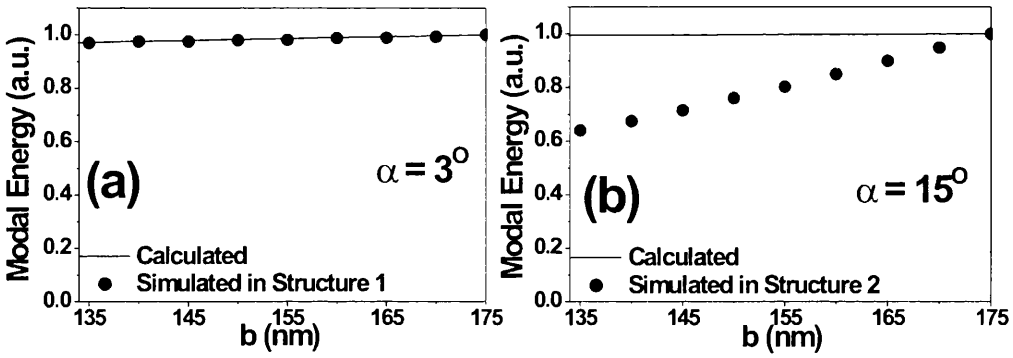

Fig. 6.23. Modal energy evolution as a function of the outer fiber radius, b, for a fiber tip with taper angles of (a) 3° and (b) 15°. The solid dots show results obtained from numerical simulations which include radiation coupling. The solid curves show calculations which include metal dissipation but ignore radiation. The silver thickness and the wavelength are 40 nm and 1.3 μm respectively.

For a large taper angle, the length of the fiber tip is reduced, so that the reflected pulse overlaps the forward pulse in time and is hard to be removed. In order to overcome this difficulty, we used another simulation structure as shown in Fig. 6.20b (structure 2). Here, an additional 1.5 μm long uniform waveguide is attached to the fiber tip to increase the delay of this reflected pulse. Although the discontinuity associated with this additional structure also introduces a reflection, by adjusting the attachment position to b = 80 nm, this reflection can be adjusted to an acceptable level. The solid dots in Fig. 6.23b show the simulated modal energy evolution for α = 15°. The large deviation from the analytical calculation (solid curve) is due to strong radiation coupling.

In Figs. 6.23, the difference between the simulated and calculated curves indicates the intensity of the radiation coupling in the region from b = 135 nm to b = 175 nm. Fig. 6.24 shows the variation of this radiation coupling intensity with the taper angle. Structure 1 in Fig. 6.20a is only suitable for calculation at small taper angles (solid dots); structure 2 in Fig. 6.20b suits for all taper angles (open dots), but will introduce some reflection artefacts at the discontinuity. The reflection artefact might explain the dip in the open dot curve. For small taper angles, this artificial effect disappears, and the simulated results from structures 1 and 2 are consistent. The fit line, which takes into account the results from structure 1 and 2, possibly shows the true enhancement of the radiation coupling loss with the taper angle.

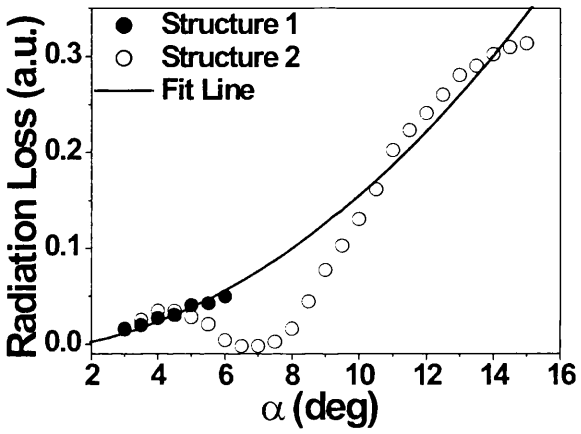

Fig. 6.24. Radiation coupling induced propagation loss as a function of the taper angle α. The solid dots are obtained from structure 1 (Fig. 6.20a), and the open dots from structure 2 (Fig. 6.20b). The silver thickness and the wavelength are 40 nm and 1.3 μm respectively.

6.5 Discussion and Conclusions

Superfocusing of the SPP mode at a silver apex has applications in scanning near-field optical microscopy, where the field confinement of the SPPs is exploited to obtain deep sub-wavelength spatial resolution. This chapter has described theoretical investigations of the mode conversion process from radially polarised fiber waveguide modes to the outer-SPP mode of an apertureless silver-coated optical fiber tip. The results show that SPP superfocusing can be efficiently excited from optical fiber modes. This internal excitation has many advantages over conventional external

excitation. For example, a higher signal-to-noise ratio and a simpler experimental geometry can be achieved.

The mode conversion from fiber waveguide modes to SPP depends on the mode anti-crossing phenomenon. Without it, mode cut-off will occur, and mode energy will be removed by radiation or reflection. In order to efficiently produce this mode conversion, the mechanisms of mode projection, inter-modal coupling, metal dissipation, and radiation coupling need to be optimized. Quantitative calculations for the first three are carried out analytically, whilst the last is performed numerically.

The structure parameters of the silver-coated fiber tip, such as the taper angle, the wavelength, the silver thickness, and the position of the edge of the silver coating, enter the different optimisation process in the following ways:

For mode projection, the wavelength, the silver thickness, and the edge of the silver coating are relevant. A large wavelength, a thick silver thickness, and close proximity of the silver coating edge to the apex allow more energy to be projected onto lower-order modes. The mode projection also depends on the input field condition. Energy projected onto high-order modes suffers less metal dissipation during the subsequent propagation toward the silver apex. However, the energy of the high-order modes has to be coupled to the outside SPP mode via the mode anti-crossing.

For inter-modal coupling, the silver thickness and the wavelength are important. Decreasing the silver thickness or the wavelength increases the mode interaction and results in a widened gap between adjacent mode branches, which reduces the waveguide non-uniformity-induced inter-modal coupling. On the other hand, although a big taper angle brings a large inter-modal coupling coefficient, this effect is partly compensated by the shortening of the fiber tip length with the increase in taper angle. The influence of the inter-modal coupling to the mode conversion is complicated and depends on the input field condition, the coupling intensity, and the fiber tip length.

Regarding metal dissipation, the effects of the wavelength, the silver thickness, and the taper angle are important. A short wavelength causes an enhanced field penetration into the silver layer and an increase of the imaginary part of the silver dielectric constant. A thin silver layer leads to a large field overlap with the silver layer. A small taper angle results in an increase in the fiber tip length. All these factors will increase metal dissipation and are harmful to the mode conversion.

For radiation coupling, only the taper angle is of importance. As it increases the transverse field confinement at the silver apex and the radiation induced propagation loss become worse, so that radiation coupling is harmful to the mode conversion.

Table 6.1 summarises these optimisation mechanisms and how these are influenced by the structure parameters of a silver-coated fiber tip. The symbols + and – respectively represent the positive and negative relations between them. That is to say an increase of one structure parameter causes an increase (+) or decrease (-) of one mechanism. The symbol X indicates a negligible effect.

Parameter / **Mechanism**	**Taper Angle**	**Wavelength**	**Silver Thickness**	**Edge of Silver Coating**
Mode Projection (to lower order modes)	X	+	+	–
Inter-modal Coupling	X	+	+	X
Metal Dissipation	–	–	–	X
Radiation Coupling	+	X	X	X

Table 6.1. Relation between the mode conversion mechanisms and the structure parameters for a silver-coated fiber tip.

Based on our studies, an improved understanding about the internal excitation and superfocusing of SPP on an apertureless silver-coated fiber tip is provided. The investigation shows how an efficient energy transfer to a region far below diffraction limit at a sliver apex can be achieved.

Chapter 7

Summary and Future Work

7.1. Summary

This thesis describes our explorations in two categories of tapered optical fiber devices: longitudinally structured fiber tapers and apertureless silver-coated fiber tips. For the former, fabrication and spectral characterisation were carried out; for the latter, theoretical investigations were performed.

7.1.1 Longitudinally structured fiber tapers

In order to produce longitudinal structures in fiber tapers, planar processing techniques have been applied on the curved surface of a micron-scale fiber taper.

Au Bragg grating fiber tapers

Using interference lithography and metal deposition, an Au Bragg grating was created on fiber tapers. This surface grating overlaps with the evanescent field of the guided modes and causes strong mode coupling due to the large permittivity contrast between gold and environment. The spectral characteristics were measured and treated theoretically. The backward couplings to guided- and radiation modes and their variations with the refractive index of the external medium were studied. A transmission dip occurring at the edge of the radiation coupling continuum displays a high sensitivity to the external medium index, and an application to refractometric sensing has been presented.

Corrugation Bragg grating fiber tapers

Using interference lithography and reactive ion etching, a surface corrugation Bragg grating was produced on the waist of a fiber taper. The grating taper waist and the adiabatic taper transition compose a reflection-based optical fiber filter. They respectively function as the functional part and the unwanted mode remover of the device. By controlling the diameter profile of the fiber taper, we have presented a

novel way to manipulate the reflection spectrum. This method of using a constant grating period and a variable taper diameter is more straightforward and easier than writing a variable-period grating.

Long period grating fiber tapers

Using contact optical lithography and HF etching, radially symmetric long period grating grooves were written on the surface of fiber tapers. The big fabrication feature size of this technique is limited by serious diffraction problems when applying contact optical lithography to fiber tapers. As an optical fiber device, the long period grating produced with our method has the merit of small polarization dependence and can be used as a wide band filter.

FIB milled micro-cavity structured fiber tapers

Using focused-ion-beam milling, a highly resolved and deeply trenched micro-cavity structure was directly produced in fiber tapers. Preliminary research on simulation and fabrication appears promising, and the device can be used as a band pass filter. The drawback of this fiber taper device is its mechanical fragility, so that further fabrication efforts are required to produce a workable device.

7.1.2 Apertureless silver-coated fiber tips

In an apertureless silver-coated fiber tip, radially polarised fiber waveguide modes can be converted to the outer-SPP mode. Superfocusing of the SPP mode at the silver apex has applications in scanning near-field optical microscopy, and the internal excitation of the SPP mode surpasses conventional external excitation with a higher signal-to-noise ratio and a simpler experimental configuration. Our theoretical investigations for this mode conversion indicate that this process depends on the mode anti-crossing and is affected by the mechanisms of mode projection, inter-modal coupling, metal dissipation, and radiation coupling. In order to make this mode conversion efficient, the structure parameters, such as the taper angle, the wavelength, the silver thickness, and the position of the edge of the silver coating, need to be optimised. Based on our quantitative calculations and simulations, a comprehensive understanding about this mode conversion process has been obtained.

7.2. Future work directions

The research presented in this thesis can be extended in many directions.

The implementations of longitudinally structured fiber tapers in various applications are straightforward. For example, the long period grating fiber tapers can be used as a wideband filter in gain equalization of fiber amplifiers [Feced 99].

The application of surface corrugation Bragg grating fiber tapers in evanescent coupling [Barclay 04] is also promising. The grating can be exploited to compensate the propagation constant mismatch between the modes in a fiber taper and in a ridge waveguide.

The further exploration of the Au Bragg grating fiber tapers will focus on the permittivity property of the grating material. In some cases, a narrow band pass filter spectrum, not a band rejection spectrum, can be fulfilled.

The future work directions of apertureless silver-coated fiber tips include more detailed optimisation calculations with regards to the structure parameters, the fabrication of silver-coated fiber tips and the setting-up of a measurement configuration.

Appendix

A1 Deduction of equation (6.10)

Here, we present the derivation of equation (6.10), which is deduced from the ambiguous equation (6.9).

Firstly, we introduce the positive-limiting differential definition as follows:

$$\frac{\partial^{(+)} f(z)}{\partial z} = \lim_{\Delta z \to 0+} \frac{f(z+\Delta z) - f(z)}{\Delta z} \tag{A1.1}$$

where the function $f(z)$ could be discontinuous, but, has to be finite.

Using this positive-limiting differential definition, we obtain,

$$\begin{cases} \dfrac{\partial^{(+)}[n^2(z)\hat{\mathbf{e}}(z)]}{\partial z} = n^2(z)\dfrac{\partial^{(+)}\hat{\mathbf{e}}(z)}{\partial z} + \dfrac{\partial^{(+)} n^2(z)}{\partial z}\hat{\mathbf{e}}(z+) \\ \dfrac{\partial^{(+)}[\beta(z)\mathbf{a}_z \times \hat{\mathbf{e}}(z)]}{\partial z} = \beta(z)\mathbf{a}_z \times \dfrac{\partial^{(+)}\hat{\mathbf{e}}(z)}{\partial z} + \dfrac{\partial^{(+)}\beta(z)}{\partial z}[\mathbf{a}_z \times \hat{\mathbf{e}}(z+)] \\ \dfrac{\partial^{(+)}[\beta(z)\mathbf{a}_z \times \hat{\mathbf{h}}(z)]}{\partial z} = \beta(z)\mathbf{a}_z \times \dfrac{\partial^{(+)}\hat{\mathbf{h}}(z)}{\partial z} + \dfrac{\partial^{(+)}\beta(z)}{\partial z}[\mathbf{a}_z \times \hat{\mathbf{h}}(z+)] \end{cases} \tag{A1.2a}$$

where,

$$\hat{\mathbf{e}}(z+) = \lim_{\Delta z \to 0+} \hat{\mathbf{e}}(z+\Delta z), \qquad \hat{\mathbf{h}}(z+) = \lim_{\Delta z \to 0+} \hat{\mathbf{h}}(z+\Delta z) \tag{A1.2b}$$

Applying Maxwell equations to the j^{th} and l^{th} local modes of a cylindrical waveguide,

$$i\omega\mu_0 \hat{\mathbf{h}}_j(z) = \nabla_t \times \hat{\mathbf{e}}_j(z) + i\beta_j(z)\mathbf{a}_z \times \hat{\mathbf{e}}_j(z) \tag{A1.3a}$$

$$-i\omega\varepsilon_0 n^2(\mathbf{r})\hat{\mathbf{e}}_j(z) = \nabla_t \times \hat{\mathbf{h}}_j(z) + i\beta_j(z)\mathbf{a}_z \times \hat{\mathbf{h}}_j(z) \tag{A1.3b}$$

$$i\omega\mu_0 \hat{\mathbf{h}}_l(z) = \nabla_t \times \hat{\mathbf{e}}_l(z) + i\beta_l(z)\mathbf{a}_z \times \hat{\mathbf{e}}_l(z) \tag{A1.3c}$$

$$-i\omega\varepsilon_0 n^2(\mathbf{r})\hat{\mathbf{e}}_l(z) = \nabla_t \times \hat{\mathbf{h}}_l(z) + i\beta_l(z)\mathbf{a}_z \times \hat{\mathbf{h}}_l(z) \tag{A1.3d}$$

where the subscripts t and z represent the transverse and longitudinal components. The dielectric constant, $n^2(\mathbf{r})$, is a real function due to our assumption of a non-absorbing waveguide.

Then, making operations of

$$(A1.3a)^* \cdot \frac{\partial^{(+)}\hat{\mathbf{h}}_l}{\partial z} + (A1.3b)^* \cdot \frac{\partial^{(+)}\hat{\mathbf{e}}_l}{\partial z} + \frac{\partial^{(+)}(A1.3c)}{\partial z} \cdot \hat{\mathbf{h}}_j{}^* + \frac{\partial^{(+)}(A1.3d)}{\partial z} \cdot \hat{\mathbf{e}}_j{}^*,$$

the following equation is obtained:

$$\begin{aligned} &\omega\varepsilon_0 n^2(\mathbf{r})'\hat{\mathbf{e}}_j{}^* \cdot \hat{\mathbf{e}}_l(z+) = -i\nabla_t \cdot (\hat{\mathbf{e}}_j{}^* \times \hat{\mathbf{h}}_l' + \hat{\mathbf{e}}_l' \times \hat{\mathbf{h}}_j{}^*) \\ &+ \beta_l' \mathbf{a}_z \cdot [\hat{\mathbf{e}}_l(z+) \times \hat{\mathbf{h}}_j{}^*(z+) - \hat{\mathbf{h}}_l \times \hat{\mathbf{e}}_j{}^*] + (\beta_l - \beta_j)\mathbf{a}_z \cdot [\hat{\mathbf{e}}_j{}^* \times \hat{\mathbf{h}}_l' - \hat{\mathbf{h}}_j{}^* \times \hat{\mathbf{e}}_l'] \end{aligned} \tag{A1.4}$$

where the asterisk represent the complex conjugation, and the positive-limiting differential definition (A1.1) and the continuous boundary conditions of magnetic field, $\hat{\mathbf{h}}(z+) = \hat{\mathbf{h}}(z)$, are used.

Integrating (A1.4) in the infinite cross section area and applying the two-dimensional form of the divergence theorem, we obtain

$$\begin{aligned} C_{jl}{}^{(+)}(z) &= \frac{1}{4}\int_{A_\infty} [\hat{\mathbf{h}}_j{}^* \times \frac{\partial^{(+)}\hat{\mathbf{e}}_l}{\partial z} - \hat{\mathbf{e}}_j{}^* \times \frac{\partial^{(+)}\hat{\mathbf{h}}_l}{\partial z}] \cdot \mathbf{a}_z dA \\ &= \frac{\omega\varepsilon_0}{4(\beta_j - \beta_l)} \int_{A_\infty} \hat{\mathbf{e}}_j{}^* \cdot \hat{\mathbf{e}}_l(z+) \frac{\partial^{(+)} n^2}{\partial z} dA \end{aligned} \tag{A1.5}$$

Here, the ambiguity in the coupling coefficient $C_{jl}{}^{(+)}$ has disappeared.

Using the similar way, a coupling coefficient $C_{jl}{}^{(-)}$ can also be derived based on a negative-limiting differential definition analogous to Eqn. (A1.1). The result is,

$$\begin{aligned} C_{jl}{}^{(-)}(z) &= \frac{1}{4}\int_{A_\infty} [\hat{\mathbf{h}}_j{}^* \times \frac{\partial^{(-)}\hat{\mathbf{e}}_l}{\partial z} - \hat{\mathbf{e}}_j{}^* \times \frac{\partial^{(-)}\hat{\mathbf{h}}_l}{\partial z}] \cdot \mathbf{a}_z dA \\ &= \frac{\omega\varepsilon_0}{4(\beta_j - \beta_l)} \int_{A_\infty} \hat{\mathbf{e}}_j{}^* \cdot \hat{\mathbf{e}}_l(z-) \frac{\partial^{(-)} n^2}{\partial z} dA \end{aligned} \tag{A1.6}$$

When applied to a silver-coated fiber tip, the results of (A1.5) and (A1.6) are identical. The coupling coefficient Eqn. (6.9) can be alternatively expressed as:

$$\begin{aligned} C_{jl}(z) &= \frac{1}{4}\int_{A_\infty} [\hat{\mathbf{h}}_j{}^* \times \frac{\partial\hat{\mathbf{e}}_l}{\partial z} - \hat{\mathbf{e}}_j{}^* \times \frac{\partial\hat{\mathbf{h}}_l}{\partial z}] \cdot \mathbf{a}_z dA = C_{jl}{}^{(+)}(z) = C_{jl}{}^{(-)}(z) \\ &= \frac{\omega\varepsilon_0}{4(\beta_j - \beta_l)} \int_{A_\infty} [\hat{\mathbf{e}}_{zj}{}^* \cdot \hat{\mathbf{e}}_{zl} + \frac{\hat{\mathbf{d}}_{rj}{}^* \cdot \hat{\mathbf{d}}_{rl}}{\varepsilon^{(-)}\varepsilon^{(+)}}] \frac{\partial n^2}{\partial z} dA \end{aligned} \tag{A1.7}$$

where the subscripts z and r represent the longitudinal and radial components of the fields, $\mathbf{d}$ is the electric displacement, and $\varepsilon^{(-)} \cdot \varepsilon^{(+)}$ is the product of the permittivities on both sides of the silver-dielectric interfaces. The second integral in (A1.7) has no ambiguous term like Eqn. (6.9).

(A1.7) is the form of Eqn. (6.10). In deduction, the only important assumption we use is that the waveguide is non-absorbing.

A2 Multi-wavelength transmission photonic crystal microcavity filters in SOI ridge waveguides

This work was executed in collaboration with Mr. Xiaohua Shi and Dr. Duncan Allsopp of the Department of Electronic and Electrical Engineering of University of Bath. Our contributions focused on the theoretical modelling and parts of the measurement.

A2.1 Introduction

During the last two decades, photonic crystal (PhC) structures have received considerable attentions in the optics community [Yablonovitch 87, Joannopoulos 95, Russell 03a]. The periodic variations of the dielectric constant of a PhC give rise to novel optical properties that depend on the period, the dielectric contrast and the geometry of each period [Russell 03b]. The resulting periodic lattices can be regarded as a kind of special optical material, in which the dispersion characteristics of the eigen Bloch waves can be revealed by wave-vector diagrams [Russell 96].

Resonant microcavities have been widely used as a vehicle for demonstrating some of the key properties of PhCs [Peyrade 02]. The resonant wavelengths of a microcavity are those obeying the standing wave condition, set by the width of the central layer sandwiched between the PhC reflectors, leaving little or no scope for engineering the positions of the transmission peaks, i.e. not only the spacing but also the offset. Recently, Hyun-Yong Lee et al demonstrated a novel multi-resonance microcavity [Lee 05]. The structure comprised multiple layers of Si-SiO_2 with the homogeneous in-cavity material replaced by a Si-SiO_2 one-dimensional (1D) PhC of different period to that of the reflectors. The transmission and reflection can be calculated using the transfer matrix method (TMM).

However, waveguide structures are needed for many applications in photonics. The TMM is not rigorously applicable in slab waveguide structures, and an alternative approach is required. In this section, we present an investigation of multi-wavelength transmission in 1D PhC microcavities formed in ridge waveguides. First, an intuitive analytical model of multi-wavelength transmission in a 1D PhC microcavity structure is developed. This is based on a wave-vector diagram and provides a simple method

for rapid design optimisation. Then, this model is applied to both multi-layer stack structures as well as 1D PhC slab waveguides. The results are compared with those of the TMM approach in the multi-layer stack structure and of a rigorous method in the photonic crystal slab structure [Gerace 04]. Finally, this model is applied to the realisation of a multi-wavelength transmission microcavity formed in a SOI ridge waveguide. The measured spectral response of this novel filter is compared with the wavelengths predicted by the analytic model, to demonstrate its validity.

A2.2 Theory

Fig. A2.1 shows the different types of 1D PhC microcavity considered in the literature (see for example, [Lee 05, Gerace 04]). Fig. A2.1a schematically shows a multiple layer 1D PhC microcavity in which the periodicity varies. The two reflectors at both ends and the central part of the cavity consist of pairs of layers of high refractive index contrast, with period Λ_A in the reflectors and Λ_B in the central section ($\Lambda_A \neq \Lambda_B$). In our work, the layer pairs were taken to be silicon (dielectric constant ε_{Si} = 12) and air (ε_{air} = 1) [McCaulley 94].

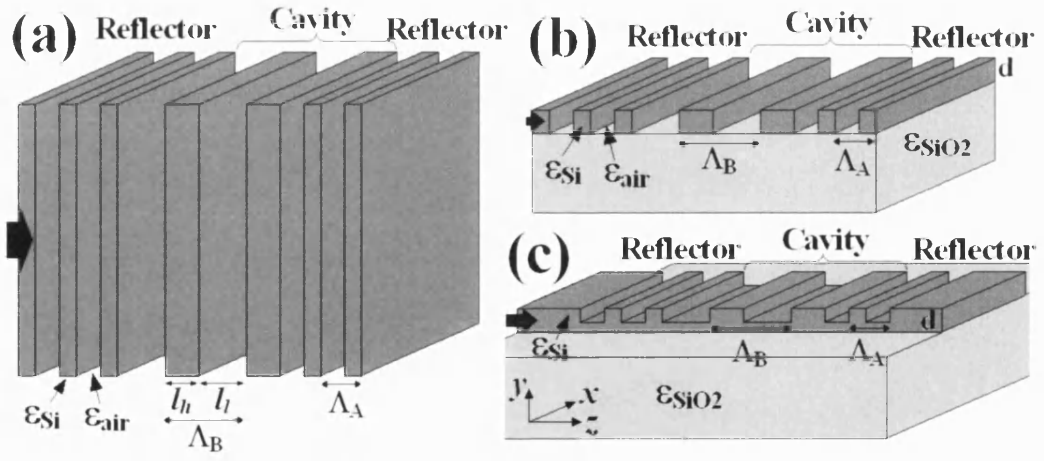

Fig. A2.1. Schematic of 1D PhC micro-cavity structures. (a) Multi-layer Stacks. (b) Photonic Crystal Slabs. (c) Planar Ridge Waveguide on SOI Wafers.

Figs. A2.1b and c show the equivalent structure formed in a planar slab waveguide and a ridge waveguide. Since a ridge waveguide forms a convenient means of coupling light in and out of the device, the structure shown in Fig. A2.1c is the most important regarding to applications. However, the field confinement in the *x*-direction associated with the ridge waveguide width introduces a complication to the analysis. For example, in the structure described in the next subsection, the air/Si

waveguide ridge is wide enough to support several modes. For the simplification of the treatment, we just consider the fundamental mode in the x-direction, so that the field confinement is insignificant compared with the confinement in the out-of-plane y-direction associated with the slab thickness. In the theory that follows, the PhC structure is treated like that in Fig. A2.1b, where the lateral feature is assumed to be infinite $|x| \rightarrow \infty$.

One other difference between the structures shown in Figs. A2.1b and A2.1c is that the air gaps in the latter do not extend through the entire thickness of the Si layer. Incomplete etching of the Si layer helps to control the radiation loss that enhances for a large air fraction in air/Si PhCs [Gerace 04]. On the other hand, the remaining Si at the bottom of the air gaps should be thin enough to ensure little effect on the design of a practical multi-wavelength filter.

The resonant wavelengths are the key factor in designing a multi-wavelength microcavity filter of the type shown in Fig. A2.1. For all three structures the resonant condition is given by:

$$2\pi s = 2(L + L_p)k_s + \pi = 4\pi(L + L_p)n_s/\lambda_s + \pi \qquad s = 1, 2, 3 \ldots \qquad \text{(A2.1)}$$

In Eqn. (A2.1), k_s, λ_s and n_s are respectively the propagation constant, the free space wavelength and the effective modal index of the s^{th} resonant mode, L is the cavity length, L_p is the penetration depth of the resonant mode into the two reflectors. With a PhC replacing the usual homogeneous material in the central section of the cavity, a resonant mode comprises two counter-propagating Bloch waves. One originates from reflections at the interfaces as light passes from high index Si layers to low index air layers (leftward propagating Bloch modes in Fig. A2.1a). The other originates from reflections at the interfaces as light passes from low index air layers to high index Si layers (rightward propagating Bloch modes in Fig. A2.1a). The factor π added to the right-hand side of Eqn. (A2.1) accounts for the phase change associated with the different types of reflection.

The use of Bloch wave vector diagrams [Russell 96] reveals the advantage of using a PhC in the central section of the cavity. Fig. A2.2 shows the Bloch wave-vector diagrams for the two 1D periodic stacks Λ_A (dotted lines) and Λ_B (solid lines) and $\Lambda_B = 2\Lambda_A$. Both sets of bi-layers satisfy the equal optical length condition, $n_h l_h = n_l l_l$, where $n_{h,l}$ and $l_{h,l}$ are respectively the refractive index and thickness of the high (low) index layers. The Bloch wave-vector diagrams are calculated using the plane-

wave expansion method [Joannopoulos 95]. Fig. A2.2 also shows by vertical dashed lines the Bloch wave vectors (denoted k_{B4}, k_{B5} and k_{B6}) of the 4th, 5th, and 6th order resonant modes calculated from Eqn. (A2.1) neglecting the penetration depth (i.e. with $L_p = 0$).

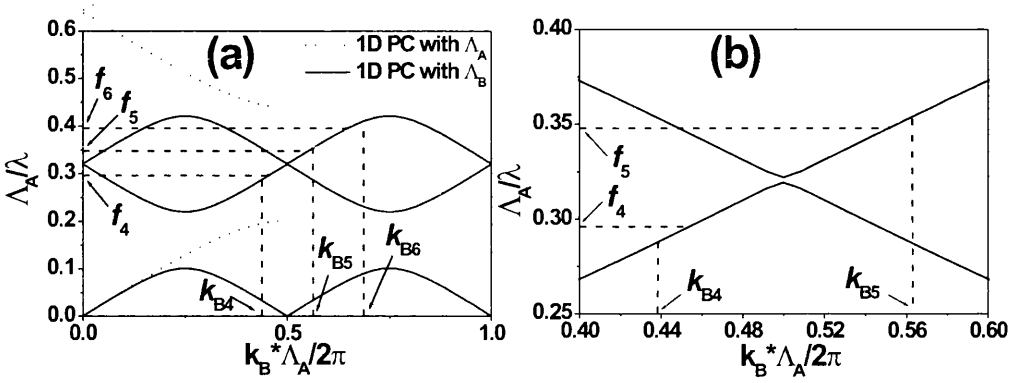

Fig. A2.2. Wave-vector diagrams of 1-D PhC stacks with periods of Λ_A (dot curves) and Λ_B (solid curves). $\Lambda_B = 2\Lambda_A$, $\varepsilon_{Si} = 12$, $\varepsilon_{air} = 1$, $n_h l_h = n_l l_l$, the Bloch wave vectors (k_{B4}, k_{B5}, and k_{B6}) are from Eqn. (A2.1), and the transmission frequencies (f_4, f_5, and f_6) are from TMM calculations. The cavity length is two periods of stack *B*. (b) is a magnified view of (a).

In the case of a 1D PhC microcavity of the type shown in Fig. A2.1a, the transmission frequencies can be calculated using transfer matrix method (TMM). The corresponding values are shown as horizontal dashed lines in Fig. A2.2 and are labelled f_4, f_5, and f_6. If the two methods for calculating the resonant condition are entirely equivalent, the vertical and horizontal dashed lines will intersect on the appropriate branches of the wave vector diagrams. In the event, a frequency mismatch of less than 3 percent is obtained, which can be ascribed to the neglect of the penetration depth in Eqn. (A2.1). This demonstrates that Eqn. (A2.1) and the TMM can be used interchangeably to calculate the resonant wavelengths of a complex multiple layer 1D PhC microcavity.

Whilst the TMM provides the accurate calculation of the transmission and reflection of multiple layer 1D PhC microcavity, the wave vector diagram approach enables rapid optimisation of the PhC central section of the microcavities of the types shown in Fig. A2.1. The wave-vector diagrams of the stack Λ_B can be tuned by varying the period, the air fraction and the refractive index contrast of the periodic

structure until its pass band lies within the first band gap of the 1D PhCs of period Λ_A used to form the reflectors. Since the transmission wavelengths are adjustable with several degrees of freedom, Eqn. (A2.1) provides a straightforward tool for designing a multi-wavelength transmission filter. Another merit of the wave-vector diagram model is its scope for application to more complicated 1D PhC slab waveguide structures. However, in order to use this model, it is necessary first to plot the wave-vector diagrams of the 1D PhC slab lattices.

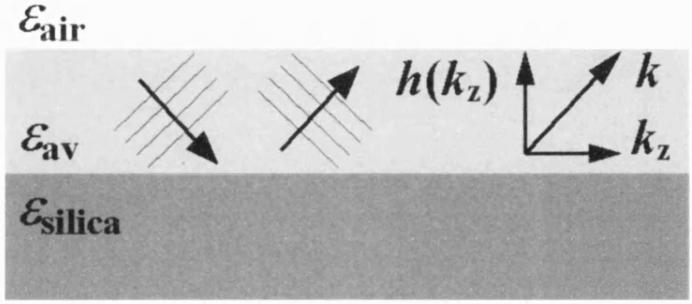

Fig. A2.3. Schematic of a plane wave guided in a slab waveguide and its component wave vectors.

In contrast with 1D multi-layer stacks, the confined nature of the guided waves must be taken into account in slab structures where 1D PhCs are etched. Fig. A2.3 illustrates the wave vector model for a propagating mode in a slab waveguide of dielectric constant equal to the spatial average, ε_{av}. The wave vector diagram gives the following dispersion relationship for such a mode:

$$f(k_z) = \frac{ck}{2\pi\sqrt{\varepsilon_{av}}} = \frac{c\sqrt{h^2(k_z) + k_z^{\,2}}}{2\pi\sqrt{\varepsilon_{av}}} \approx \sqrt{\frac{c^2 h^2(k_z)}{(2\pi)^2 \varepsilon_{av}} + f_0^{\,2}(k_z)} \qquad \text{(A2.2)}$$

where, c is the speed of light in free space, k is the wave vector of the corresponding plane wave (see Fig. A2.3), k_z is the in-plane wave vector amplitude (propagation constant), the frequency, $f(k_z)$, and the vertical wave vector component, $h(k_z)$, inside the slab are functions of k_z. The definition of $f_0(k_z)$ will be explained later.

It is proposed here that Eqn. (A2.2) is used in a phenomenological way to account for the vertical confinement of the propagating modes in slab waveguide and the action of the 1D PhC lattice to the Bloch waves in the in-plate direction. If the vertical dielectric contrast is large, the out-of-plane wave vector components, $h(k_z)$, of the Bloch modes inside the 1D PhC will resemble the vertical field distribution of the

guided modes inside the equivalent slab waveguide of dielectric constant equal to ε_{av} [Gerace 04]. In this way, the relationship between $h(k_z)$ and k_z can be well approximated by solving the corresponding slab waveguide. On the other hand, the in-plane components of the wave vectors of the guided waves, k_z, interact with the periodic lattice, and give rise to band splitting when k_z approaches the edge of the Brillouin zone according to the Bloch-Floquet theorem. This band splitting is expressed in the form of $f_0(k_z)$, and the effect of the periodic lattice on k_z is calculated by using the Plane-Wave Expansion method in an infinite 1D periodic multilayer.

The rationalisation of Eqn. (A2.2) is that it accounts for the dominant physics, albeit in a phenomenological way. The $h(k_z)$ term provides information about the blue shift in the dispersion relationship arising from the strong vertical field confinement to the equivalent slab waveguide [Gerace 04]. The $f_0(k_z)$ term stands for the band splitting arising from the strong periodic variation in the dielectric constant.

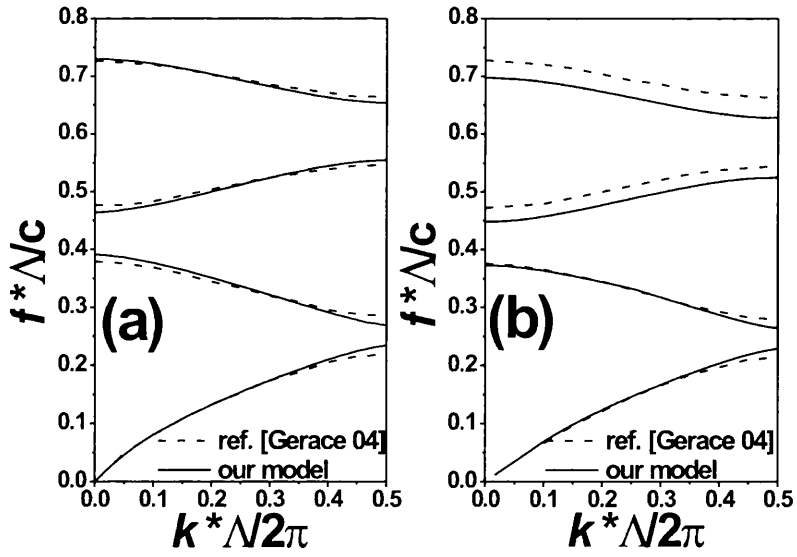

Fig. A2.4. Calculated wave-vector curves of PhC silicon slabs using the approximate method of Eqn. (A2.2) (solid lines) and the rigorous method in ref. [Gerace 04] (dashed lines). Only TE modes are calculated. The overlap layers are air. The substrate layers in (a) and (b) are air and silica respectively. The thickness of the slab is 0.4 times the period, the air fraction is 0.3, with $\varepsilon_{Si} = 12$, $\varepsilon_{air} = 1$, $\varepsilon_{Silica} = 2.1$.

Fig. A2.4 compares this approximate wave vector curves obtained from Eqn. (A2.2) (solid lines) with the more rigorous results taken from ref. [Gerace 04] (dashed

lines). Only TE modes are calculated. There is excellent agreement between these two results, especially for the first few bands.

This approximate Bloch wave-vector diagram constitutes the basis for explaining the close match between the measurement and calculation described in the next subsection.

A2.3 Design and measurements

The validity of the wave vector diagram approach was tested by applying it to the design of a 1D PhC microcavity waveguide device with three resonant wavelengths within its stop-band. The device structure, schematically shown in Fig. A2.1c, comprised 1D PhC reflectors of period Λ_A surrounding another 1D PhC of period Λ_B ($\Lambda_B > \Lambda_A$). The period and air fraction of the inner 1D PhC were then optimised so the transmission peaks coincided with the design wavelengths. The specification for the microcavity was that it should transmit simultaneously light in the telecommunications bands at 1310 nm and 1550 nm wavelength.

A silicon-on-insulator wafer with the top silicon layer of 350 nm thick was used. A 2.4 μm wide ridge waveguide was defined by conventional photolithography and subsequent ICP powered reactive ion etching with a mixed gas of trifluoromethane (CHF_3) and sulphur hexafluoride (SF_6). The ridge height was estimated to be ~300 nm, i.e. almost the full thickness of the Si layer.

Then, a 200 nm thick PMMA layer was applied on the wafer by spin coating, and the microcavity pattern was written into it by electron-beam-lithography (EBL) and transferred into the ridge waveguide by further reactive ion etching. In order to maintain the accuracy of the structure dimensions, the PMMA layer was directly used as the etch mask and no ICP power was used during the RIE process. The depth of the resulting air gaps was ~200 nm, limited by the ~1:1 etch rates of Si and PMMA.

A scanning electron microphotograph of the fabricated structure is shown in Fig. A2.5. From left to right, the structure consists of a two-cycle PhC reflector of measured period Λ_A = 493 nm (design value of Λ_A = 500 nm), a microcavity comprising a two-cycle PhC of measured period Λ_B = 985 nm (design value of Λ_B = 1000 nm), and a second reflector formed by two and half-cycles of a PhC of period Λ_A. The measured air fractions of periods *A* and *B* are 0.67 and 0.74, respectively, against design values of 0.72 and 0.73. The discrepancy between the designed and

measured feature sizes is primarily limited by the resolution of the electron beam lithography process.

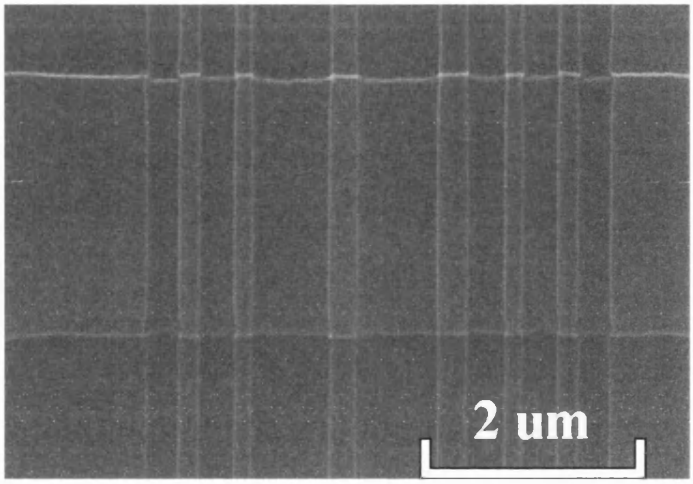

Fig. A2.5. Scanning electron micrograph of a fabricated multi-channel-transmission planar ridge waveguide filter based on a SOI wafer.

The sample was then thinned by mechanical polishing to ~150 μm from the backside and cleaved to produce optical quality facets. Light of a super-continuum source from a piece of endless single mode photonic crystal fibre [Wadsworth 04] was coupled into the ridge waveguide through a micro-lensed fiber. The transmitted spectrum was measured using an optical spectral analyser and was shown in Fig. A2.6a. Three transmission peaks occur at wavelengths of 1168 nm, 1321 nm and 1562 nm. The positions of the latter two agree well with the 1310 nm and 1550 nm design specification to better than 1%.

Accurate measurements of the quality factor, Q, and transmittance of the resonance, T, at 1562 nm wavelength were performed using a tuneable diode (C-band) laser with a wavelength step resolution of 0.01 nm. The results are $Q \approx 230$ and $T \approx 0.11$, indicating reasonable control of the loss in the fabrication.

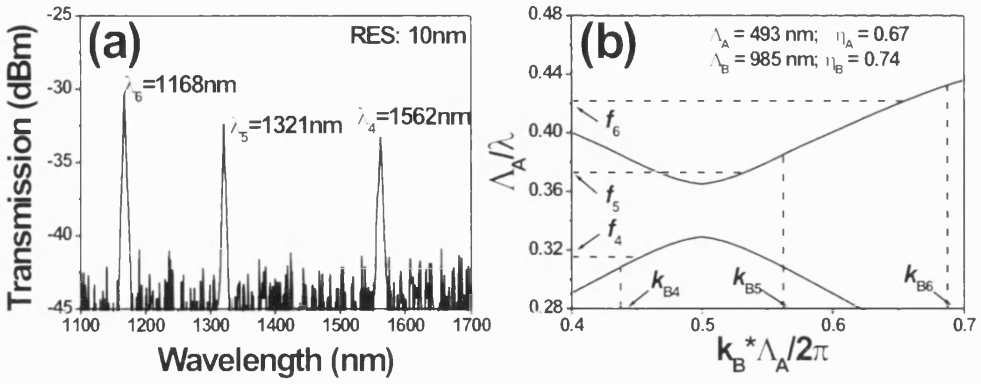

Fig. A2.6. (a) Transmission spectrum of the fabricated multi-channel-transmission planar ridge waveguide filter. (b) Comparison of the measured and calculated resonant wavelengths in the wave-vector diagram. The 4th, 5th, and 6th resonant modes are labelled. The wave-vector k_B comes from Eqn. (A2.2) with $f = \Lambda_A/\lambda$, $\Lambda_A = 510$ nm, $\Lambda_B = 1012$ nm, $\eta_B = 0.75$.

Fig. A2.6b shows the calculated wave-vector curves of the PhC slab inside the cavity using the simplified equation (A2.2). Values of the resonant wave-vectors, k_B, found from Eqn. (A2.1) with $L_p = 0$, and the measured transmission frequencies, $f = \Lambda_A/\lambda$, taken from Fig. A2.6a, are also shown in the wave vector diagram. The three transmission wavelengths correspond to the 4th, 5th, and 6th resonant modes of the cavity. Good agreement between the measured and calculated results is achieved with errors less than 3.5%.

A2.4. Conclusion

Table A2.1 summarises the results of the work described above. Firstly, in multiple layer stacks, the normalised resonant wavelengths, Λ_A/λ, obtained from the wave-vector diagram approach and the Eqn. (A2.1) are compared with the results from the rigorous TMM calculations. The discrepancies between these two are shown in brackets. Secondly, in 1D PhC ridge waveguides, the normalised resonant wavelengths obtained from our approach are compared with those obtained from experimental measurements (Fig. A2.6a). Again, the difference is shown in brackets. Excellent agreement is obtained in both cases, demonstrating the validity of applying the simple wave vector diagram approach to the design of multi-wavelength transmission 1D PhC microcavity filters with high index contrast.

Λ_A/λ / Resonant Mode	Multi-layer Stacks (Fig. A2.2)		Planar Slab Waveguide (Fig. A2.6)	
	TMM	New model (Err.)	Measurement	New model (Err.)
4^{th}	0.296	0.287 (-3.0%)	0.315	0.308 (-2.2%)
5^{th}	0.348	0.354 (1.7%)	0.373	0.385 (3.2%)
6^{th}	0.396	0.410 (3.5%)	0.422	0.433 (2.6%)

Table A2.1. Comparison of the normalised resonant wavelengths.

A simplified analytical model based on wave-vector diagrams of a 1D PhC lattice has been introduced to design multi-wavelength transmission microcavity structured filters in multi-layer stack and ridge waveguide schemes. Its validity in analysing the behaviour of both types of structure is verified by comparison with the rigorous calculation and with the experimental measurement. In a microcavity structured ridge waveguide in a SOI wafer, multi-wavelength transmission has been observed at wavelengths that fit well with the calculated values. Such multi-transmission filters can find many applications in a wide range.

Figures and Tables

Chapter 2

Background on Electromagnetic Theory

Chapter 3

Fiber Tapering, Planar Processing, and Interference Lithography Techniques

Chapter 4
Surface Bragg Gratings on Fiber Tapers

Chapter 5

Other Longitudinal Structures on Fiber Tapers

Chapter 6

Internal Excitation and Superfocusing of Surface Plasmon Polaritons on an Apertureless Silver-Coated Fiber Tip

Appendix

References

[Adam 98] P. M. Adam, P. Royer, R. Laddada, and J. L. Bijeon, "Apertureless near-field optical microscopy: influence of the illumination conditions on the image contrast", Appl. Opt., **37**, 1814 (1998).

[Al-Bader 92] S. J. Al-Bader, and M. Imtaar, "Azimuthally uniform surface-plasma modes in thin metallic cylindrical shells", IEEE J. Quan. Electron. **28**, 525 (1992).

[Al-Bader 93] S. J. Al-Bader, and M. Imtaar, "Optical fiber hybrid-surface Plasmon polaritons", J. Opt. Soc. Am. B **10**, 83 (1993).

[Archambault 93] J. L. Archambault, L. Reekie, and P. St. J. Russell, "100% reflectivity Bragg reflectors produced in optical fibres by single excimer laser pulses" Electron. Lett. **29**, 453 (1993).

[Ashino 98] M. Ashino, and M. Ohtsu, "Fabrication and evaluation of a localized plasmon resonance probe for near-field optical microscopy/spectroscopy", Appl. Phys. Lett., **72**, 1299 (1998).

[Babadjanyan 00] A. J. Babadjanyan, N. L. Margaryan, and Kh. V. Nerkararyan, "Superfocusing of surface polaritons in the conical structure", J. Appl. Phys., **87**, 3785 (2000).

[Barclay 04] P. E. Barclay, K. Srinivasan, M. Borselli, and O. Painter, "Efficient input and output fiber coupling to a photonic crystal waveguide", Opt. Lett. **29**, 697 (2004).

[Barnes 03] W. L. Barnes, A. Dereux, and T. W. Ebbesen, "Surface plasmon subwavelength optics", Nature **424**, 824 (2003).

[Berini 01] P. Berini, "Plasmon-polariton waves guided by thin lossy metal films of finite width: Bound modes of asymmetric structures", Phys. Rev. B, **61**, 10484 (2001).

[Betzig 91] E. Betzig, J. K. Trautman, T. D. Harris, J. S. Weiner, and R. L. Kostelak, "Breaking the Diffraction Barrier: Optical Microscopy of a Nanometric Scale", Science, **251**, 1468 (1991).

[Betzig 92] E. Betzig, and J. K. Trautman, "Near-Field Optics: Microscopy, Spectroscopy, and Surface Modification Beyond the Diffraction Limit", Science, **257**, 189 (1992).

[Bilodeau 93] F. Bilodeau, B. Malo, J. Albert, D. C. Johnson, K. O. Hill, Y. Hibino, M. Abe, and M. Kawachi, "Photosensitization of optical fiber and silica-on-silicon/silica waveguides", Opt. Lett., **18**, 953 (1993).

[Birks 92] T. A. Birks and Y. W. Li, "The shape of fiber tapers", IEEE J. Lightwave Technol., **10**, 432 (1992).

[Birks 97] T. A. Birks, J. C. Knight, and P. St. J. Russell, "Endlessly single-mode photonic crystal fiber", Opt. Lett. **22**, 961 (1997).

[Bouhelier 03] A. Bouhelier, J. Renger, M. R. Beversluis, and L. Novotny, "Plasmon-coupled tip-enhanced near-field optical microscopy", J. Microsc. **210**, 220 (2003).

[Bozhevolnyi 01] S. I. Bozhevolnyi, J. Erland, K. Leosson, P. M. W. Skovgaard, and J. M. Hvam, "Waveguiding in surface plasmon polariton band gap structures", Phys. Rev. Lett. **86**, 3008 (2001).

[Burnstein 74] E. Burnstein, W. P. Chen, Y. J. Chen, and A. Hartstein, "Surface-polaritons propagating electromagnetic modes at interfaces", J. Vac. Sci. Technol. **11**, 1004 (1974).

[Chiang 00] K. S. Chiang, Y. Liu, M. N. Ng, and X. Dong, "Analysis of etched long-period fibre grating and its response to external refractive index", Elec. Lett. **36**, 966 (2000).

[CST microwave studio 2006] http://www.cst.com/.

[Diez 01] A. Diez, M. V. Andres, and J. L. Cruz, "In-line fiber-optic sensors based on the excitation of surface plasma modes in metal-coated tapered fibers", Sensors and Actuators B **73**, 95 (2001).

[Ding 05] J. F. Ding, A. P. Zhang, L. Y. Shao, J. H. Yan, and S. He, "Fiber-taper seeded long-period grating pair as a highly sensitive refractive-index sensor", IEEE Photon. Technol. Lett. **17**, 1247 (2005).

[Ding 06] W. Ding, S. R. Andrews, T. A. Birks, and S. Maier, "Modal coupling in fiber tapers decorated with metallic surface gratings", Opt. Lett. **31**, 2556 (2006).

[Ditlbacher 02] H. Ditlbacher, J. R. Krenn, G. Schider, A. Leitner, and F. R. Aussenegg, "Two-dimensional optics with surface plasmon polaritons", Appl. Phy. Lett. **81**, 1762 (2002).

[Dong 95] L. Dong, J. L. Archambault, L. Reekie, R. St. J. Russell, and D. N. Payne, "Photoinduced absorption change in germanosilicate performs: evidence for the color-center model of photosensitivity", Appl. Opt. **34**, 3436 (1995).

[Erdogan 96] T. Erdogan and J. E. Sipe, "Tilted fiber phase gratings", J. Opt. Soc. Am. A **13**, 296 (1996).

[Erdogan 97] T. Erdogan, "Fiber grating spectra", J. Lightwave Technol. **15**, 1277 (1997).

[Eckert 00] R. Eckert, J. M. Freyland, H. Gersen, and H. Heinzelmann "Near-field flurescence imaging with 32 nm resolution based on microfabricated cantilevered probes", Appl. Phys. Lett. **77**, 3695 (2000).

[Feced 99] R. Feced, C. Alegria, M. N. Zervas, and R. I. Laming, "Acoustooptic attenuation filters based on tapered optical fibers", IEEE J. Selected Topics in Quan. Electron. **5**, 1278 (1999).

[Foresi 97] J. S. Foresi, P. R. Villeneuve, J. Ferrera, E. R. Thoen, G. Steinmeyer, S. Fan, J. D. Joannopoulos, L. C. Kimerling, H. I. Smith, and E. P. Ippen, "Photonic-bandgap microcavities in optical waveguides", Nature **390**, 143 (1997).

[Gamo 97] K. Gamo, "Recent advances of focused ion beam technology", Nucl. Instr. And Meth. B **121**, 464 (1997).

[Gerace 04] D. Gerace and L. C. Andreani, "Gap maps and intrinsic diffraction losses in one-dimensional photonic crystal slabs", Phys. Rev. E. **69**, 056603 (2004).

[Gibson 05] B. C. Gibson, S. T. Huntington, S. Rubanov, P. Olivero, K. D. Lyytikainene, J. Canning, and J. D. Love, "Exposure and characterization of nano-structured hole arrays in tapered photonic crystal fibers using a combined FIB SEM technique", Opt. Express **13**, 9023 (2005).

[Gierak 99] J. Gierak, A. Septier, and C. Vieu, "Design and realization of a very high-resolution FIB nanofabrication instrument", Nucl. Instr. And Meth. A **427**, 91 (1999).

[Grosjean 05] T. Grosjean, A. Sabac, and D. Courjon, "A versatile and stable device allowing the efficient generation of beams with radial, azimuthal or hybrid polarizations", Opt. Comm. **252**, 12 (2005).

[Hafner 90] C. Hafner, "The Generalized Multiple Multipole Technique for Computational Electromagnetic", Artech (Boston), 1990.

[Hernandez 04] D. M. Hernandez, J. Mora, P. P. Millan, A. Diez, J. L. Cruz, and M. V. Andres, "Temperature sensor based on the power reflected by a Bragg grating in a tapered fiber", Appl. Opt. **43**, 2393 (2004).

[Hill 78] K. O. Hill, Y. Fujii, D. C. Johnson, and B. S. Kawasaki, "Photosensitivity in optical fiber waveguide: Application to reflection filter fabrication", Appl. Phys. Lett. **32**, 647 (1978).

[Hill 97] K. O. Hill and G. Meltz, "Fiber Bragg grating technology funfamentals and overview", J. Lightwave Technol. **15**, 1263 (1997).

[Hirsch 03] L. R. Hirsch, R. J. Stafford, J. A. Bankson, S. R. Sershen, B. Rivera, R. E. Price, J. D. Hazle, N. J. Halas, and J. L. West, "Nanoshell-mediated near-infrared thermal therapy of tumors under magnetic resonance guiding" Proc. Nat. Acad. Sci. **100**, 13549 (2003).

[Hodzic 04] V. Hodzic, J. Orloff, and C. C. Davis, "Periodic structures on biconically tapered optical fibers using ion beam milling and boron implantation", J. Lightwave Technol. **22**, 1610 (2004).

[Homola 99] J. Homola, S. S. Yee, and G. Gauglitz, "surface plasmon resonance sensors: review", Sensors and Actuators B **54**, 3 (1999).

[Ishimaru 91] A. Ishimaru, "Electromagnetic Wave Propagation, Radiation, and Scattering", Prentice-Hall (New Jersey), 1991.

[Jackson 99] J. D. Jackson, "Classical Electrodynamics", John Wiley & Sons Inc. (New York), 1999.

[James 03] S. W. James, and R. P. Tatam, "Optical fibre long-period grating sensors: characteristics and application", Meas. Sci. Technol. **14**, R49 (2003).

[Janunts 05] N. A. Janunts, K. S. Baghdasaryan, Kh. V. Nerkararyan, and B. Hecht, "Excitation and superfocusing of surface plasmon polaritons on a silver-coated optical fiber tip", Opt. Comm. **253**, 118 (2005).

[Jenkins 81] F. A. Jenkins and H. E. White, Fundamentals of Optics, (Auckland: McGraw-Hill, 1981).

[Joannopoulos 95] J. D. Joannopoulos, R. Meade, and J. Winn, "Photonic Crystals", Princeton University Press (Princeton), (1995).

[Kakarantzas 02] G. Kakarantzas, T. A. Birks, and P. St. J. Russell, "Structural long-period gratings in photonic crystal fibers", Opt. Lett. **27**, 1013 (2002).

[Kneipp 02] K. Kneipp, H. Kneipp, I. Itzkan, R. R. Dasari, and M. S. Feld, "Surface-enhanced Raman scattering and biophysics", J. Phys. **14**, R597 (2002).

[Krenn 00] J. R. Krenn, G. Schider, W. Rechberger, B. Lamprecht, A. Leitner, F. R. Aussenegg, and J. C. Weeber, "Design of multipolar plasmon excitations in silver nanoparticles" Appl. Phys. Lett. **77**, 3379 (2000).

[Laffont 01] G. Laffont and P. Ferdinand, "Tilted short-period fiber-Bragg-grating-induced coupling to cladding modes for accurate refractometry", Meas. Sci. Technol. **12**, 765 (2001).

[Lamprecht 00] B. Lamprecht, G. Schider, R. T. Lechner, H. Ditlbacher, J. R. Krenn, A. Leitner, and F. R. Aussenegg, "Metal nanoparticle gratings: influence of dipolar particle interaction on the plasmon resonance" Phys. Rev. Lett. **84**, 4721 (2000).

[Lee 05] H. Y. Lee, S. J. Cho, and G. Y. Nam, "Multiple-wavelength-transmission filters based on Si-SiO2 one-dimensional photonic crystals", J. Appl. Phys. **97**, 103111 (2005).

[Lefevre 80] H. C. Lefevre, "Single-mode fiber fractional wave devices and polarisation controllers", Elec. Lett. **16**, 778 (1980).

[Lemaire 93] P. J. Lemaire, R. M. Atkins, V. Mizrahi, and W. A. Reed, "High pressure H_2 loading as a technique for achieving ultrahigh UV photosensitivity and thermal sensitivity in GeO_2 doped optical fibres", Electron. Lett. **29**, 1191 (1993).

[Lewis 84] A. Lewis, M. Isaacson, A. Harootunian, and A. Muray, "Development of a 500 Å spatial resolution light microscope: I. Light is efficiently transmitted through $\lambda/16$ diameter apertures", Ultramicroscopy, **13**, 227 (1984).

[Love 86] J. D. Love, and W. M. Henry, "Quantifing loss minimisation in single-mode fibre tapers" Electron. Lett. **22**, 912 (1986).

[Love 91] J. D. Love, W. M. Henry, W. J. Stewart, R. J. Black, S. Lacroix, and F. Gonthier, "Tapered single-mode fibres and devices Part 1: Adiabaticity criteria", IEE Proceedings-J, **138**, 343 (1991).

[Maier 01] S. A. Maier, M. L. Brongersma, P. G. Kik, S. Meltzer, A. A. G. Requicha and H. A. Atwater, "Plasmonics - A Route to Nanoscale Optical Devices", Adv. Mat. **13**, 1501 (2001).

[Maier 02] S. A. Maier, M. L. Brongersma, P. G. Kik, and H. A. Atwater, "Observation of near-field coupling in metal nanoparticle chains using far-field polarization spectroscopy", Phys. Rev. B **65**, 193408 (2002).

[Maier 05] S. A. Maier, M. D. Friedman, P. E. Barclay, and O. Painter, "Experimental demonstration of fiber-accessible metal nanoparticle plasmon waveguides for planar energy guiding and sensing", Appl. Phys. Lett. **86**, 071103 (2005).

[Maier 06] S. A. Marier, Plasmonics: Fundamentals and Applications, Springer-Verlag: (New York), 2006.

[McCaulley 94] J. A. McCaulley, V. M. Donnelly, M. Vernon, and I. Taha, "Temperature dependence of the near-infrared refractive index of silicon, gallium arsenide, and indium phosphide", Phys. Rev. B **49**, 7408 (1994).

[McFarland 03] A. D. McFarland and R. P. V.Duyne, "Single silver nanoparticles as real-time optical sensors with Zeptomole sensitivity", Nano Lett. **3**, 1057 (2003).

[Mekis 96] A. Mekis, J. C. Chen, I. Kurland, S. Fan, P. R. Villeneuve, and J. D. Joannopoulos, "High Transmission through Sharp Bends in Photonic Crystal Waveguides", Phys. Rev. Lett. **77**, 3787 (1996).

[Meltz 89] G. Meltz, W. W. Morey, and W. H. Glenn, "Formation of Bragg gratings in optical fibers by a transverse holographic method", Opt. Lett. **14**, 823 (1989).

[Milner 01] R. G. Milner, and D. Richards, "The role of tip plasmons in near-field Raman microscopy", J. Microsc. **202**, 66 (2001).

[Mock 03] J. J. Mock, D. R. Smith, and S. Schultz, "Local refractive index dependence of plasmon resonance spectra from individual nanoparticles", Nano. Lett. **3**, 485 (2003).

[Mortimore 85] D. B. Mortimore, "Wavelength-flattened fused couplers", Electron. Lett. **21**, 742, (1985).

[Nerkararyan 97] Kh. V. Nerkararyan, "Superfocusing of a surface polariton in a wedge-like structure", Physics Lett. A, **237**, 103, (1997).

[Novotny 94] L. Novotny, and C. Hafner, "Light propagation in a cylindrical waveguide with a complex, metallic, dielectric function", Phys. Rev. E **50**, 4094 (1994).

[OptiFDTD 5.0] http://www.optiwave.us/fdtd/optifdtd.html.

[Orloff 03] J. Orloff, M. Utlaut, and L. W. Swanson, "High resolution focused ion beams", (Kluwer Academic, New York), 2003.

[Peyrade 02] D. Peyrade, E. Silberstein, Ph. Lalanne, A. Talneau, and Y. Chen, "Short Bragg mirrors with adiabatic modal conversion", Appl. Phys. Lett., **81**, 829 (2002).

[Pohl 84] D. W. Pohl, W. Denk, and M. Lanz, "Optical stethoscopy: Image recording with resolution $\lambda/20$", Appl. Phys. Lett., **44**, 651 (1984).

[Prade 91] B. Prade, J. Y. Vinet, and A. Mysyrowicz, "Guided optical waves in planar heterostructures with negative dielectric constant" Phys. Rev. B **44**, 13556 (1991).

[Prewett 91] P. D. Prewett and G. L. R. Mair, "Focused Ion Beams from Liquid Metal Ion Source", Research Studies Press (Taunton), 1991.

[Prodan 03] E. Prodan, C. Radloff, N. J. Halas, and P. Nordlander, "A hybridization model for the plasmon response of complex nanostructures", Science **302**, 419 (2003).

[Quabis 05] S. Quabis, R. Dorn, and G. Leuchs, "Generation of a radially polarized doughnut mode of high quality", Appl. Phys. B **81**, 597 (2005).

[Reddick 89] R. C. Reddick, R. J. Warmack, and T. L. Ferrell, "New form of scanning optical microscopy", Phys. Rev. B, **39**, 767 (1989).

[Raschke 03] G. Raschke, S. Kowarik, T. Franzl, C. Sonnichsen, T. A. Klar, and J. Feldmann, "Biomolecular recognition based on single gold nanoparticle light scattering", Nano Lett., **3**, 937 (2003).

[Rakic 98] A. D. Rakic, A. B. Djurisic, J. M. Elazar, and M. L. Majewski, "Optical properties of metallic films for vertical-cavity optoelectronic devices", Appl. Opti., **37**, 5271 (1998).

[Ritchie 57] R. H. Ritchie, "Plasma losses by fast electrons in thin films", Phys. Rev. **106**, 874 (1957).

[Russell 85] P. St. J. Russell, and R. Ulrich, "Grating-fiber coupler as a high-resolution spectrometer", Opt. Lett. **10**, 291 (1985).

[Russell 95] P. St. J. Russell, T. A. Birks, and F. D. Lloyd-Lucas, "Photonic Bloch waves and photonic band gaps", in Confined Electrons and Photons: New Physics and Applications, E. Burstein & C. Weisbuch (editors), pp 585-633, Plenum Press, 1995.

[Russell 96] P. St. J. Russell and T. A. Birks, "Bloch wave optics in photonic crystals: physics and applications", in Photonic Band Gap Materials, C. M. Soukoulis (editor), Kluwer Academic Publishers, pp. 71-91 (1996).

[Russell 03a] P. Russell, "Photonic crystal fibers", Science, **299**, 358 (2003).

[Russell 03b] P. St. J. Russell, "Designing photonic crystals", in Electron and Photon Confinement in Semiconductor Nanostructures, IL Nuovo Cimento (editor), Amsterdam: IOS Press, pp. 79-103 (2003).

[Sanchez 99] E. J. Sanchez, L. Novotny, and X. S. Xie, "Near-Field Fluorescence Microscopy Based on Two-Photon Excitation with Metal Tips", Phys. Rev. Lett. **82**, 4014 (1999).

[Sarid 81] D. Sarid, "Long-Range Surface-Plasma Waves on Very Thin Metal Films", Phys. Rev. Lett. **47**, 1927 (1981).

[Schroeder 01] K. Schroeder, W. Ecke, R. Mueller, R. Willsch, and A. Andreev, "A fiber Bragg grating refractometer", Meas. Sci. Technol. **12**, 757 (2001).

[Shon-Roy 98] L. Shon-Roy, A. Wiesnoski, and R. Zorich "Advanced Semiconductor Fabrication Handbook", Integrated Circuit Engineering Corporation (Scottsdale, Arizona US), 1998.

[Snyder 83] A. W. Snyder, J. D. Love, "Optical Waveguide Theory", Chapman and Hall (London), 1983.

[Stockman 04] M. I. Stockman, "Nanofocusing of Optical Energy in Tapered Plasmonic Waveguides", Phys. Rev. Lett. **93**, 137404 (2004).

[Taflove 97] A. Taflove, "Computational Electrodynamics: The Finite-Difference Time-Domain Method" (Second Edition), Artech House (Boston), 1997.

[Vaccaro 03] L. Vaccaro, L. Aeschimann, U. Staufer, H. P. Herzig, and R. Dandliker, "Propagation of the electromagnetic field in fully coated near-field optical probes", Appl. Phys. Lett. **83**, 584 (2003).

[Vengsarkar 96] A. M. Vengsarkar, P. J. Lemaire, J. B. Judkins, V. Bhatia, T. Erdogan, and J. E. Sipe, "Long-period fiber gratings as band-rejection filters", J. Lightwave Technol. **14**, 58 (1996).

[Wadsworth 04] W. J. Wadsworth, N. Joly, J. C. Knight, T. A. Birks, F. Biancalana, P.St.J. Russell, "Supercontinuum and four-wave mixing with Q-switched pulses in endlessly single-mode photonic crystal fibres", Opt. Express **12**, 299 (2004).

[Wang 04] Z. Wang, R. W. Peng, F. Qiu, X. Q. Huang, M. Wang, A. Hu, S. S. Jiang, and D. Feng, "Selectable-frequency and tunable-Q perfect transmissions of electromagnetic waves in dielectric heterostructures", Appl. Phys. Lett. **84**, 3969 (2004).

[Weiland 77] T. Weiland, "A discretization method for the solution of Maxwell's equations for six-component fields", Electronics and Communication (AEU). **31**, 116 (1977).

[Wokaun 82] A. Wokaun, J. P. Gordon, and P. F. Liao, "Radiation damping in surface-enhanced Raman scattering", Phys. Rev. Lett. **48**, 957 (1982).

[Xu 95] M. G. Xu, L. Dong, L. Reekie, J. A. Tucknott, and J. L. Cruz, "Temperature-independent strain sensor using a chirped Bragg grating in a tapered optical fibre", Elec. Lett. **31**, 823 (1995).

[Yablonovitch 87] E. Yablonovitch, "Inhibited Spontaneous Emission in Solid-State Physics and Electronics", Phys. Rev. Lett., **58**, 2059 (1987).

[Yariv 97] A. Yariv, "Optical Electronics in Modern Communications" (Fifth Edition), Oxford University Press, 1997.

[Yee 66] K. S. Yee, "Numerical solution of initial boundary value problems involving Maxwell's equations in isotropic media", IEEE Trans. Antennas and Propagation. **14**, 302 (1966).

[Yin 05] L. Yin, V. K. Vlasko-Vlasov, J. Pearson, J. M. Hiller, J. Hua, U. Welp, D. E. Brown, and C. W. Kimball, "Subwavelength focusing and guiding of surface plasmons", Nano Lett. **5**, 1399 (2005).

[Zengerle 87] R. Zengerle, "Light propagation in singly and doubly periodic planar waveguides", J. Mod. Opt., **34**, 1589 (1987).

[Zenhausern 94] F. Zenhausern, M. P. O'Boyle, and H. K. Wickramasinghe, "Apertureless near-field optical microscope", Appl. Phys. Lett. **65**, 1623 (1994).